Development of Statistical Tools for Studies of the Rapid Neutron Capture Process

by

Yukiya Saito

B.Sc., The University of Tokyo, 2016

M.Sc., The University of British Columbia, 2018

A THESIS SUBMITTED IN PARTIAL FULFILLMENT
OF THE REQUIREMENTS FOR THE DEGREE OF

Doctor of Philosophy

in

THE FACULTY OF GRADUATE AND POSTDOCTORAL STUDIES

(Physics)

The University of British Columbia

(Vancouver)

April 2023

The following individuals certify that they have read, and recommend to the Faculty of Graduate and Postdoctoral Studies for acceptance, the thesis entitled:

Development of Statistical Tools for Studies of the Rapid Neutron Capture Process

submitted by **Yukiya Saito** in partial fulfillment of the requirements for the degree of **Doctor of Philosophy** in **Physics**.

Examining Committee:

Reiner Krücken, Professor, Physics & Astronomy, UBC
Supervisor

Iris Dillmann, Senior Research Scientist, TRIUMF
Co-supervisor

Janis A. McKenna, Professor, Physics & Astronomy, UBC
University Examiner

Trevor Campbell, Associate Professor, Statistics, UBC
University Examiner

Morten Hjorth-Jensen, Professor, Physics, Michigan State University and University of Oslo
External Examiner

Additional Supervisory Committee Members:

Alison Lister, Associate Professor, Physics & Astronomy, UBC
Supervisory Committee Member

Jeremy Heyl, Professor, Physics & Astronomy, UBC
Supervisory Committee Member

Gary Hinshaw, Professor, Physics & Astronomy, UBC
Supervisory Committee Member

Abstract

The rapid neutron capture process (*r*-process) is a complex nucleosynthesis mechanism for the creation of heavy nuclei, which occurs under extreme astrophysical conditions, as expected to occur in compact binary mergers and some types of core-collapse supernovae. An accurate understanding of the *r*-process is crucial for explaining the abundances of roughly half the elements heavier than iron in the solar system. Not only are the predictions of the r-process abundance pattern affected by the thermodynamical conditions of such astrophysical events, significant uncertainty also arises from the properties of thousands of neutron-rich nuclides involved in the process. While many of the neutron-rich nuclei may become experimentally accessible in the near future, it is essential to quantify the uncertainty originating from theoretical descriptions of atomic nuclei and identify key nuclear physics inputs of the numerical simulations of the *r*-process.

In this thesis, several statistical methods have been developed and applied to scrutinize the uncertainty of nuclear physics inputs in the studies of the *r*-process nucleosynthesis. The variance-based sensitivity analysis method identifies influential nuclear physics inputs in a statistically rigorous manner and probes their effect on elemental abundance patterns. The ensemble Bayesian model averaging method provides a simple framework for combining competing theoretical nuclear physics models based on experimental data and quantifying their uncertainties. Furthermore, an emulator of *r*-process abundance calculations has been developed using artificial neural networks, which dramatically speeds up the calculations of abundance patterns, potentially allowing for scaling up various statistical analyses. While the effectiveness of these methods has been shown for the specific features of the observed solar abundance pattern and nuclear physics observables, they are

readily applicable to broader aspects of the studies of the *r*-process nucleosynthesis.

Lay Summary

The origin of elements heavier than iron is not completely understood. Especially the process that can create the heaviest elements in the Universe called the "*r*-process" continues to be a topic of active research. In order to fully explain the abundances of nuclear species observed in the solar system, we need to understand the properties of many atomic nuclei that do not exist in nature, in addition to where the *r*-process can occur. This thesis describes statistical and machine learning tools that can help us evaluate how well we know some of the key nuclear physics relevant to the *r*-process, and what we need to know to understand it better.

Preface

In this thesis, my main research work and contributions are described. As a member of the Gamma-Ray Spectroscopy Group, I have also participated and taken shifts in many radioactive isotope beam experiments at TRIUMF in Canada and RIKEN in Japan over the past 7 years, which have led to publications. However, they are not described in this thesis.

The implementation of NUCLEARREACTIONNETWORK.JL described in Section 1.3 was performed in collaboration with TRIUMF co-op student Paul Virally (University of Waterloo) from Sep.-Dec. 2021. My role was the development of the design of the software, implementation of the core numerical routines, verification of the results, and supervision of Mr. Virally. Mr. Virally has implemented much of the software and performed related tasks, such as tests on a GPU, software profiling, and creating documentation. The software is available on https://github.com/YukiyaSaito/NuclearReactionNetwork.jl.

A version of Chapter 5 is under preparation for publication but has not been submitted yet. I have led the entire study in collaboration with I. Dillmann (TRIUMF), R. Kruecken (LBNL/UBC/TRIUMF), M. R. Mumpower (LANL), and R. Surman (U Notre Dame).

A version of Chapter 5 has been published as G. G. Kiss, A. Vitéz-Sveiczer, Y. Saito, A. Tarifeño-Saldivia, M. Pallas, J. L. Tain, I. Dillmann, J. Agramunt, A. Algora, C. Domingo-Pardo, A. Estrade, C. Appleton, J. M. Allmond, P. Aguilera, H. Baba, N. T. Brewer, C. Bruno, R. Caballero-Folch, F. Calvino, P. J. Coleman-Smith, G. Cortes, T. Davinson, N. Fukuda, Z. Ge, S. Go, C. J. Griffin, R. K. Grzywacz, O. Hall, A. Horváth, J. Ha, L. J. Harkness-Brennan, T. Isobe, D. Kahl, T. T. King, A. Korgul, S. Kovács, R. Krücken, S. Kubono, M. Labiche, J. Liu, J.

Liang, M. Madurga, K. Miernik, F. Molina, A. I. Morales, M. R. Mumpower, E. Nacher, A. Navarro, N. Nepal, S. Nishimura, M. Piersa-Siłkowska, V. Phong, B. C. Rasco, B. Rubio, K. P. Rykaczewski, J. Romero-Barrientos, H. Sakurai, L. Sexton, Y. Shimizu, M. Singh, T. Sprouse, T. Sumikama, R. Surman, H. Suzuki, T. N. Szegedi, H. Takeda, A. Tolosa, K. Wang, M. Wolinska-Cichocka, P. Woods, R. Yokoyama, and Z. Xu, "Measuring the β-decay Properties of Neutron-rich Exotic Pm, Sm, Eu, and Gd Isotopes to Constrain the Nucleosynthesis Yields in the Rare-earth Region." *The Astrophysical Journal*, 936(2):107, 2022, DOI: 10.3847/1538-4357/ac80fc. G. G. Kiss and A. Vitéz-Sveiczer (ATOMKI) were responsible for data collection and analysis. I was responsible for the analysis of the astrophysical implications of the experimental data and the composition of the corresponding parts of the manuscript. I performed the work in collaboration with I. Dillmann (TRIUMF), R. Kruecken (LBNL/UBC/TRIUMF), M. R. Mumpower (LANL), and R. Surman (U Notre Dame). Chapter 5 is based on the text and figures that I have prepared for the manuscript, except for Figures 5.1 and 5.2, which were prepared by G. G. Kiss.

A version of Chapter 6 is under preparation for publication but has not been submitted yet. I have led the entire study in collaboration with I. Dillmann (TRIUMF), R. Kruecken (LBNL/UBC/TRIUMF), M. R. Mumpower (LANL), and R. Surman (U Notre Dame).

Table of Contents

Abstract . . . . . **iii**

Lay Summary . . . . . **v**

Preface . . . . . **vi**

Table of Contents . . . . . **viii**

List of Tables . . . . . **xi**

List of Figures . . . . . **xii**

Glossary . . . . . **xvi**

Acknowledgments . . . . . **xix**

1 Introduction **1**

1.1 Structure of the Thesis 2

1.2 Synthesis of Elements 4

1.2.1 Nucleosynthesis up to Iron 5

1.2.2 Evidence of the Rapid Neutron Capture Process 9

1.2.3 Possible Sites of the *r*-Process 15

1.3 Nuclear Reaction Network Calculations 20

2 Nuclear Physics of the *r*-Process **27**

2.1 The Basics of the *r*-Process Abundance Pattern 27

2.1.1 Prominent Peaks in the Solar Abundance Pattern 27
2.1.2 The Rare-Earth Peak 32
2.1.3 Modeling of Nuclear Physics Inputs 33
2.1.4 Roles of Nuclear Physics Inputs 34
2.2 Nuclear Mass Models 37
2.2.1 Liquid Drop Model and Semiempirical Mass Formula . . 39
2.2.2 The Strutinsky Theorem 42
2.2.3 Finite Range Droplet Model (FRDM) 43
2.2.4 Hartree-Fock-Bogoliubov (HFB) Mass Models 47
2.2.5 Extended Thomas-Fermi Plus Strutinsky Integral (ETFSI) Mass Models 51
2.2.6 Weizsäcker-Skyrme (WS) Mass Models 52
2.2.7 Duflo-Zuker (DZ) Mass Model 54
2.2.8 Models by Koura, Uno, Tachibana, and Yamada (KUTY) . 54
2.2.9 Brief Comparison of Mass Models 55

3 Statistical Inference and Machine Learning Methods 61
3.1 Bayesian Statistics 62
3.2 Monte Carlo Method and Markov Chain Monte Carlo 64
3.3 Variance-Based Sensitivity Analysis Method 67
3.4 Neural Networks 72

4 Ensemble Bayesian Model Averaging of Nuclear Mass Models . . . 76
4.1 Method 78
4.1.1 Bayesian model averaging 78
4.1.2 Ensemble Bayesian model averaging 79
4.1.3 Setup of numerical experiment 82
4.2 Results and Discussion 85
4.2.1 Comparison with observations 85
4.2.2 Weights in the EBMA models 88
4.2.3 Uncertainty quantification with EBMA 91
4.3 Conclusions 95

5 Variance-Based Sensitivity Study with Experimental Data 97

5.1 Astrophysical implication of the experimental results 98
5.1.1 Method 98
5.1.2 Results 103
5.2 Summary and Conclusions 116

6 Emulation of a Nuclear Reaction Network Calculation Code 119
6.1 Numerical Experiment 120
6.1.1 Emulating nuclear reaction network calculations with ANNs 120
6.1.2 Distributions of theoretical nuclear physics inputs 122
6.1.3 Data pre-processing and training of ANNs 123
6.2 Results and Discussion 124
6.2.1 Optimized Emulator Architecture 124
6.2.2 Performance 126
6.2.3 Uncertainty Quantification 129
6.3 Conclusions 131

7 Summary and Outlook 132
7.1 Summary of the Contributions of This Thesis 132
7.2 Outlook 133

Bibliography 136

List of Tables

Table 2.1 A summary of rms errors of the mass models discussed in Section 2.2, with respect to the experimentally determined masses listed in the AME2020 [10]. 56

Table 4.1 95 % posterior highest density intervals (HDI) of the EBMA weights and standard deviations (variances), fitted with the AME2020 S_n values. 89

Table 5.1 Half-lives ($T_{1/2}$) and β-delayed neutron emission probabilities (P_{1n}) measured in the present work. Table taken from our publication Ref. [93]. 100

Table 5.2 Table of nuclear input variables that have a significant contribution to the uncertainties of the calculated abundances for $A = 168$-173 in the neutron star merger scenario. 108

Table 5.3 Table of nuclear physics inputs that have a significant contribution to the uncertainties of calculated abundances for $A = 168$-173 in the hot wind scenario. 109

Table 5.4 Table of nuclear input variables that have a significant contribution to the uncertainties of the calculated abundances for $A = 168$-173 for the neutron star merger scenario, with the relative uncertainty of the half-life of ^{168}Sm reduced to 20.0 %. . 112

Table 6.1 Architecture of the neural network optimized by neural architecture search, then by hand. 126

List of Figures

Figure 1.1 Abundance of elements and isotopes in the solar system as a function of mass number. 4

Figure 1.2 Trend of the nuclear binding energy per nucleon for stable isotopes as a function of mass number A. 6

Figure 1.3 Conceptual paths of s- and r-process nucleosynthesis around the neutron magic number $N = 82$. 11

Figure 1.4 Derived solar r-process abundance patterns from Refs. [26] and [27]. 13

Figure 1.5 Scaled elemental abundances of neutron-capture elements in metal-poor stars in the Galactic Halo compared to the r-process abundance pattern observed in the solar system. Figure was taken from Ref. [4]. 14

Figure 1.6 Comparison between PRISM and NUCLEARREACTIONNETWORK.JL, as well as the relative differences in the calculated abundances as a function of mass number A. Figure credit: P. Virally (U Waterloo) [77]. 24

Figure 1.7 Comparison in memory consumption between PRISM and our code NUCLEARREACTIONNETWORK.JL. Figure credit: P. Virally (U Waterloo) [77]. 25

Figure 1.8 Fractions of time for different operations spent in a single run of NUCLEARREACTIONNETWORK.JL [80]. Figure credit: P. Virally (U Waterloo) [77]. 26

Figure 2.1 Basic workings of the r-process under the $(n,\gamma) \leftrightarrows (\gamma,n)$ equilibrium and β-flow equilibrium conditions. 30
Figure 2.2 Comparison of the regions on the chart of nuclides where nuclear masses have been experimentally determined (as listed in the AME2020 [10]) and the nuclei that are predicted to be bound based on FRDM2012 [119]. 38
Figure 2.3 Deviation of the nuclear binding energies modeled by the semiempirical mass formula from the experimentally determined values. 41
Figure 2.4 Residuals of mass excess of the theoretical mass models listed in Table 2.1 as functions of neutron number N, with respect to the experimental nuclear masses from the AME2020 [10]. . . 57
Figure 2.5 Comparisons of the mass models and the experimental masses listed in the AME2020 [10], relative to the predictions of the FRDM2012 for (a) $Z = 28$ (Ni), (b) $Z = 50$ (Sn), and (c) $Z = 64$ (Gd) isotopes. 58
Figure 2.6 Comparisons of the predictions of the r-process abundance patterns employing different mass models. 60

Figure 3.1 Conceptual schematics of the meaning of the value $V_{X_i}\left(E_{\boldsymbol{X}_{\sim i}}(Y \mid X_i)\right)$ in Eq. 3.11. 70

Figure 4.1 Comparison of the AME2003 data with the latest AME2020 data for one-neutron separation energies S_n, illustrated on the chart of nuclides. 84
Figure 4.2 Root mean squared error (RMSE) [MeV] of the neutron separation energies S_n reconstructed by the EBMA models fitted with (a) the whole chart of nuclides and (b) each isotopic chain ($Z = $ const.), compared to the AME2020 [10]. 86
Figure 4.3 Same plot as Figure 4.2, but for (c) each isotonic chain ($N = $ const.), and (d) each isobaric chain ($A = $ const.). 87
Figure 4.4 Maximum a posteriori (MAP) values of the largest weight in the EBMA ensemble determined for each (a) isotopic chain, (b) isotonic chain, and (c) isobaric chain. 90

Figure 4.5 Trends of the sizes of 68% highest density intervals of the EBMA models, fitted with the AME2020 S_n data. 92
Figure 4.6 Comparisons of one-neutron separation energies (S_n) predicted by each mass model used in this study and the experimental masses from the AME2020 [10], relative to the predictions of the FRDM2012. 93
Figure 4.7 Distributions of the new data points in AME2020 compared to AME2003, with respect to the 68% HDIs predicted by the EBMA models fitted with the AME2003 data. 95

Figure 5.1 Half-lives determined in this experiment, in comparison to previous measurements from Ref.[227], as well as theoretical predictions of different models. 98
Figure 5.2 β-delayed one-neutron emission probabilities (P_{1n}) determined in this experiment, in comparison to theoretical predictions of different models. 99
Figure 5.3 Calculated relative *r*-process abundance pattern for the neutron star merger scenario (blue line) and the hot wind scenario (orange). 104
Figure 5.4 Comparisons of 2σ uncertainty bands of the calculated abundance patterns between the current experimental uncertainties of $T_{1/2}$ and P_{1n} values and the uncertainties of $T_{1/2}$ from Ref. [227]. 105
Figure 5.5 A snapshot of the *r*-process path in the neutron star merger scenario at t=0.732 s. 107
Figure 5.6 Calculated relative *r*-process abundance pattern for the neutron star merger scenario. 111
Figure 5.7 Correlation of abundances for $A = 167, 168, 172$, and 173 with the half-life of ^{168}Sm, as well as the first-order sensitivity indices ($S^{(1)}$), in the neutron star merger scenario. 113
Figure 5.8 The abundance evolution, abundance flows, and integrals of the abundance flows of the isotopes ^{168}Sm, ^{168}Eu, and ^{168}Gd as functions of time in the neutron star merger scenario. . . . 114

Figure 5.9 Total abundance flows (the same quantity as the panels (g)–(i) in Figure 5.8), averaged over the generated samples, in the neutron star merger scenario. 115

Figure 6.1 Nuclei included as input variables in the construction of the emulator. 122

Figure 6.2 Comparison of the results between the original nuclear network calculation by PRISM [81] and our ANN emulator, using the test data set, for the neutron star merger scenario, focusing on the rare-earth peak (REP) region $A = 150$–180. . . . 127

Figure 6.3 Same figure as Figure 6.2, but for the neutrino-driven hot wind scenario. 128

Figure 6.4 Panel (a): the emulated abundance pattern and the estimated $\pm 1\sigma$ uncertainty band of one of the test samples, compared to the original (PRISM) calculation. Panel (b): how many of the original calculations of the 10k test samples are covered by the $\pm 1\sigma$ and $\pm 2\sigma$ uncertainty bands, respectively. 130

Glossary

AGB	Asymptotic Giant Branch
AME	Atomic Mass Evaluation
ANN	Artificial Neural Network
BBN	Big Bang Nucleosynthesis
BCS	Bardeen-Cooper-Schrieffer
BH	Black Hole
BMA	Bayesian Model Averaging
BNN	Bayesian Neural Network
BRIKEN	Beta-delayed neutron measurements at RIKEN
CNN	Convolutional Neural Network
CNO	Carbon-Nitrogen-Oxygen
CPU	Central Processing Unit
DFT	Density Functional Theory
DZ	Duflo-Zuker
EBMA	Ensemble Bayesian Model Averaging
EDF	Energy Density Functional

EM	Expectation Maximization
ETFSI	Extended Thomas-Fermi Plus Strutinsky Integral
FAM	Finite Amplitude Method
FRDM	Finite-Range Droplet Model
GP	Gaussian Process
GPU	Graphical Processing Unit
GRB	Gamma-Ray Burst
HDI	Highest Density Interval
HF(B)	Hartree-Fock(-Bogoliubov)
HMC	Hamiltonian (Hybrid) Monte Carlo
KUTY	Koura, Uno, Tachibana, and Yamada
LDM	Liquid-Drop Model
MAP	Maximum A Posteriori
MCMC	Markov Chain Monte Carlo
MHD	MagnetoHydroDynamic(s)
NAS	Neural Architecture Search
NS	Neutron Star
NUTS	No-U-Turn Sampler
ODE	Ordinary Differential Equation
PDF	Probability Density Functions
PRISM	Portable Routines for Integrated nucleoSynthesis Modeling
QRPA	Quasi-particle Random-Phase Approximation

ReLU Rectified Linear Unit

REP Rare-Earth Peak

RMS(E) Root Mean Squared (Error)

RIKEN RIkagaku KENkyūjo, a scientific research institute in Japan

TRIUMF Canada's particle accelerator centre

WS Weizsäcker-Skyrme

Acknowledgments

I would like to begin by acknowledging that most of the work presented in this thesis was performed at TRIUMF, located on the traditional, ancestral, and unceded territory of the Musqueam People.

I express my special gratitude to my supervisors Prof. Reiner Krücken and Dr. Iris Dillmann for their continuous support throughout my graduate studies and for providing me with great learning and research opportunities.

I also thank Dr. Matthew R. Mumpower and Prof. Rebecca Surman for introducing me to the field of theoretical nuclear astrophysics and for patiently working with me.

I was lucky to have great colleagues during my studies: Luca Egoriti, James McNeil, Edward Thoeng, Daniel Yates, Guy Leckenby, Nikita Bernier, Roger Caballero-Folch, and Chris Griffin, to name a few.

Although not included in the current thesis, I thank Prof. Nils Paar, Ante Ravlić, Dr. Futoshi Minato, Prof. Jonathan Engel, and Evan Ney for providing their theoretical calculations and for helping me with my project.

All my friends with whom I was lucky enough to spend time are also a big part of the reason I was able to reach this point. Especially, I would like to give a special thanks to all my friends I met in Canada, and my best friends in Japan, Andras Takahiro Suzuki and Hiroki Sato.

I also thank my family for always supporting me even though I am far away from them.

Finally, I thank Danielle Jamieson and our cat April, for always being by my side and for being my inspiration.

Chapter 1

Introduction

When I was born,
Earth shed tears to equal my birth weight.
I was made from a bit of Heaven and Earth.
— Shuntarō Tanikawa,
To Go Home (1979)

All of the visible matter around us, including ourselves, is made of combinations of electrons, protons, and neutrons, together forming what we know as chemical elements. The wide variety of chemical elements in nature, from hydrogen to uranium, can be characterized by their atomic nuclei, which are composed of specific numbers of protons and neutrons. While protons and neutrons (nucleons) are not elementary particles themselves—they are made of elementary particles called quarks bound together by another type of elementary particles called gluons, which mediate the strong force described by the theory of quantum chromodynamics (QCD)—it is possible to provide rather coherent descriptions of atomic nuclei by treating protons and neutrons as the fundamental degree of freedom. We will see some aspects of it in this chapter. The field of physics based on the nucleon degree of freedom is called (low-energy) nuclear physics.

Nuclear astrophysics, which is the focus of the current thesis, is at the intersection of nuclear physics and astrophysics, where we aim to understand the origin of chemical elements based on our knowledge of stellar structure and evolution, and the nuclear physics processes that occur inside stars and explosive astrophysical

events. The field of modern nuclear astrophysics was formalized by the seminal works of Burbidge et al. (1957) [1] and Cameron (1957) [2]. The general term which describes the production of chemical elements in the Universe is called *nucleosynthesis*.

1.1 Structure of the Thesis

In this chapter (**Chapter 1**), we will first review various nucleosynthesis processes, with an emphasis on the processes which produce the heaviest elements in nature and their relations to the properties of atomic nuclei (**Section 1.2**). Among many nucleosynthesis processes, the focus of the current thesis is the rapid neutron capture process (*r*-process), which synthesizes the heaviest elements in the Universe (Section 1.2.2). The *r*-process is believed to occur in neutron-rich and explosive astrophysical environments, such as compact binary mergers and some types of (core-collapse) supernovae, involving thousands of neutron-rich nuclei and diverse types of nuclear reactions. Thus, modeling of the observables of the *r*-process, such as abundance patterns and electromagnetic emissions, requires detailed descriptions of the astrophysical environments and the properties of neutron-rich nuclei, which are currently not very well understood.

In order for an accurate understanding of the *r*-process, it is essential to quantify the uncertainties of nuclear physics models as well as their effect on the *r*-process observables. In this thesis, we focus on the *r*-process abundance pattern in the solar system, which is one of the most well-known observables. Therefore, in **Section 1.3**, a method to compute the nuclear abundance evolution in astrophysical environments called a nuclear reaction network and its computational aspects will be discussed.

The current thesis puts an emphasis on the nuclear physics of the *r*-process, which will be discussed in **Chapter 2**. **Section 2.1** discusses the peak structures in the observed solar *r*-process abundance pattern and their relations to the nuclear physics processes. In **Section 2.2**, different approaches for describing nuclear masses, which are some of the most fundamental properties of atomic nuclei, will be discussed. As shown in this section through an example of nuclear mass models, theoretical predictions of the properties of nuclei start to diverge and become

uncertain without experimental constraints, especially in the neutron-rich region, where the *r*-process operates.

Statistical frameworks are powerful tools for *uncertainty quantification* in mathematical (numerical) models (e.g. nuclear mass models, nuclear reaction network models, and so on). Furthermore, they can also be used for identifying influential inputs of the models that contribute the most to the uncertainty of the prediction of the models. This is called a *sensitivity analysis*. In **Section 3**, an overview of the statistical and machine learning techniques used in the main contributions of the current thesis (Chapters 4, 5, and 6) will be given.

Section 3.1 discusses the framework of Bayesian statistics. **Section 3.2** describes the Markov chain Monte Carlo (MCMC) method, which is often used for parameter estimation in Bayesian statistics. The statistical framework and computational techniques introduced in these sections are applied to the uncertainty quantification of theoretical nuclear mass models in **Chapter 4**, using the mass models described in Section 2.2.

Section 3.3 explains the basics of the variance-based sensitivity analysis method. This method defines sensitivity as a contribution of the input(s) to the variance (propagated uncertainty) of the output of a numerical simulation. In **Chapter 5**, this method has been applied to nuclear reaction network abundance calculations, investigating the influence of the newly measured β-decay properties and their uncertainties for a number of neutron-rich nuclei in the rare-earth region. It provides a more statistically rigorous framework for sensitivity analyses than previous studies and provides more detailed information on how the inputs affect the predicted abundance patterns.

Section 3.4 introduces the basics of highly flexible machine learning models called artificial neural networks (ANNs). In **Chapter 6**, ANNs have been used to model the changes in abundance patterns predicted by nuclear reaction network calculations, as a result of changes in the values of nuclear physics inputs, such as nuclear masses and half-lives of the nuclides of interest. In this context, the ANN models are considered to be *emulators* of the nuclear reaction network calculations. These emulators are able to compute abundance patterns significantly faster than full nuclear reaction network calculations, therefore, they potentially enable statistical analyses, such as variance-based sensitivity analyses, at a much larger

scale.

In **Chapter 7**, a summary of the contributions of the current thesis is given and the outlook is discussed.

1.2 Synthesis of Elements

Figure 1.1 shows the abundance pattern of elements and isotopes in the solar system. This abundance pattern contains rich information on how the elements have been synthesized in our solar system. It is mainly obtained from observation of the intensity of elemental absorption and emission lines in the Solar spectrum, and analyses of a specific class of meteorites that retain the isotopes that existed in the early Solar system [3]. Below, a brief overview of the origin of elements from the lightest elements to the heavy elements past iron is given. Especially the rapid neutron capture process (*r*-process), which creates the heaviest elements that exist in the Universe and is the focus of the current thesis, will be discussed in more detail.

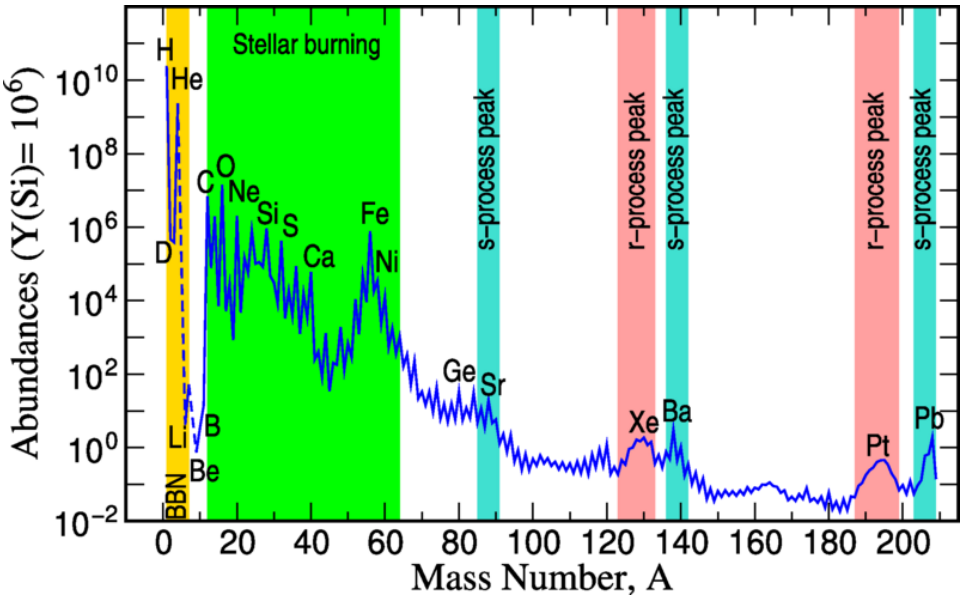

Figure 1.1: Abundance of elements and isotopes in the solar system as a function of mass number. Figure adapted from Ref. [4]

1.2.1 Nucleosynthesis up to Iron

Synthesis of Elements in the Big Bang and by Cosmic-Ray Spallation

The first nucleosynthesis process took place minutes after the Big Bang, which produced the lightest nuclei such as ^{1,2}H, ^{3,4}He, and ^{7}Li. This is called Big Bang nucleosynthesis (BBN). About 75% of the produced nuclei are ^{1}H (protons), and the rest of the 25% is mainly ^{4}He (α-particles). The other nuclei are produced in orders of magnitude smaller amounts. The disagreement between theoretical predictions and observations on the amount of ^{7}Li is a longstanding problem and is referred to as the "lithium problem" [5, 6].

The next lightest elements observed in the Solar System are ^{6}Li, ^{9}Be, ^{10}B and ^{11}B, whose abundances are about six orders of magnitude smaller than the species produced in the BBN. However, these are not chronologically the next species to be produced after the BBN. This is because the BBN only produces negligible amounts of these nuclei and even if they are produced, they would be quickly consumed in the early stage of stellar burning due to their low Coulomb barriers. Due to their unknown origin at that time, Burbidge et al. (1957) referred to their production mechanisms as "*x*-process". Today, their production is attributed to spallation reactions of CNO nuclei (see the following paragraphs for details) abundant in stellar atmospheres (cosmic-ray spallation) [7].

Stellar Burning

The production of nuclides up to the iron peak occurs within the cores of stars through nuclear fusion reactions. It is often referred to as "stellar burning". The reason why stellar burning can only produce elements up to iron is that, as shown in Figure 1.2, fusion reactions up to the iron peak release energy due to increasing binding energies towards heavier masses. This creates internal pressure to prevent stars from collapsing gravitationally. However, fusion reactions can no longer release energy beyond the iron peak. The increase in proton number means higher Coulomb barriers; therefore, stellar burning of heavy elements is highly hindered. Today, the following stellar burning phases are known to exist: hydrogen burning, helium burning, carbon burning, neon burning, oxygen burning, and silicon

burning. Depending on its total mass, a star may go through one or several of these burning stages. Only massive stars with more than 8 solar masses (8 $M_{\odot}$) can ignite all burning phases and end their lives in a core-collapse supernova [8, 9].

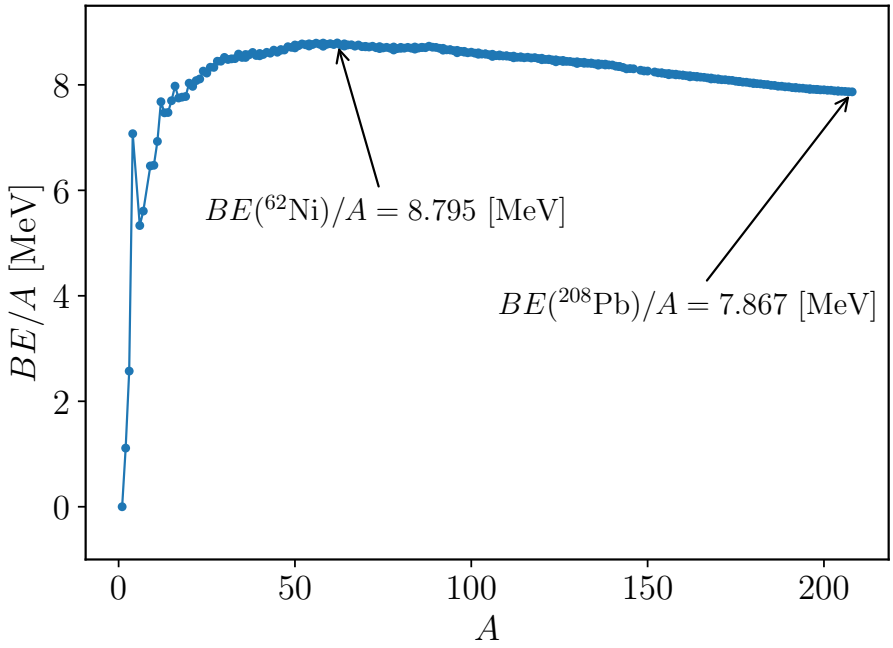

Figure 1.2: Trend of the nuclear binding energy per nucleon (BE/A) as a function of mass number A for stable isotopes up to ^{208}Pb. The most tightly bound nucleus is ^{62}Ni with $BE/A = 8.795$ MeV. The data are from AME2020 [10].

Star formation begins in an interstellar gas cloud, which consists mainly of primordial hydrogen and helium. Stars formed at late stages are already "contaminated" with material from previous star generations (metallicity). The gas cloud starts to contract due to the attractive gravitational force, and the gravitational potential energy is converted into thermal energy and radiation. As its density increases and the atoms are ionized, the radiation starts to raise the temperature and pressure [8, 11].

When the central temperature reaches about 10 million Kelvin, hydrogen burn-

ing begins. Stars undergoing hydrogen burning occupy a particular band on a graph of luminosities and effective temperatures (Hertzsprung-Russell diagram) and are referred to as main-sequence (MS) stars. This is the longest stage in the life of a typical star (e.g., roughly 10^{10} years for a 1 $M_\odot$ star) [9, 11].

In principle, hydrogen burning fuses four ^{1}H nuclei to produce a ^{4}He nucleus. However, the probability of this direct reaction occurring is too small to explain the luminosity of stars. In fact, ^{4}He nuclei are produced in a sequence of nuclear reactions in the core called the pp (proton-proton) chains. The timescale of the process is dominated by the first reaction in the pp-chains, which is $p + p \to d + e^+ + \nu$, where d, e^+, and ν denote a deuterium (^{2}H) nucleus, a positron, and a neutrino, respectively. This reaction is slow because, in addition to the Coulomb barrier of the protons, it involves the weak interaction, which converts a proton into a neutron in the field of a second proton, unlike many other stellar fusion reactions, which are mediated by the strong nuclear force and the Coulomb force [8, 9]. For the Sun, the beginning of the pp-chains is estimated to be 4.5 Gy ago and it would take 4.8 Gyr from now to exhaust the hydrogen in the core [8, 12]. If stable carbon or nitrogen nuclides from previous star generations are present in the stellar plasma, the CNO cycles can alternatively complete the net reaction of hydrogen burning.

After all the hydrogen is consumed in the core, the star further contracts due to the gravitational force and it increases the temperature. Eventually, the abundant ^{4}He in the core is ignited and produces mainly ^{12}C via the triple-α process and ^{16}O by another capture of an α-particle. This is called helium burning. For stars whose masses are in the range $0.5M_\odot \lesssim M \lesssim 8M_\odot$, helium burning is the last stage of core burning. They eventually evolve into the stage called asymptotic giant branch (AGB), where the carbon-oxygen core is surrounded by a burning helium shell, and the helium burning region is surrounded by a hydrogen burning shell [8, 13].

Stars with masses larger than $\sim 8M_\odot$ undergo hydrostatic carbon burning after the helium is consumed and the temperature increases due to a further contraction of the core. Carbon burning creates a core mainly consisting of ^{16}O, ^{20}Ne, ^{24}Mg, and ^{23}Na. If the initial masses of stars exceed $\sim 10M_\odot$, they are capable of igniting even further hydrostatic burning stages, called neon burning, oxygen burning, and silicon burning. Through significantly more complicated networks of nuclear reactions, they eventually produce nuclei in the mass $A = 52$-56 region. The nu-

clei in the mass region are commonly referred to as iron-peak nuclei, which are some of the most tightly bound nuclei (Figure 1.2). While silicon burning creates a Fe/Ni-core made of iron-peak nuclei such as ^{56}Ni, ^{54}Fe, and ^{56}Fe, the details of the composition of the products sensitively depend on the degree of neutron excess in the stellar plasma and its thermodynamical conditions such as temperature and density [9, 11].

Stellar Explosions

The composition of nuclei synthesized in the core, however, deviates from the abundance pattern observed in the solar system. This is because the synthesized nuclei need ejection mechanisms, and such explosive processes significantly alter the composition of the nuclei. Core-collapse and thermonuclear supernovae are considered to be responsible for such an ejection of material, including iron peak nuclei, into the interstellar medium [8].

Core-collapse supernovae occur at the end of the lives of massive stars ($\gtrsim 8M_\odot$). Depending on specific absorption lines in the optical spectra, which reflect the composition of the outer layers, they can be categorized into type II, Ib, and Ic supernovae. At the end of the silicon burning, the core becomes electron-degenerate. Electron degeneracy pressure arises due to a large density of electrons confined in the same volume; therefore, electrons start to occupy high-momentum states since multiple electrons cannot occupy the same state due to the Pauli exclusion principle. When the mass of the core reaches the Chandrasekhar limit ($\sim 1.4M_\odot$), the electron degeneracy pressure can no longer support its mass and the core instantaneously collapses (on a timescale of less than a second [14]) due to gravity. Once the core surpasses nuclear density ($\sim 2\times10^{14}$ gcm^{-3}, according to the liquid-drop model, Section 2.2.1), where the nuclear force becomes repulsive, it rebounds and generates an outward shock wave. The hot and dense core forms a protoneutron star as a result of the photodissociation of the iron-peak nuclei and electron captures.

By the time the shock wave reaches the outer edge of the core, the kinetic energy is lost due to the emission of neutrinos. Although the mechanism of revival of the shock is not yet fully understood, the neutrino-matter interaction is considered

to be the predominant process (neutrino-driven wind). From the shock propagating through layers with different compositions, a range of elements such as ^{16}O, ^{28}Si, ^{36}Ar, ^{40}Ca ("α-nuclei") and iron-peak nuclei, predominantly ^{56}Ni are synthesized and ejected [15].

Another major mechanism of supernovae is due to a thermonuclear explosion. This is classified as type Ia supernovae because of the presence of silicon absorption lines in the spectra. It is believed that the viable progenitors of type Ia supernovae are carbon-oxygen (C+O) white dwarfs in a binary system accreting hydrogen- or helium-rich matter from a non-degenerate companion (single-degenerate scenario); a C+O white dwarf plunging into the envelope of a giant companion and merging with its core (core degenerate scenario); or a merger of two C+O white dwarfs (double-degenerate scenario). White dwarfs are the final stage of low- to intermediate-mass stars, which are supported by the electron degeneracy pressure. Although detailed mechanisms of triggering a thermonuclear explosion are still actively studied, in general it is caused by a white dwarf approaching the Chandrasekhar limit through accretion of matter or a merger, and heating due to gravitational compression triggers a thermonuclear explosion (Ref. [16] and references therein). The explosion mainly produces iron-peak nuclei as well as some intermediate-mass nuclei in the outer layer of the white dwarf, although the yields depend on the composition of the core and the detail of the explosion [8, 17, 18]. The notable fact is that the light curve of type Ia supernovae is predominantly powered by ^{56}Ni, which undergoes a β-decay to ^{56}Cu, and finally to ^{56}Fe. About half to two thirds of the ^{56}Fe in the Galaxy is considered to have been produced by type Ia supernovae [9].

1.2.2 Evidence of the Rapid Neutron Capture Process

As the proton number increases past the iron peak, nucleosynthesis via charged-particle and fusion reactions becomes increasingly unlikely due to the large Coulomb barriers. The decreasing trend of nuclear binding energy per nucleon past iron (Figure 1.2) also indicates that further fusion reactions cannot produce energy. Conditions achieved within the explosions of stars discussed in the previous section also tend to produce iron-peak nuclei, due to their large binding energies. In order to

produce heavy elements (Pb and beyond), neutron capture processes are necessary.

Solar Abundance Pattern

The first evidence of neutron capture processes can be seen in the double-peak features of the solar abundance pattern (Figure 1.1) around $A \sim 130$ and 140, as well as $A \sim 195$ and 205, corresponding to the neutron magic numbers $N = 82$ and 126, respectively. The higher and lower mass peaks of the double peaks are believed to originate from the slow neutron capture process (*s*-process) and the rapid neutron capture process (*r*-process), respectively, through accumulation of abundances due to the increased stability at neutron magic numbers (e.g., smaller neutron capture cross sections). In the *s*-process, neutron captures occur on a timescale of 10–100 years, which is slower than that of β-decays. On the other hand, in the *r*-process, the typical timescale of neutron captures is on the order of millisecond or less.

The *s*-process, which occurs in asymptotic giant branch (AGB) stars and during the hydrostatic burning phases of massive stars ($> 8M_{\odot}$), synthesizes heavy elements through an iteration of neutron captures and β-decay near the valley of β-stability [19]. Due to its low neutron density ($10^{6\text{–}12}$ cm^{-3}) in the environment, there is sufficient time (tens to hundreds of years) for the nuclei to decay back to stability, despite their long half-lives of the nuclei near the valley of stability. The wide range of neutron densities gives rise to *weak* and *main* *s*-processes, where the weak component mainly produces nuclei with $A < 90$ in massive stars and the main component creates nuclei up to ^{209}Bi in AGB stars. Sources of neutrons in the *s*-process are the α-induced reactions $^{13}\mathrm{C} + \alpha \rightarrow {}^{16}\mathrm{O} + n$, occurring in the He- ($\sim$75 %) and C-rich ($\sim$25 %) intershell region during the H-shell burning. Additional neutrons are provided by the $^{22}\mathrm{Ne} + \alpha \rightarrow {}^{25}\mathrm{Mg} + n$ reactions, occuring in the thermal pulses of AGB stars, caused by He-shell flashes (explosive expansions of the He shell) [8, 9]. Approximately half of the abundances of elements heavier than iron that exist in the solar system can be explained by the *s*-process [20].

On the other hand, the *r*-process is believed to occur in neutron-rich (typically neutron density of $\gtrsim 10^{20}$ cm^{-3}) [9] and explosive environments and is responsible for the other half of the abundances of the heavy elements. Due to the fast and successive neutron captures, it operates in the neutron-rich region on the chart of

nuclides. Therefore, in the *r*-process, the masses of nuclei are smaller than in the *s*-process when the nucleosynthesis path encounters the neutron magic numbers. The peaks arise as a result of accumulation of material at the closed neutron shells, where neutron capture slows down. The differences of the masses of nuclei when the nucleosynthesis paths encounter the neutron shell closures cause the double-peak structures observed in the solar abundance pattern (Figure 1.1). Conceptual schematics of this mechanism are shown in Figure 1.3, taking the neutron magic number $N = 82$ as an example.

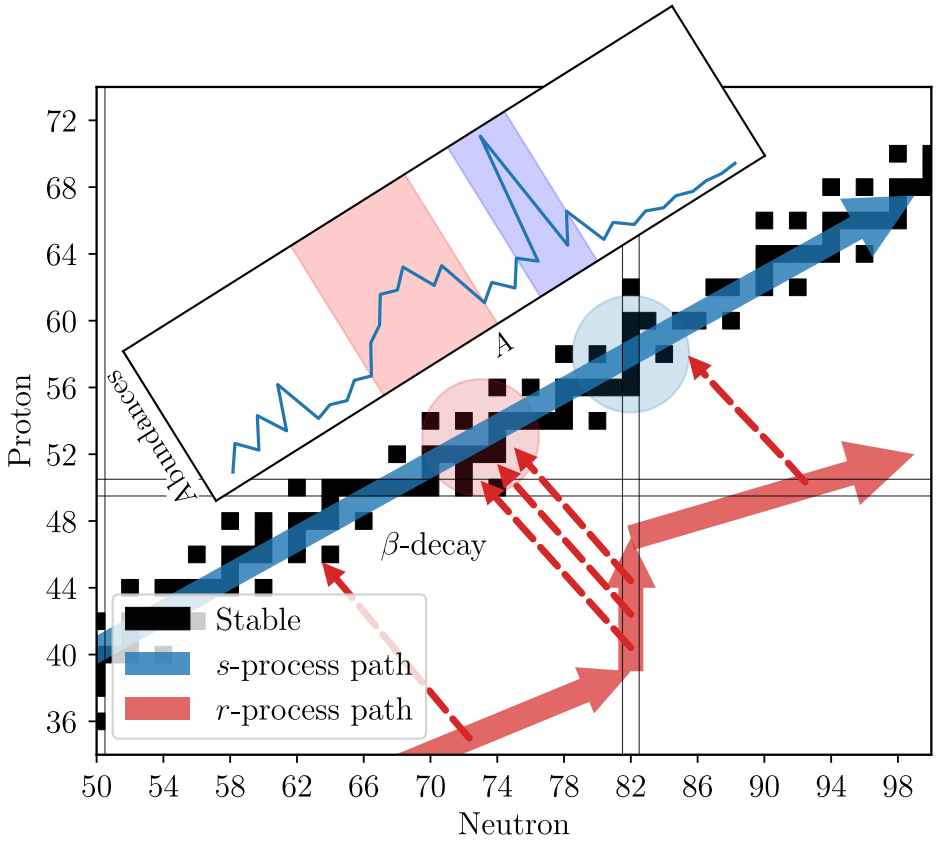

Figure 1.3: Conceptual paths of *s*- and *r*-process nucleosynthesis around the neutron magic number $N = 82$. The circles show the locations on the line of stability where accumulation of material occurs due to the respective neutron capture processes. The inset figure shows the corresponding solar abundance pattern taken from Ref.[21].

Recently, a third neutron capture process called the "intermediate" neutron capture process (*i*-process) has been a topic of investigation [22–25]. This process is believed to operate at intermediate neutron densities of $\sim 10^{15}$ cm^{-3}. Some observations of carbon-enhanced metal poor stars indicate abundance patterns that cannot be explained by a superposition of regular *s*- and *r*- processes, and the *i*-process may be able to explain such observations. The *i*-process was first proposed in Ref. [22] to occur in He-flashes in thermally-pulsing AGB stars and post-AGB stars, where neutrons are provided by the $^{13}\mathrm{C} + \alpha \rightarrow {}^{16}\mathrm{O} + n$ reactions. Recent studies indicate that rapidly accreting white dwarfs in binary systems are also a possible site [25]. The path of the *i*-process is believed to lie between the paths of the *s*- and *r*-processes, 2-6 neutrons away from stability.

In addition, other heavy element nucleosynthesis processes are known to exist as a result of charged particle and photon-induced reactions, such as *rp*-, ν-, νp-, and γ-processes. However, their contributions are limited to just a fraction of the overall elemental abundances compared to the *s*- and *r*-processes and are not apparent in the overall abundance pattern (Figure 1.1).

Since the *s*-process is well understood in terms of the properties of involved nuclei and astrophysical sites, the *r*-process abundance pattern can be derived by subtracting the contribution of the *s*-process from the observed solar abundance pattern. Figure 1.4 shows two different derived *r*-process abundance patterns from Refs. [26, 27]. As discussed above, large peaks are visible at $A \sim 130$ and 195 due to the neutron shell closures at $N = 82$ and 126, which are referred to as the second and third abundance peaks, respectively. These peaks are believed to be formed as a result of a "main" *r*-process, which is responsible for the synthesis of the heavy elements up to and beyond the third peak, as opposed to a "weak" *r*-process, which is primarily responsible for the formation of the first *r*-process peak at $A \sim 80$ [28, 29]. Furthermore, a smaller peak can be seen between the second and third peaks. It is commonly referred to as the *rare-earth peak*. The origin of the peak structures will be discussed in more detail in Section 2.1.1.

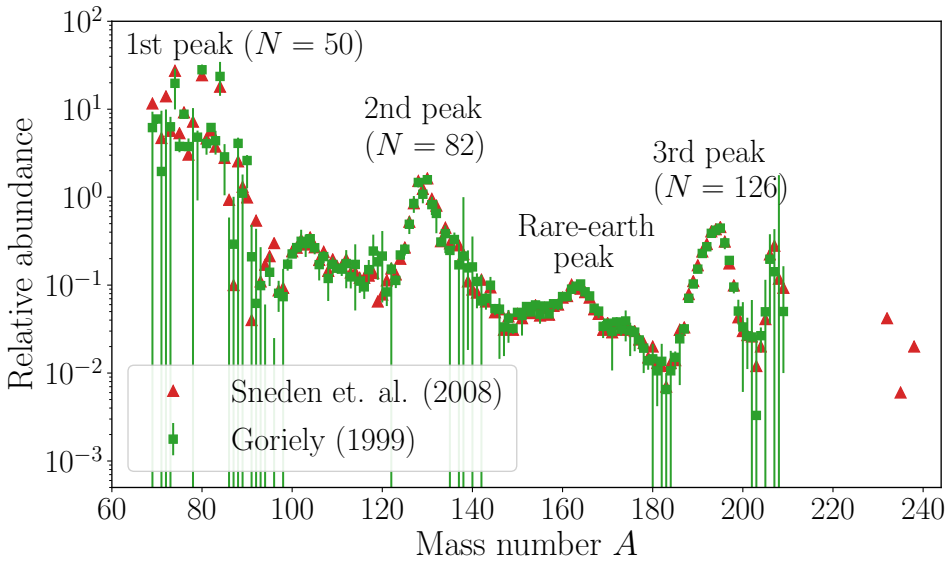

Figure 1.4: Derived solar *r*-process abundance patterns from Refs. [26] (green squares) and [27] (red triangles).

Observations of Metal-Poor Stars

Observations of metal-poor stars in the Milky Way's stellar halo (a spherical population of stars that surrounds our Milky Way Galaxy) provide further evidence for the *r*-process. Metal-poor stars have significantly smaller abundances of metals (elements heavier than hydrogen and helium, e.g. iron) compared to the solar system. In general, the metallicity of the interstellar medium increases as the time passes due to various nucleosynthesis processes. Therefore, metal-poor stars, which are formed in the early stage of the formation of our galaxy, could provide opportunities to isolate signatures of the *r*-process. In fact, observations of metal-poor stars with enhancement in the *r*-process-only elements (elements that are produced exclusively or almost exclusively in the *r*-process, e.g., Eu), show abundance patterns that closely match the solar *r*-process abundance pattern for $Z = 56$–78 (Figure 1.5), providing evidence for a "robust" main *r*-process, which produces nearly identical abundance patterns in separate astrophysical events. Furthermore, some metal-poor stars exhibit significant star-to-star abundance scatter of lighter ($Z \leq 50$) elements, providing evidence for a weak *r*-process, most likely

originating from different mechanisms than the main *r*-process.

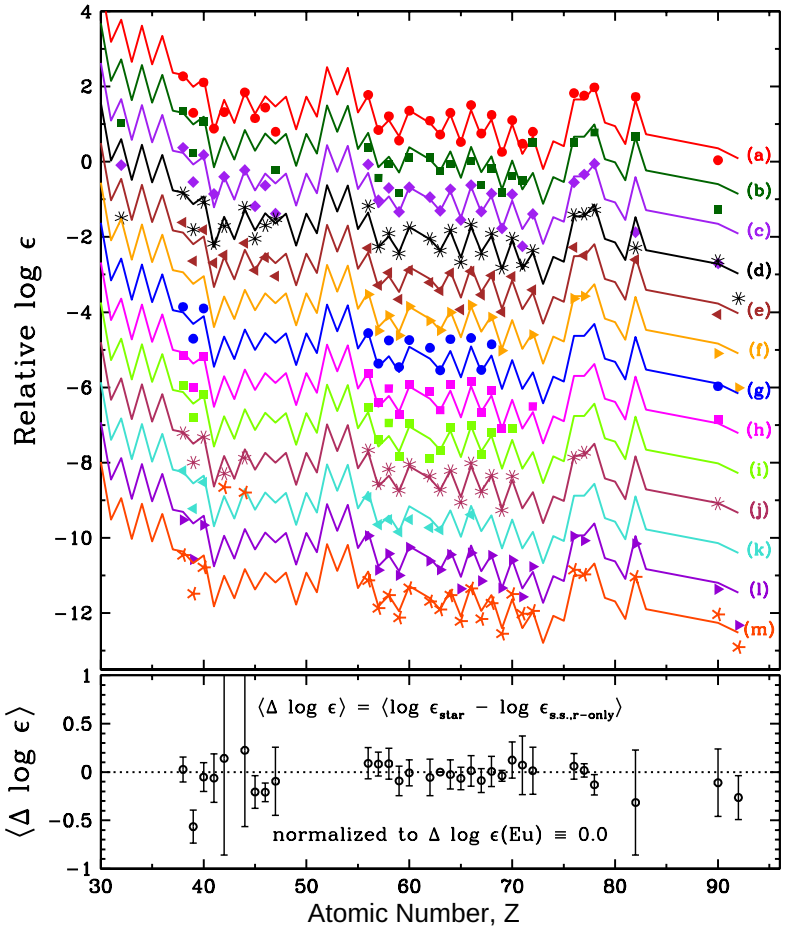

Figure 1.5: Scaled elemental abundances of neutron-capture elements in metal-poor stars in the Galactic Halo compared to the *r*-process abundance pattern observed in the solar system (solid lines). The abundance patterns are scaled to match the abundances for Eu ($Z = 63$). The vertical shift of each abundance pattern is for display purposes. Labels (a)–(m) correspond to different metal-poor stars. The bottom panel shows deviations of the mean abundances of the metal-poor stars from the *r*-process solar abundance pattern. Figure was taken from Ref. [4].

Kilonovae

A more direct evidence connecting the *r*-process nucleosynthesis to a specific astrophysical event was obtained as an electromagnetic counterpart of the gravitational wave event GW170817, originating from a binary neutron star merger [30, 31]. The observation agreed well with predictions of light-curves powered by the radioactive decays of the *r*-process nuclei synthesized in the neutron star merger ejecta [32, 33]. Such emission of light is called a "kilonova" or "macronova". In order to model the evolution of the spectra of the kilonova, at least two components originating from different types of ejecta were necessary: the "blue" emission peaking at optical wavelengths a day after the merger, which mainly contains light *r*-process elements originating from the fastest moving outer layer of the ejecta, and the "red" component peaking at near-infrared wavelengths roughly a week after the merger, which contains lanthanide/actinide elements whose optical opacity is largely due to their complex electron shell structures. The blue component was found to be consistent with a combination of hot and fast dynamical ejecta from the collision interface and neutrino-driven wind ejecta, and the red component most likely originates from the post-merger accretion disk outflows (see the following section for the descriptions of the ejecta). These features of the light curve were interpreted as clear indications of the production of heavy *r*-process elements [34, 35].

1.2.3 Possible Sites of the *r*-Process

Due to the observation of the kilonova associated with GW170817, which showed evidence of the synthesis of heavy elements, binary neutron star mergers are now considered to be one of the most promising candidates as the *r*-process site. While the inferred nucleosynthesis yield and rate of GW170817 suggest that such mergers could be responsible for most of the *r*-process nuclei in the solar system [34, 35], existence of other sources is not excluded. Below, a brief review of some of the possible sites of the *r*-process are given.

Neutron Star Mergers and Neutron Star-Black Hole Mergers

Since the main *r*-process requires a neutron-rich environment and explosive mechanisms to eject material, mergers of binary neutron stars (NS mergers) were considered to achieve such conditions long before the observation of GW170817 [36–39]. Ejecta of NS mergers can be categorized into the following three components [4]: (i) dynamic ejecta, (ii) neutrino-driven wind ejecta, and (iii) accretion disk outflows.

The dynamic ejecta consists of two additional components: a tidal component [38, 40] and a shock-heated component originating from the contact interface [41–43]. The tidal component consists of cold unprocessed neutron-rich material thrown out of the surface of the neutron stars due to the tidal interaction during the final part of the inspiral right before merging. In the tidal component, due to the extremely neutron-rich (low electron fraction Y_e[1]) environment, the heating from radioactive decays, and the relatively slow expansion of the ejecta, the *r*-process produces nuclei up to mass number $A \sim 280$, where fission is the main decay mode. The fission fragments again capture neutrons and may undergo fission several times (fission cycling). In such neutron-rich ejecta, the resulting abundance pattern tends to reproduce the features of the solar *r*-process abundance pattern for $A > 140$, regardless of the modeling details of the fission yields [44, 45]. In the shock-heated component, the high temperature enhances electron and positron capture, making the ejecta less neutron rich [46]. Furthermore, it has been suggested that the electroweak processes due to the neutrino flux from a hypermassive neutron star, which is one of the possible central remnant objects of NS mergers, can make the ejecta even less neutron-rich [47]. However, the extent of the effect depends sensitively on the details of the modeling.

Typically, NS mergers create either a stable NS (maximum mass: 2.2-2.9 $M_\odot$ [48]), a massive NS (MNS, whose mass is larger than the maximum mass of a stable NS and smaller than the maximum mass allowed by uniform rotation), a hypermassive NS (HMNS, whose mass exceeds the maximum mass for a uniformly rotating NS), or a black hole (BH), depending on the mass and spin of the remnant

[1] In neutral plasma, the electron fraction $Y_e = \sum_i Z_i Y_i$ represents the neutron-to-proton ratio, where Y_i and Z_i are the abundance and the proton number of the nuclear species i. For example, $Y_e = 0.5$ implies an equal number of protons and neutrons in the plasma.

[49]. When the central NS remnant is supported by the temperature and rotation, it does not immediately collapse into a BH even when the mass exceeds the maximum mass for a neutron star. Such a central remnant emits neutrinos and creates a neutrino-driven outflow mainly in the polar direction [50, 51]. The outflow is exposed to the flux of neutrinos for a long enough time, therefore, it can reach an equilibrium:

$$\nu_e + n \leftrightarrows p + e^-, \tag{1.1}$$

$$\bar{\nu}_e + p \leftrightarrows n + e^+, \tag{1.2}$$

making the material less neutron-rich or possibly slightly proton rich ($Y_e > 0.5$). This condition only allows for a weak *r*-process, producing elements below the second *r*-process peak ($A < 130$).

After NS mergers, often an accretion disk or torus is formed surrounding the central compact remnant. For a binary system of neutron stars with a typical mass of $\sim 1.35 M_\odot$, including GW170817 where the masses of the individual neutron stars were inferred to be in the range 1.17-1.60 $M_\odot$ [30], the central remnant forms a HMNS and then eventually collapses into a BH [52]. If the lifetime of the HMNS is longer than approximately 1 s, the neutrinos emitted from the hot HMNS can make the ejecta less neutron-rich, with an electron fraction exceeding $Y_e = 0.3$ [53–55]. In this case, similarly to the case of neutrino-wind driven ejecta, only light *r*-process elements can be produced (weak *r*-process). If the lifetime is shorter than roughly 1 s, the effect of the neutrino flux is limited, and the main long-term ejection mechanisms are due to viscous heating and recombinations of α particles. While some nucleosynthesis calculations based on a disk outflow condition report synthesis of the whole range of the *r*-process nuclei, from nuclei with $A \lesssim 130$ to nuclei beyond the third peak with $A \gtrsim 195$, the results are sensitive to the nuclear physics inputs, especially the choice of mass models, as well as the properties of the disk outflow [56, 57].

In the case of NS-BH mergers, mass ejection occurs only if the NS is tidally disrupted by the BH, which is dependent on the mass ratio of the BH and NS and the spin of the BH [58, 59]. Unless the NS directly plunges into the BH, tidal and disk outflow ejecta can be formed. In general, nucleosynthesis in each component

proceeds similarly to the case of NS mergers.

Core-Collapse Supernovae

Core-collapse supernovae have long been considered to be one of the most promising candidates of the site of the *r*-process nucleosynthesis. This is because core-collapse supernovae are explosive events which can produce a proto-neutron star as a remnant. However, as discussed in Section 1.2.1, the ejecta of standard core-collapse supernovae are believed to be powered by the neutrinos emitted during the cooling of a hot proto-neutron star (neutrino-driven wind). Realistic treatments of neutrinos and proto-neutron stars in the simulations of core-collapse supernovae suggest that the ejecta are most likely not very neutron-rich or even proton-rich [60, 61], similarly to the case of the neutrino-driven wind ejecta in NS mergers. Therefore, at most only a weak *r*-process can occur.

However, some special classes of core-collapse supernovae could potentially lead to a successful main *r*-process. One of such possibilities is a magneto-rotational supernova, in which a jet-like explosion, induced by a core collapse with a strong magnetic field and/or a fast-rotating core, accelerates neutron-rich material away from the newly-formed proto-neutron star [35, 62]. The results of relativistic 3D magneto-hydrodynamical simulations for a 15 $M_{\odot}$ progenitor showed a successful *r*-process beyond the third peak at $A \sim 195$ in jet-like ejecta in the polar direction [63]. Further investigations employing various magnetic field strengths show that, especially when the initial magnetic fields are small, the explosions can be deformed and experience longer exposures to neutrinos, therefore, the material becomes less neutron-rich and the *r*-process is weakened [64–66]. While this type of supernovae is expected to be rare, it may also provide the possibility to explain the star-to-star scatter of some of the elements in metal-poor stars (Section 1.2.2) [4, 67].

Another possibility is a collapsar, motivated by the observation of an exceptionally energetic supernova SN 1998bw, which is likely accompanied by a long-duration gamma-ray burst (lGRB) GRB 980425 [68]. In this scenario, a rapidly rotating massive star collapses into a rotating BH, and an accretion disk is formed around the newly-formed BH. Above a certain mass accretion rate, jet-like explo-

sions can occur, causing lGRBs [69]. While the material in the accretion disk is not initially neutron-rich, electrons in the inner disk region become degenerate and start to turn protons into neutrons via electron captures [70]. Such neutron-rich flows may produce a wide range of the *r*-process elements. Multi-dimensional MHD simulations of accretion disk outflows suggest that a large amount of *r*-process ejecta could account for the solar *r*-process abundances even if the event is extremely rare [71, 72]. However, uncertainties remain in the properties of progenitors and explanations for some of the observations, such as lGRB and the presence of a significant amount of ^{56}Ni [4].

1.3 Nuclear Reaction Network Calculations

Nuclear reaction networks are often used to study the evolution of nuclear abundances during astrophysical events. From the evolutions of nuclear abundances, it is also possible to compute the amount of energy release due to nuclear decays. The energy release is particularly important for modeling kilonova lightcurves.

Typically, nucleosynthesis calculations are performed using hydrodynamical trajectories (temporal evolution of temperature and/or density) obtained from tracer particles in hydrodynamical simulations of astrophysical events of interest (post-processing). Tracer particles record the evolution of the positions and thermodynamic properties of the surrounding astrophysical plasma. These simulations also provide an initial composition of nuclear species, which is then evolved through nuclear reaction networks along the astrophysical trajectories.

To obtain the evolution of nuclear abundances, astrophysical trajectories are divided into small time steps and the following system of ordinary differential equations is solved (integrated) for nuclear abundances at each time step:

$$\begin{aligned}\frac{\mathrm{d}Y_i}{\mathrm{d}t} = &\sum_j \mathcal{N}^i_j \lambda_j Y_j + \sum_{j,k} \mathcal{N}^i_{j,k}\, \rho N_A \langle j,k\rangle\, Y_j Y_k \\ &+ \sum_{j,k,l} \mathcal{N}^i_{j,k,l}\, \rho^2 {N_A}^2 \langle j,k,l\rangle\, Y_j Y_k Y_l, \end{aligned} \tag{1.3}$$

where Y_i is the nuclear abundance of the nucleus i, defined so that $\sum_i Y_i A_i = \sum_i X_i = 1$, with X_i being the mass fraction of the nucleus i. ρ is the density of the astrophysical medium, which is obtained from hydrodynamical simulations. The factors $\mathcal{N}^i_j$, $\mathcal{N}^i_{j,k}$, and $\mathcal{N}^i_{j,k,l}$ account for how many particles of nucleus i are created or destroyed in the reaction, while correcting for over-counting due to having the same nuclear species in a reaction. λ_i, $N_A\langle j,k\rangle$, and $N_A\langle j,k,l\rangle$ are one-body reaction or decay rate, two-body reaction rate between nuclei i and j, and three-body reaction rate between nuclei j, k, and l. One-body reactions include reactions of nuclei with photons (photodissociation), electrons (electron capture), and neutrinos. The one-body, two-body, and three-body reaction rates typically depend on the temperature of the medium, which can be given by hydrodynamical simulations, but it is also possible to compute the temperature at each time step using the density and entropy

of the system.

Performing nuclear reaction network calculations and obtaining the final abundance pattern according to the system of coupled ordinary differential equations (ODEs) is considered to be solving an initial value problem with respect to the initial conditions. This system of ODEs is considered *stiff*, since the abundances and their changes in each time step ranges over many orders of magnitude. For a stiff system of ODE, the *implicit Euler* method is often used to obtain the evolution of the abundances. Following the notation in Ref. [73], let $\boldsymbol{Y}(t)$ denote a vector of abundances at time t, then in the implicit Euler method the abundances at time $t+\Delta t$ are obtained as

$$\boldsymbol{Y}(t+\Delta t) = \boldsymbol{Y}(t) + \Delta t\, \dot{\boldsymbol{Y}}(t+\Delta t). \tag{1.4}$$

This method is called "implicit" since it depends on the gradient at the future time $t+\Delta t$. Rearranging Eq. 1.4,

$$0 = \boldsymbol{F}(\boldsymbol{x},\, T(t+\Delta t),\, \rho(t+\Delta t)), \tag{1.5}$$

$$\text{where} \quad \boldsymbol{F} \equiv \frac{\boldsymbol{x}-\boldsymbol{Y}(t)}{\Delta t} - \dot{\boldsymbol{Y}}(\boldsymbol{x},\, T(t+\Delta t),\, \rho(t+\Delta t)), \tag{1.6}$$

where $\boldsymbol{x} \equiv \boldsymbol{Y}(t+\Delta t)$, which are the abundances at the future time step $t+\Delta t$, and T and ρ are the temperature and the density of the environment at the time step, respectively, which come from the astrophysical trajectory. This is obtained from finding a root (solution) of Eq. 1.5 with respect to $\boldsymbol{x}$. The Newton-Raphson (NR) iterative method is commonly used for this root finding problem. Starting from an initial guess of $\boldsymbol{x}_0 = \boldsymbol{Y}(t)$, the iteration at step n can be written as

$$[J_{\boldsymbol{F}}(\boldsymbol{x}_n)] \cdot (\boldsymbol{x}_{n+1} - \boldsymbol{x}_n) = \boldsymbol{F}(\boldsymbol{x}_n,\, T(t+\Delta t),\, \rho(t+\Delta t)), \tag{1.7}$$

where $J_{\boldsymbol{F}}$ is the Jacobian matrix, whose matrix elements can be written as

$$(J_{\boldsymbol{F}})_{i,j} = \frac{\partial F_i}{\partial Y_j} = \frac{\delta_{i,j}}{\Delta t} - \frac{\partial \dot{Y}_i}{\partial Y_j}, \tag{1.8}$$

where $\delta_{i,j}$ is the Kronecker delta. $\frac{\partial \dot{Y}_i}{\partial Y_j}$ is given by taking the derivative of Eq. 1.3

with respect to Y_j.

The Jacobian constitutes a sparse matrix where only $\sim$0.1 % of the elements are non-zero [74–77]. While existing references often use an expression where the inverse of $\boldsymbol{J_F}$ is multiplied to both sides of Eq. 1.7. However, in reality, the inverse is never calculated. This is because an inverse of a sparse matrix is generally not sparse, and calculating such an inverse is computationally inefficient. To solve Eq. 1.7 for $\boldsymbol{x}_{n+1} - \boldsymbol{x}_n$, optimized linear solvers, such as (oneMKL) PARDISO [78], are commonly used.

NUCLEARREACTIONNETWORK.JL

In order to investigate the possibilities of improving the efficiency of the calculation, we have implemented a nuclear reaction network for the *r*-process nucleosynthesis, using the programming language JULIA [79]. This work was performed together with TRIUMF co-op student Paul Virally (University of Waterloo) from Sep.-Dec. 2021 [77]. We chose to use the relatively new language JULIA, which has a high-level syntax that makes the implementation of complex structures and algorithms simpler, while achieving high-performance comparable to traditional languages such as C++ and FORTRAN, upon appropriate code optimizations.

Three months of code development resulted in the ability to compute the abundance patterns for complex astrophysical scenarios of the *r*-process, such as neutron star mergers including fission. Our code is tentatively named NUCLEARREACTIONNETWORK.JL [80]. The accuracy of our code for a neutron star merger scenario is shown in Figure 1.6, and it yields essentially the identical results as the established nuclear reaction network code PRISM [81], which is used for all of the work presented in this thesis.

Our code implements a semi-parallel computation scheme where the stored reaction/decay data are shared among the separate nuclear reaction network calculations that run in parallel on separate CPUs whenever possible. In order to test the effect of the parallelization scheme, the amount of memory usage has been measured as a function of the number of parallel runs of nuclear reaction network calculations. If our parallelization scheme is effective, the amount of memory usage would grow sublinearly with the number of parallel runs. The blue dots in

Figure 1.7 show that the memory consumption of our code grows approximately linearly with the number of parallel runs. The orange dashed line represents the linear growth of memory consumption based on a run of our code with a single CPU. This result implies that our parallel computation scheme is not effective, most likely due to local copies of the reaction/decay data associated with each run. The memory consumption of a run of PRISM (green dot) and its linear extrapolation (green dashed line) are shown in the same figure for comparison. Since PRISM does not implement any parallel calculation scheme, only the memory usage for a single run has been measured.

While our parallelization scheme did not result in an improvement in the efficiency of the calculations, Figure 1.7 shows that our code is approximately four times more memory efficient than PRISM, which is a state-of-the-art nucleosynthesis code. Since our typical run lengths (wall time) are about twice as long as PRISM, overall our code is twice as resource efficient, since the resource consumption is proportional to the requested memory size times the wall time.

Another finding of this development is that, while existing references point out that most of the computational cost is spent on solving the linear equation Eq. 1.7, as shown in Figure 1.8 our profiling of the computational cost points to the possibility that the most computational time is spent on constructing the Jacobian matrices (Eq. 1.8).

Since construction of the Jacobian is computationally expensive, it seems that a reasonable approach to reduce this cost is to offload the operations onto general-purpose graphical processing units (GPUs), which allow for highly parallel computations. However, since elements of the Jacobian matrix can have contributions from multiple nuclear reactions, it has been found that this computation cannot be readily parallelized.

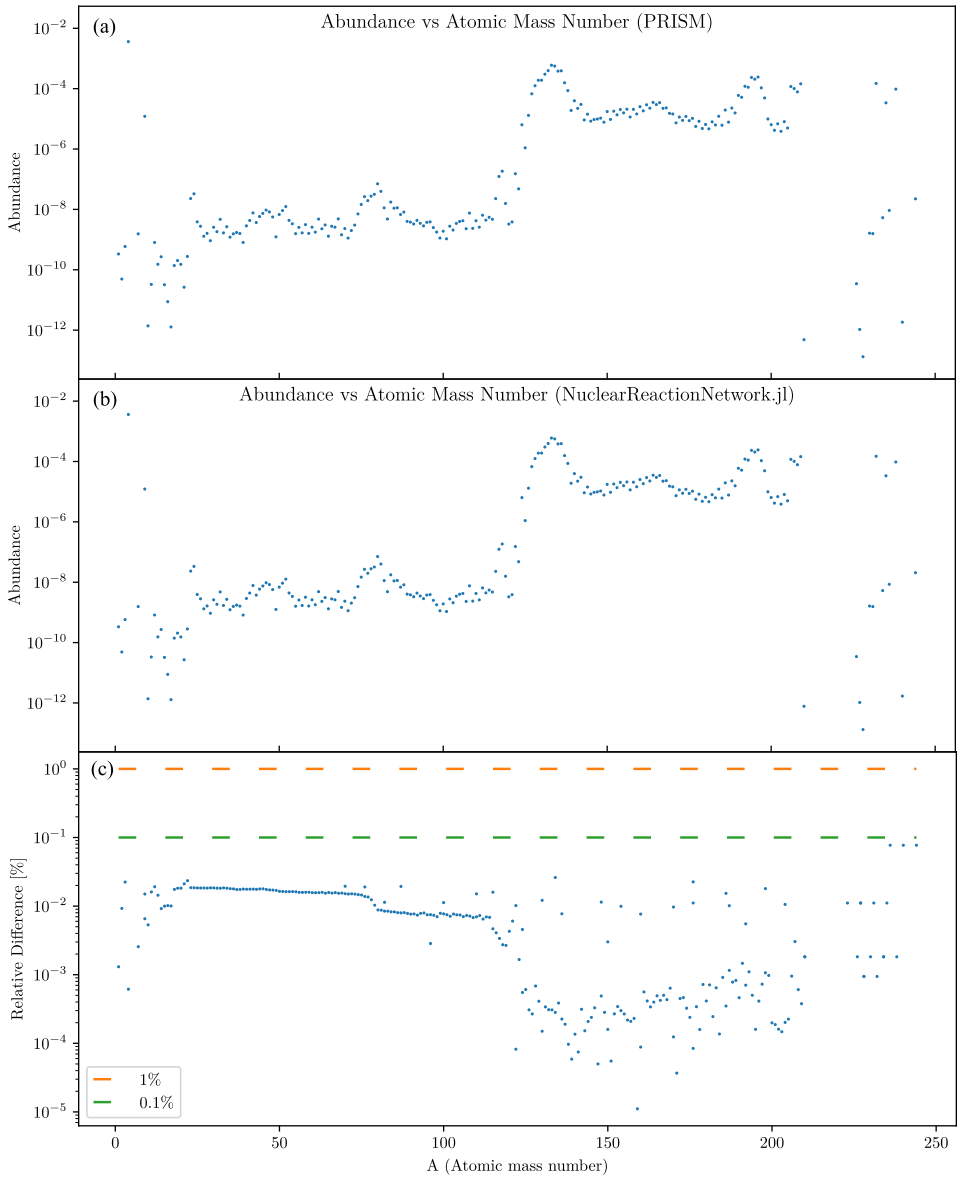

Figure 1.6: Comparison between PRISM [81] (panel (a)), NUCLEARREACTIONNETWORK.JL [80] (panel (b)), and the relative differences (panel (c)) in the calculated abundances as a function of mass number A. A neutron star merger trajectory was used. The relative differences are defined as $100 \times \frac{\left|Y_A^{\mathrm{PRISM}} - Y_A^{\mathrm{NRN.JL}}\right|}{Y_A^{\mathrm{PRISM}}}$ [%]. Figure credit: P. Virally (U Waterloo) [77].

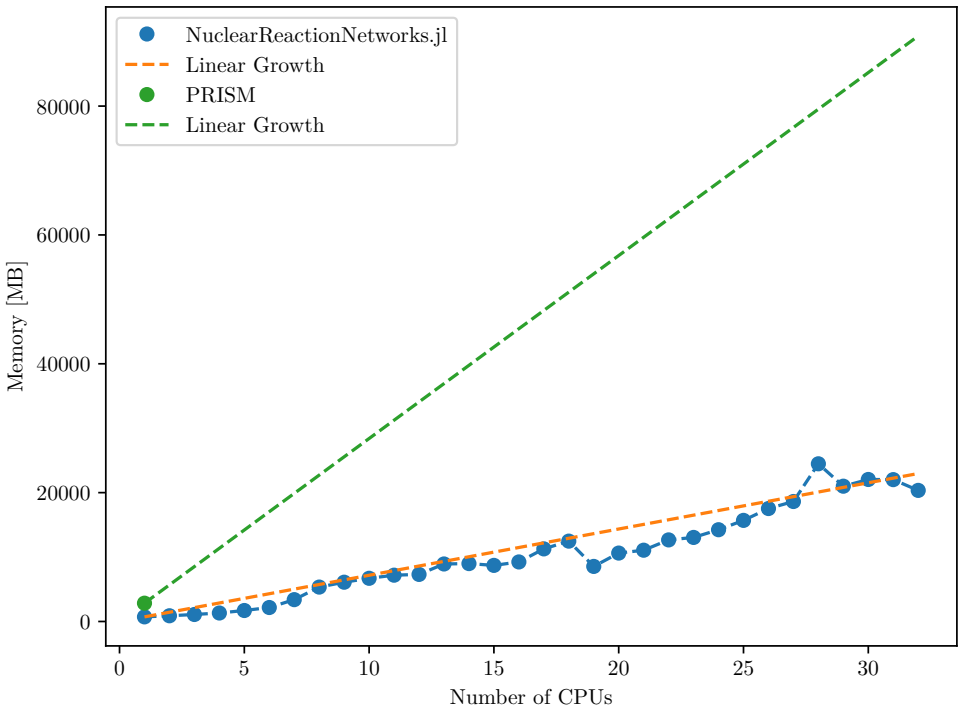

Figure 1.7: Comparison in memory consumption between PRISM [81] and our code NUCLEARREACTIONNETWORK.JL [80] using the hot neutrino-driven wind scenario from Ref. [82]. The x-axis is equivalent to the number of the runs of nuclear reaction network calculations, since one calculation is run on each CPU. Figure credit: P. Virally (U Waterloo) [77].

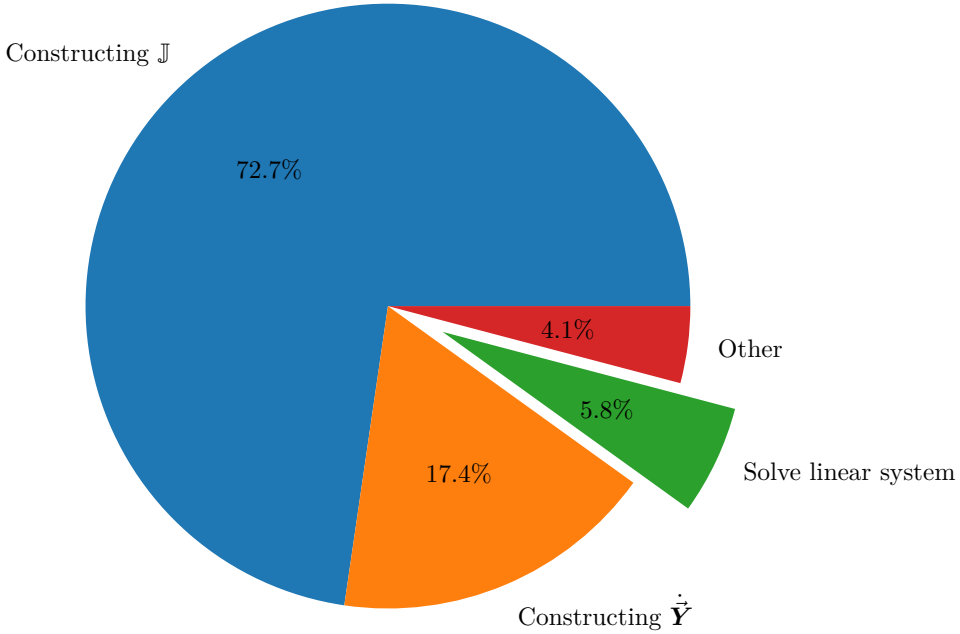

Figure 1.8: Fractions of time for different operations spent in a single run of NUCLEARREACTIONNETWORK.JL [80]. Figure credit: P. Virally (U Waterloo) [77].

Chapter 2

Nuclear Physics of the *r*-Process

So far we have seen that there are multiple possible *r*-process sites, and the composition of the ejecta of each astrophysical scenario differs significantly. Attributing the observed solar *r*-process abundance pattern to specific astrophysical scenarios remains a challenging task. In addition to our understanding of the astrophysical conditions, significant uncertainties also remain in the theoretical descriptions of the properties of nuclei, such as masses, β-decay properties, neutron capture cross sections, fission rates and yields, and so on. In this chapter, we will briefly review how the nuclear physics inputs to the modeling of the *r*-process affect the predictions. An overview of various theoretical descriptions of nuclear masses, which are some of the most fundamental properties of nuclei, will also be discussed.

2.1 The Basics of the *r*-Process Abundance Pattern

2.1.1 Prominent Peaks in the Solar Abundance Pattern

How the nuclear physics properties give rise to some of the features of the *r*-process, such as the second and third peaks, can be understood by assuming some equilibrium conditions. When there are sufficient neutrons in the environment relative to the number of seed nuclei, which capture the neutrons, and the temperature is sufficiently large ($\gtrsim$ 1 GK), a chemical equilibrium between neutron captures (denoted as (n,γ)) and photodissociations (reverse reactions of neutron captures,

denoted as (γ, n)) is established (panel (a) of Figure 2.1). This condition is often achieved in the early stage of the *r*-process nucleosynthesis. Under this condition, the abundance pattern in an isotopic chain (the same proton number Z but different neutron number N), is determined from the ratio of two neighboring isotopes (Saha equation) [4, 8]:

$$\frac{Y(N+1,Z)}{Y(N,Z)} = n_n \cdot \frac{G(N+1,Z)}{2G(N,Z)} \cdot \left(\frac{A+1}{A}\right)^{3/2} \cdot \left(\frac{2\pi\hbar^2}{m_u kT}\right)^{3/2} \cdot \exp\left(\frac{S_n(N+1,Z)}{kT}\right), \tag{2.1}$$

where $Y(N,Z)$ is the abundance of the isotope (N,Z), n_n is the neutron number density, A is the mass number $A = N+Z$, m_u is the nucleon mass, T is the temperature of the environment, and $S_n(N,Z)$ is the one-neutron separation energy of the nucleus (N,Z). $\hbar$ is the reduced Planck constant and k is the Boltzmann constant. $G(N,Z)$ is called a partition function of the nucleus (N,Z), defined as $G = \sum_\mu (2J_\mu + 1)\exp\left(-E_\mu/kT\right)$, where μ is a label of the state (including the ground state), J_μ is its spin, and E_μ is its energy. The dependence of the abundance ratios on nuclear masses is clear through the dependence on the neutron separation energies, which are the mass (binding energy) differences of the neighboring nuclei on an isotopic chain. The abundance maximum in the isotopic chain is obtained when $Y(N+1,Z) \simeq Y(N,Z)$. Since at neutron magic numbers (e.g., $N = 82$, 126), the one-neutron separation energy of the neighboring nuclei $S_n(N+1,Z)$ becomes significantly smaller than $S_n(N,Z)$, accumulation of material tends to occur at the magic numbers. In realistic nuclear reaction network calculations, which do not explicitly assume the $(n,\gamma) \leftrightarrows (\gamma,n)$ equilibrium, the reverse reaction (photodissociation) rates are calculated via a similar expression, the so-called detailed balance [11]:

$$\lambda_{(\gamma,n)} = \langle \sigma v \rangle_{(n,\gamma)} \cdot \frac{G(N,Z)\cdot G_n}{G(N+1,Z)} \cdot \left(\frac{A}{A+1}\right)^{3/2} \cdot \left(\frac{m_u kT}{2\pi\hbar^2}\right)^{3/2} \cdot \exp\left(\frac{-S_n(N+1,Z)}{kT}\right), \tag{2.2}$$

where $\langle \sigma v \rangle$ is a velocity-integrated cross section (the quantity $N_A \langle \sigma v \rangle$ is called a reaction rate), and $G_n = 2$ is the partition function of a neutron. Therefore, the accumulation of material within the isotopic chain inevitably depends on nuclear masses. The nuclei whose abundances are accumulated in the equilibrium are often referred to as "waiting-point" nuclei (panel (b) of Figure 2.1).

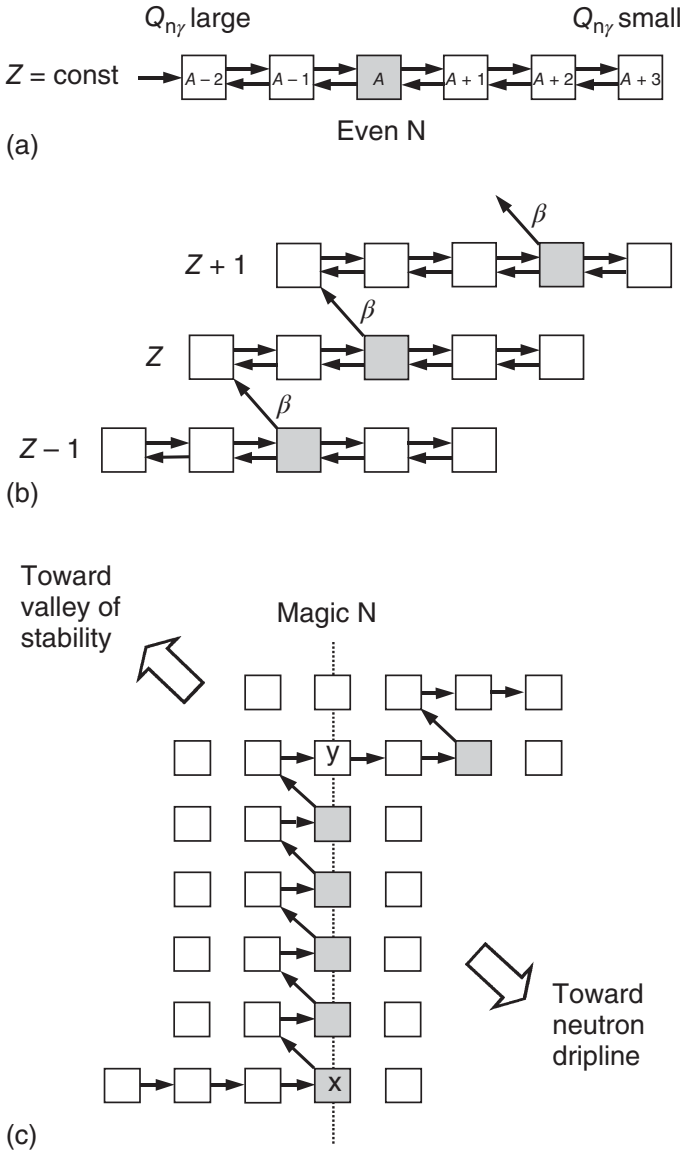

Figure 2.1: Basic workings of the *r*-process under the $(n,\gamma) \leftrightarrows (\gamma,n)$ equilibrium and β-flow equilibrium conditions. Panel (a) shows an isotopic chain in an $(n,\gamma) \leftrightarrows (\gamma,n)$ equilibrium and the gray color indicates a waiting point nucleus (see text for definition), (b) shows how material is transported to subsequent isotopic chains from the waiting point nuclei, and (c) shows a typical path of nucleosynthesis when encountering a neutron magic number. Figure taken from Ref. [8]

The meaning of waiting point nuclei becomes clear by considering another type of equilibrium involving β^--decay (which converts a neutron into a proton). When the $(n,\gamma) \leftrightarrows (\gamma,n)$ equilibrium occurs due to abundant neutrons, the rate at which material is transported from an isotopic chain (proton number Z) to the next $(Z+1)$ is approximately constant [4]:

$$\sum_N \lambda_\beta(N,Z)Y(N,Z) = Y(Z)\sum_N \lambda_\beta \frac{Y(N,Z)}{Y(Z)} = Y(Z)\lambda_\beta^{\text{eff}} = \text{const.}, \tag{2.3}$$

where $Y(Z)$ is the abundance for the whole isotopic chain with proton number Z, λ_β is the β-decay rate, and $\lambda_\beta^{\text{eff}}$ is the β-decay rate weighted by the abundance of each isotope. This is called a "β-flow equilibrium" or a "steady-flow approximation". Thus, the most abundant isotope during the $(n,\gamma) \leftrightarrows (\gamma,n)$ equilibrium (waiting point nucleus) has the largest contribution to $\lambda_\beta^{\text{eff}}$. Therefore, the flow of material into the next isotopic chain has to "wait" for these nuclei to undergo β-decays. Around the neutron magic numbers, the waiting point nuclei tend to be the isotopes with the neutron magic numbers; therefore, the abundance flow goes up vertically along the magic numbers (panel (c) of Figure 2.1). As the nucleosynthesis path approaches the valley of β-stability, the β-decay half-lives become larger, therefore, there is a delay in converting material to higher Z and abundance builds up around these points. This picture qualitatively explains how the second ($A \sim 130$) and third ($A \sim 195$) r-process peaks arise corresponding to the neutron magic numbers at $N = 82$ and $N = 126$.

In neutron-rich conditions such as dynamic ejecta in NS mergers, as the r-process produces increasingly heavy nuclei through the successive neutron captures, photodissociations, and β-decays, the path of nucleosynthesis reaches nuclei where fission is the main decay mode. Fission redistributes the material into smaller masses and has been suggested to be crucial to creating the features in the abundance pattern observed in the solar r-process abundance pattern [45, 51, 83, 84]. The redistributed material can capture neutrons and undergo fission several times (fission cycling). There are various channels of fission, such as spontaneous fission, neutron-induced fission, β-delayed fission, and so on.

2.1.2 The Rare-Earth Peak

In the late time of the *r*-process, when the temperature and the available number of neutrons decrease, the material starts to decay towards stability. This is called the *r*-process *freeze-out*. During the freeze-out, the timescales of neutron captures and β-decays become similar, and the balance of these processes may determine some of the features of the abundance pattern, including the *rare-earth peak* (REP, $A \sim$165) [85–88]. Fission during the freeze-out may also have a significant impact on the formation of the rare-earth peak, as well as the second ($A \sim 130$) and third ($A \sim 195$) abundance peaks [89–91]. Furthermore, some neutron-rich nuclei undergo (one or multiple) neutron emissions following β-decays (β-delayed neutron emission). Since this not only alters the path of the decay chains towards stability, but also provides free neutrons during the freeze-out, it can have a significant effect on the final abundance pattern.

According to this picture, understanding the synthesis of the lanthanides ($A =$ 150-180) in this mass region may allow us to probe the detailed conditions of the freeze-out and the mechanisms of the *r*-process that robustly reproduce the abundance pattern occurring in stars over a wide range of metallicities [85, 86].

The formation of the REP is sensitive to variables that control the neutron density and neutron-to-seed ratio in the late stages of the *r*-process, such as the timescale for the expansion of the material. However, these astrophysical conditions are entangled with nuclear physics processes that provide additional neutrons, of which β-delayed neutron emissions can be a main contributor [92]. The mass region and nuclei responsible for the formation of the REP have previously been inferred [86]. However, the most important nuclei lie about 10–15 mass units away from the valley of stability, and the experimental knowledge of β-decay properties for these neutron-rich isotopes has so far been very limited [93].

Several authors have proposed that during the *r*-process freeze-out the competition between β^--decays and neutron captures shape the REP while the material decays back to stability [85–88, 92, 94]. Neutron emission following β^--decays of neutron-rich nuclei may also have a significant impact on the abundance pattern by providing additional neutrons to the environment and changing the mass number of the nuclide. Therefore, it is important to understand the relationship between

the r-process abundance pattern and nuclear observables, such as β-decay half-lives ($T_{1/2}$) and β-delayed neutron emission probabilities (P_n values). This topic is further explored in Chapter 5.

2.1.3 Modeling of Nuclear Physics Inputs

As illustrated in Figure 2.2 for the case of nuclear masses (also see Section 2.2), the properties of many of the neutron-rich nuclei relevant to the r-process have yet to be experimentally determined. Inevitably, r-process simulations have to rely on the theoretical models of nuclear masses, β-decays, neutron captures, fission, and so on. Here, a summary of nuclear physics models is given that are often used in studies of the r-process.

The nuclear mass is arguably the most fundamental property of a nucleus. This is not only because nuclear masses allow us to probe the properties of the nuclear many-body system, but also almost all the properties of nuclei needed for the r-process depend on the masses. This is because, for any reaction or decay, (differences of) the masses determine the reaction Q-value, which is the energy released (if $Q > 0$) or absorbed (if $Q < 0$) as a result of the reaction or decay. For more detailed discussions on nuclear mass models, see Section 2.2.

β-decay rates are typically obtained using a nuclear mass model as well as a method called quasi-particle random-phase approximation (QRPA), which describes the excited states of the daughter nucleus using *quasi-particles*, which is a convenient concept for describing the pairing correlations in many-body problems (see Section 2.2.4 as well as Chapter 6, 7, and 8 of Ref. [95]). The most commonly used theoretical β-decay rates are the ones of FRDM+QRPA [96–98] (for FRDM, see Section 2.2.3). There exist more microscopic approaches such as the Skyrme Finite Amplitude Method (FAM) [99], which is a computationally efficient implementation of QRPA, employing the Skyrme interaction (Eq. 2.28), and the relativistic QRPA method based on the covariant density functional theory [100]. In all of the above models except for Ref. [96], Gamow-Teller (allowed) transitions as well as first-forbidden transitions are taken into account.

The most common approach for computing neutron capture rates are Hauser-Feshbach statistical model calculations [101]. In such calculations, neutron cap-

ture cross sections are calculated by averaging over resonances in the compound nucleus, resulting in cross sections that vary smoothly with energy. The nuclear level density, the γ-ray strength function, which describes the probabilities of γ-ray transitions of the compound nucleus, and light-particle potentials are necessary for these calculations. There exist several implementations of these calculations often used for the studies of the *r*-process, such as TALYS [102], NON-SMOKER [103], CoH [104], and so on.

While fission is expected to play an important role in the *r*-process under extremely neutron-rich environment, due to its sensitive dependence on the height of fission barriers (energy required to undergo fission) of nuclei in the region where little experimental constraints exist, theoretical modeling remains challenging. Nevertheless, there have been various studies that computed fission barriers [105–108], rates of different fission channels [81, 105, 109–111], and fission yields [112–116].

2.1.4 Roles of Nuclear Physics Inputs

The nuclear physics models discussed above collectively define a nuclear reaction network, and consequently, determine the predictions of *r*-process abundance pattern. However, each nuclear physics input, such as masses, neutron capture rates, β-decay properties (half-lives and neutron emission probabilities), fission properties (rates and yields), etc., plays a different role in the nucleosynthesis process. In this section, we will review the basic roles of such nuclear physics inputs focusing on their effect on the formation of *r*-process abundance pattern.

Nuclear Masses

Under the picture of the "classical" *r*-process, where the equilibrium between neutron capture and photodissociation, i.e., $(n,\gamma) \leftrightarrows (\gamma,n)$, is assumed, the abundance ratios in an isotopic chain (nuclei with the same proton number Z) are determined by the Saha equation (Eq. 2.1). For a given neutron density n_n and temperature T, the abundance ratio at the abundance maximum in an isotopic chain can be approximated as $Y(N,A) \simeq Y(N+1,Z)$. Assuming that for neighboring isotopes, the partition functions are also similar, i.e., $G(N,Z) \simeq G(N+1,Z)$, the

abundance maximum is located at the same neutron separation energy S_n for any isotopic chain. This means that the "path" of the r-process is solely determined by the S_n values given astrophysical conditions (n_n, T). The waiting-point nuclei in each isotopic chain are those where the local abundance maxima occur, and material is transferred into the next isotopic chain.

The effect of nuclear masses, however, is not limited to the location of the r-process path. The masses determine the Q-values (the amount of energy release / absorption) of all reactions and decays; therefore, accurate modeling of nuclear masses is essential for descriptions of every component of nuclear reaction networks.

β-Decay Half-Lives

While the ratio of abundances within an isotopic chain during the $(n,\gamma) \leftrightarrows (\gamma,n)$ equilibrium are determined by the S_n values, the total abundance of a whole isotopic chain $Y(Z) = \sum_N Y(N,Z)$ is affected by β^--decays that connect one isotopic chain to another through ${}^A_Z X_N \rightarrow {}^A_{Z+1} X'_{N-1} + e^- + \bar{\nu}_e$, where X and X' are some elements with proton numbers Z and $Z+1$, respectively, e^- is an electron, and $\bar{\nu}_e$ is an electron antineutrino. While there are enough neutrons in the environment and isotopic chains are connected by successive β-decays, the isotopic chains reach a β-flow equilibrium [117, 118]:

$$Y(Z) \cdot \lambda_\beta^{\text{eff}} = \text{const.}, \tag{2.4}$$

where $\lambda_\beta^{\text{eff}} \equiv \sum_N \lambda_\beta(N,Z) \cdot \frac{Y(N,Z)}{Y(Z)}$ is the effective β-decay rate of the isotopic chain Z. The value of $\lambda_\beta^{\text{eff}}$ is dominated by the half-life of the waiting-point nucleus within the isotopic chain. Since β-decay half-lives and rates are related by $T_{1/2} = \ln 2/\lambda_\beta$, the isotopic abundances are proportional to the effective β-decay half-lives, i.e., $Y(Z) \propto T_{1/2}^{\text{eff}}$. This means that the shape of the final abundance pattern is largely determined by the half-lives of the waiting point nuclei. Especially at the neutron magic numbers such as $N = 50, 82$, and 126, which correspond to waiting points, the half-lives tend to be longer than other nuclei on the path, leading to the peaks of the final abundance pattern at $A \simeq 80, 130$, and 195, respectively.

Since β-decays are responsible for the flow of material towards higher proton

numbers, the timescale of β-decays also determines how far the *r*-process path can reach in terms of proton number within the timescale of the expansion of the astrophysical plasma ($\sim$ 1s). Therefore, the global trend of the theoretical β-decay half-lives is expected to affect the predicted production of heavy nuclei and the extent of the contributions of fission, which is the main decay mode around and below the next neutron magic number $N = 184$.

β-Delayed Neutron Emission

β^--decays of neutron rich nuclei are followed by emissions of one or more neutrons when the neutron separation energy falls below the Q_β value. When the $(n,\gamma) \leftrightarrows (\gamma,n)$ equilibrium breaks down and the material decays back to stability at the late stage of the *r*-process ($\sim$ 1s after the beginning of the *r*-process), which is commonly referred to as the "freeze-out", β-delayed neutron emissions can alter the abundance pattern established during the equilibrium. This is because, in addition to the fact that neutron emissions change the mass number of a nucleus, the emitted neutrons can also be captured during the freeze-out. Since neutrons may be captured by any nucleus in the plasma, depending on neutron density during the freeze-out, β-delayed neutron emissions may globally affect abundance patterns [4]. Therefore, experimental determination and accurate theoretical modeling of β-delayed neutron emission probabilities are necessary to correctly understand the flow of material at the late stage of the *r*-process.

Neutron Capture

During the $(n,\gamma) \leftrightarrows (\gamma,n)$ equilibrium the abundance pattern does not depend on the neutron capture rates (Eq. 2.1). However, if the environment is extremely neutron-rich or the temperature is not hot enough, the equilibrium is not necessarily established. In this case, neutron capture rates are relevant, since the timescale of neutron captures and β-decays become comparable. Furthermore, during the freeze-out, competition of neutron captures and β-decays smoothes out the odd-even staggering in the abundance pattern versus mass number due to the staggering in neutron separation energies [4].

Fission

If the environment is sufficiently neutron rich and the speed of successive β-decays allows the production of nuclei approaching the next neutron magic number $N = 184$, fission can affect the abundance pattern by distributing the fragments of nuclei with large mass numbers into the lighter mass regions [45]. These fragments can again capture neutrons to produce fission nuclei and repeat this cycle several times (fission cycling). Since every fission cycle doubles the number of heavy nuclei, fission can increase the abundance of heavy nuclei relative to light particles. Furthermore, fission also provides free neutrons in the environment and may affect the dynamics of the freeze-out in addition to β-delayed neutron emissions.

Currently, experimental investigations of nuclear fission remain challenging due to the difficulties in producing heavy neutron-rich nuclei.

2.2 Nuclear Mass Models

As discussed in Section 2.1, nuclear masses play an essential role in predicting abundance patterns of the *r*-process nucleosynthesis. However, experimental determination of nuclear masses, especially short-lived neutron-rich nuclei, remains a challenging task. Figure 2.2 shows the chart of nuclides with measured nuclear masses based on the Atomic Mass Evaluation 2020 (AME2020) [10], in comparison to the region where positive one- and two-neutron separation energies (S_n and S_{2n}, respectively) as well as positive one- and two-proton separation energies (S_p and S_{2p}, respectively) are predicted based on the FRDM2012 nuclear mass model (Section 2.2.3). In AME2020, the masses of 2427 nuclides with $N, Z \geq 10$ are listed, while FRDM2012 predicts that 7174 nuclei with $N, Z \geq 10$ exist. It also shows that nuclear masses have been measured almost to the theoretical limit of existence (dripline) on the neutron-deficient side, while the masses of many neutron-rich nuclei have not yet been experimentally studied. Although next-generation radioactive isotope beam facilities such as the now operational FRIB (Facility for Rare Isotope Beams) in the United States, FAIR (Facility for Antiproton and Ion Research) in Germany (which is still under construction), TRIUMF-ARIEL (Advanced Rare Isotope Laboratory) in Canada (under construction), and RIBF at RIKEN in Japan (operational) will be able to produce more neutron-rich nuclei,

precise experimental studies of such short-lived nuclei remain difficult. Since at least in some cases (e.g. binary neutron star merger), the path of the *r*-process is expected to extend all the way to the neutron dripline, which is the neutron-rich limit beyond which nuclei are no longer bound, it is necessary to have reliable theoretical description of nuclear masses to accurately understand the observed *r*-process abundance pattern and other observables.

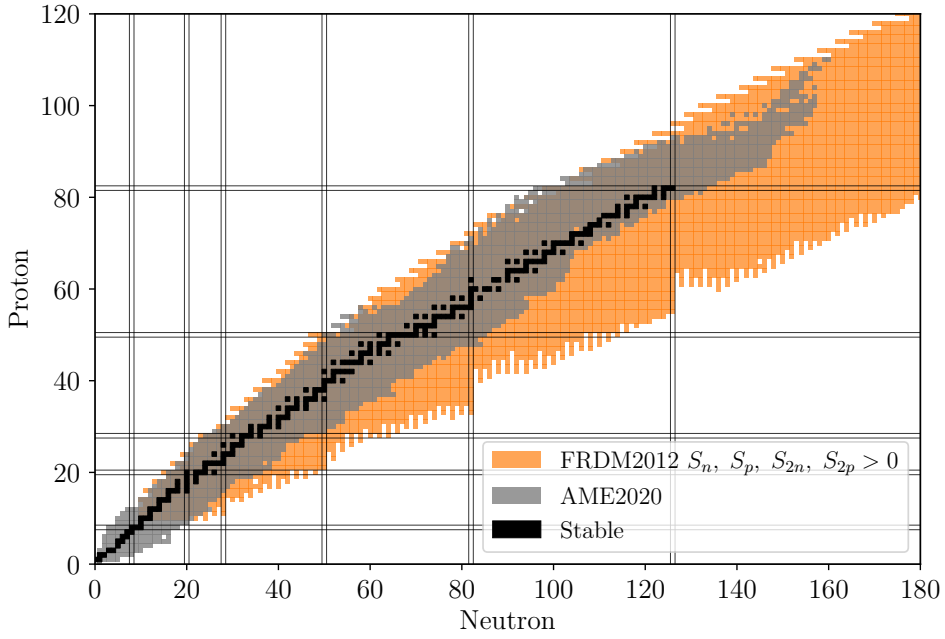

Figure 2.2: Comparison of the regions on the chart of nuclides where nuclear masses have been experimentally determined (as listed in the AME2020 [10]) and the nuclei that are predicted to be bound, i.e. positive one- and two-neutron separation energies (S_n and S_{2n}, respectively) and one- and two-proton separation energies (S_p and S_{2p}, respectively) predicted by FRDM2012 [119] (see Section 2.2.3). The vertical and horizontal lines correspond to the magic numbers.

In this section, an overview of the theoretical concepts of some of the most commonly used nuclear mass models will be provided. In particular, emphasis is placed on the finite-range droplet model (FRDM, Section 2.2.3) and the Hartree-Fock-Bogoliubov (HFB) mass model (Section 2.2.4), which are some of the most

successful mass models using the macroscopic-microscopic (mic-mac) approach and the microscopic approach, respectively.

2.2.1 Liquid Drop Model and Semiempirical Mass Formula

Nuclear masses are often expressed in the form of the binding energy of a nucleus as a function of neutron number N and proton number Z

$$B(N,Z) = \left(NM_n + ZM_p - [M(N,Z) - ZM_e]\right)c^2, \tag{2.5}$$

where M_n is the mass of a neutron, M_p the mass of a proton, $M(N,Z)$ the mass of a nucleus with N neutrons and Z protons, M_e the mass of an electron, and c the speed of light. The fact that the mass of a nucleus is smaller than the sum of the nucleons (neutrons and protons) that constitute the nucleus was first discovered by Aston (1920) [120], according to Ref. [121]. Later, Eddington [122] suggested that the observed mass defect is due to the binding energies of the nuclei. Further measurements of nuclear masses and their interpretation revealed that, for nuclei with more than about twelve nucleons, the binding energy per nucleon $B(N,Z)/A$ stays roughly constant at around 8 MeV, where $A = N + Z$ represents the number of nucleons (see Fig. 1.2). Combined with the observed near constant nuclear densities, this led to the notion that one nucleon in the nucleus interacts only with its nearest neighbors. If all possible pairs of nucleons in a nucleus interact with each other, then the total binding energy of the nucleus would be proportional to the number of pairs $\frac{1}{2}A(A-1)$, meaning that the binding energy per nucleon would be proportional to the mass number A [95]. This leads to the concept of the saturation of the nuclear forces, which originates, among other properties, from its short-range nature. Thus, the roughly constant nucleon density within a nucleus and the relatively sharp drop in density at the surface can be qualitatively explained by the saturation property of the nuclear force.

Based on the observation of how nucleons interact with each other in a nucleus, Weizsäcker [123] and Bethe and Bacher [124] were the first to propose the semiempirical formula (macroscopic mass formula) for nuclear binding energies,

which was inspired by the liquid-drop picture of atomic nucleus [125, 126]:

$$B(N,Z) = a_V A - a_S A^{2/3} - a_C \frac{Z(Z-1)}{A^{1/3}} + a_I \frac{(N-Z)^2}{A} + \delta(A), \tag{2.6}$$

where the values of the parameters were obtained by fitting it to the data from AME2012 [127]:

$$a_V = 15.64; \quad a_S = 17.58; \quad a_C = 0.71; \quad a_I = 23.07 \quad \text{[MeV]}. \tag{2.7}$$

The first term of Eq. 2.6 is called the volume term. Assuming that a nucleus is a sphere with a constant density and a sharp surface, the radius R can be estimated as $R = r_0 A^{1/3}$, where r_0 is empirically determined as $r_0 = 1.2$ [fm]. Thus, this term is proportional to $A \propto R^3$. Similarly, the second term is called the surface term, which is proportional to $A^{2/3} \propto R^2$. It arises from the fact that the nucleons at the surface interact with fewer nucleons than the ones inside the nucleus. The a_C term represents the Coulomb energy, which is proportional to the number of proton pairs ($\propto Z(Z-1)$). The a_I term represents the symmetry energy, which favors a configuration with the same number of protons and neutrons. However, heavy nuclei typically have more neutrons than protons. This is due to the Coulomb repulsion, which makes the potential for a proton shallower. Finally, the term $\delta(A)$ corresponds to the pairing effect. There exist different expressions and dependencies on A of this term, but here we adopt the version by Mendoza-Temis: [126]

$$\delta(A) = \begin{cases} 13.59 \cdot A^{-1/2} & \text{for even-even nuclei,} \\ 0 & \text{for even-odd and odd-even nuclei,} \\ -13.59 \cdot A^{-1/2} & \text{for odd-odd nuclei.} \end{cases} \tag{2.8}$$

This is because like nucleons (neutron-neutron or proton-proton) energetically favor to be in a pair. It can be seen from the experimental observations that, for example, the ground-state spins (sum of the orbital angular momentum and the intrinsic spin) of even-even nuclei (nuclei with even number of neutrons and protons) are always coupled to 0^+ and those of odd-odd nuclei generally show nonzero ground-state spins.

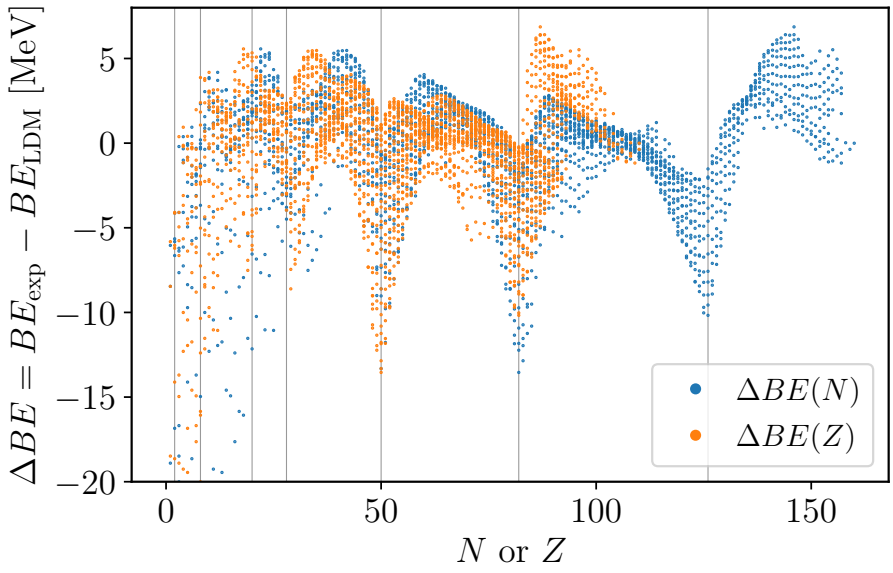

Figure 2.3: Deviation of the nuclear binding energies modeled by the semiempirical mass formula ($BE_{\rm LDM}$) from the experimentally determined binding energies ($BE_{\rm exp}$) as listed in AME2020 [10], as functions of neutron number N and proton number Z. The vertical lines correspond to the magic number $N, Z = 2, 8, 20, 28, 50, 82$, and 126.

The deviation of the experimental binding energies from the predictions by the semiempirical mass formula is shown in Figure 2.3. Large deviations are observed at $N = 28,\ 50,\ 82,\ 126$ and $Z = 28,\ 50,\ 82$. These numbers, in addition to $N, Z = 2,\ 8,\ 20$, are known as *magic numbers*, where the nuclei become exceptionally strongly bound due to the fully occupied shells, analogous to closed electron shells in atomic structures. This shows that the liquid-drop model (LDM), which describes the bulk properties of nuclei, does not capture well such microscopic effect originating from the nuclear shell structure. As discussed in more detail in the following, much of the effort in developing more realistic nuclear mass models has been put into reconciling the macroscopic description of nuclei with the microscopic effect.

Models that have microscopic corrections to macroscopic descriptions of atomic

nuclei are often referred to as microscopic-macroscopic (mic-mac) models. The first step towards adding a microscopic effect to the liquid-drop model was taken by Myers and Swiatecki (1966) [128]. In their mass model, shell effects were treated as "bunching" of single-particle levels through a simple algebraic representation. Furthermore, a shape parameterization was introduced to allow for deviations from spherical symmetry, which is assumed by the liquid-drop model. Pairing of like nucleons (*nn* or *pp* pairs) was taken into account by adding a term $11A^{-1/2}$ MeV for odd-odd nuclei (nuclei with odd N and odd Z) and subtracting the same term for even-even nuclei from the total binding energy. A Wigner term, which corrects for the systematic underbinding of nuclei around $N = Z$, was also included. These corrections improved the root-mean-squared (rms) error between experimental and calculated masses to around 1 MeV from 2.97 MeV without such corrections [121].

2.2.2 The Strutinsky Theorem

A more rigorous approach for including shell corrections to a macroscopic model was made possible by the Strutinsky theorem [129, 130], which was later generalized by Myers and Swiatecki (1982) [128]. From a microscopic perspective, this method can be understood as an approximation to the Hartree-Fock (HF) method (see Section 2.2.4), in which nucleons independently move around in a average (mean-field) potential. Myers and Swiatecki (1982) [131] had shown that, using a smooth diagonal single-particle density matrix $\tilde{\rho}$, which approximates the HF self-consistent single-particle density ρ_{HF}, the HF energy E_{HF}, which is a functional of ρ_{HF}, can be expanded in powers of $\delta\rho \equiv \rho_{\mathrm{HF}} - \tilde{\rho}$

$$E_{\mathrm{HF}} \equiv E[\rho_{\mathrm{HF}}] \simeq E[\tilde{\rho}] + \sum_i n_i \tilde{\varepsilon}_i - \mathrm{tr}\,\tilde{h}\tilde{\rho} + O(\delta\tilde{\rho}^2). \tag{2.9}$$

$\tilde{h} \equiv h[\tilde{\rho}]$ is an approximation to the exact HF Hamiltonian $h[\rho_{\mathrm{HF}}]$, $\tilde{\varepsilon}_i$ are the corresponding single-particle energies, and n_i are their occupation numbers. The term $E[\tilde{\rho}]$ can be, for example, determined from the liquid-drop model (Section 2.2.1), the droplet model (Section 2.2.3), or the energy determined from the extended Thomas-Fermi method (Section 2.2.5). The single-particle Hamiltonian $\tilde{h}$ has the usual form of $-\frac{\hbar^2}{2M}\boldsymbol{\nabla}^2 + V$, where V is the (deformed) potential of choice, which

usually contains the spin-orbit effect as well. The term $\mathrm{tr}\,\tilde{h}\tilde{\rho}$ is the smoothed version of the sum of the single-particle energies

$$\mathrm{tr}\,\tilde{h}\tilde{\rho} \equiv \widetilde{\sum_i} n_i \tilde{\varepsilon}_i \equiv \tilde{E}_{\mathrm{s.p.}}, \tag{2.10}$$

where the original sum of the single-particle energies is

$$E_{\mathrm{s.p.}} \equiv \sum_i n_i \tilde{\varepsilon}_i. \tag{2.11}$$

Strutinsky (1967, 1968) [129, 130] expressed this $E_{\mathrm{s.p.}}$ as

$$E_{\mathrm{s.p.}} = \int_{-\infty}^{\infty} \varepsilon g(\varepsilon)\,\mathrm{d}\varepsilon, \tag{2.12}$$

where

$$g(\varepsilon) = \sum_i n_i \delta(\varepsilon - \tilde{\varepsilon}_i). \tag{2.13}$$

In order to obtain $\tilde{E}_{\mathrm{s.p.}}$, the simplest approach is to replace $g(\varepsilon)$ with $\tilde{g}(\varepsilon)$, which is a sum of Gaussian,

$$\tilde{g}(\varepsilon) = \frac{1}{\gamma\sqrt{\pi}} \sum_i n_i \exp\left[-\frac{(\varepsilon - \tilde{\varepsilon}_i)^2}{\gamma^2}\right], \tag{2.14}$$

where γ is the width of the smoothing, which is set to be at least as wide as the spacing between the average spacing of the major shells. The smoothed sum of the single-particle energies is then

$$\tilde{E}_{\mathrm{s.p.}} = \int_{-\infty}^{\infty} \varepsilon \tilde{g}(\varepsilon)\,\mathrm{d}\varepsilon. \tag{2.15}$$

This is the basic concept of the Strutinsky shell correction method. The procedure is often referred to as the standard averaging method.

2.2.3 Finite Range Droplet Model (FRDM)

The finite-range droplet model (FRDM) developed by Möller et al. (2016, 1995) [119, 132], which has been one of the most successful and commonly used macroscopic-

microscopic ("mic-mac") global mass models, included not only the Strutinsky shell corrections but also pairing corrections based on the Bardeen-Cooper-Schrieffer (BCS) theory of superconductivity [133] as well as the Wigner term. As the name suggests, in the FRDM the liquid-drop model was replaced by the "droplet" model, originally developed by Myers and Swiatecki (1969, 1974) [134, 135], which is described below.

Macroscopic Part

One of the improvements made in the macroscopic droplet model was to allow a finite incompressibility of nuclei, which was simply infinite in the liquid-drop model. It allows a finite nucleus to be squeezed by the surface tension and dilated by the Coulomb force. This was achieved by introducing a dilation variable $\varepsilon = (\rho_0 - \rho^c)/3\rho_0$ and a central asymmetry variable $\delta = (\rho_n - \rho_p)/\rho^c$ to the volume (bulk) term of the liquid-drop model, where ρ_0 is the equilibrium density of infinite nuclear matter and $\rho^c = \rho_n^c + \rho_p^c$ is the sum of the central (bulk) density of neutrons and protons. The surface term was also modified so that the neutron and proton surfaces are separate, which is consistent with the observations of real nuclei (e.g. the observation of a neutron skin [136]). These improvements provided a framework for describing dynamic phenomena such as the giant dipole resonance. Furthermore, more sophisticated treatments of the Coulomb energy, such as the exchange effect, surface diffuseness, redistribution of protons, and the finite proton size, were introduced to depart from the simple picture of a uniformly charged sphere with a defined surface assumed in the liquid-drop model. Deformation was also accounted for through deformation-dependent factors.

The "finite-range" property of the model comes from the finite range of the nuclear force. This was incorporated into the model by multiplying the surface term of the liquid-drop model with a shape-dependent factor B_1:

$$B_1 = \frac{A^{-2/3}}{8\pi^2 r_0^2 a^4} \int\int \left(2 - \frac{|\boldsymbol{r} - \boldsymbol{r'}|}{a}\right) \frac{\exp(-|\boldsymbol{r} - \boldsymbol{r'}|/a)}{|\boldsymbol{r} - \boldsymbol{r'}|/a} \, \mathrm{d}^3\boldsymbol{r} \, \mathrm{d}^3\boldsymbol{r'}, \tag{2.16}$$

which is a folding of an empirical saturating two-body potential expressed by the Yukawa-plus-exponential model, whose range is a. The double integral is over a

sharp-surfaced (deformed) matter distribution whose volume is $V = (4\pi/3)r_0^3 A$. The constant in front of the integrals becomes 1 when a becomes 0. The Coulomb energy was also refined by taking into account the diffuseness of the charge distribution characterized by the diffuseness constant a_{den}.

The other major improvement to the macroscopic model was the introduction of the phenomenological exponential compressibility term, proposed by Treiner et al. [137]. This modification addressed the overestimation of the central density by the standard droplet model.

Microscopic Part

In mic-mac models, the total potential energy can generally be expressed as a function of neutron number N, proton number Z, and the shape of the nucleus [119]

$$E_{\mathrm{pot}}(N,Z,\mathrm{shape}) = E_{\mathrm{mac}}(N,Z,\mathrm{shape}) + E_{\mathrm{s+p}}(N,Z,\mathrm{shape}), \tag{2.17}$$

where E_{mac} is the contribution from the macroscopic model and $E_{\mathrm{s+p}}$ is the shell-plus-pairing correction. While microscopic correction is technically the shell-plus-paring correction added to the macroscopic deformation energy relative to the macroscopic spherical energy, in practical calculations it is $E_{\mathrm{s+p}}$ that is calculated to obtain the microscopic corrections. Given a deformation of a nucleus, $E_{\mathrm{s+p}}$ is solely determined from the single particle levels using the Strutinsky's theorem and a pairing model.

In order to calculate the shell corrections, it is necessary to first specify the single-particle potential V felt by a nucleon

$$V = V_{\mathrm{l}} + V_{\mathrm{s.o.}} + V_{\mathrm{C}}, \tag{2.18}$$

where V_{l} is the spin-independent nuclear part of the potential, $V_{\mathrm{s.o.}}$ is the spin-orbit potential, and V_C is the Coulomb potential. The first spin-independent part is the folded-Yukawa potential

$$V_{\mathrm{l}}(\boldsymbol{r}) = -\frac{V_0}{4\pi {a_{\mathrm{pot}}}^3} \int_V \frac{\exp\left(-|\boldsymbol{r}-\boldsymbol{r'}|/a_{\mathrm{pot}}\right)}{|\boldsymbol{r}-\boldsymbol{r'}|/a_{\mathrm{pot}}}\, \mathrm{d}^3\boldsymbol{r'}, \tag{2.19}$$

where $a_{\rm pot}$ is called the potential diffuseness constant, and the volume integral is over the volume of the (deformed) potential, whose volume is $\frac{4}{3}\pi R_{\rm pot}^3$. Note that $R_{\rm pot}$, which is the potential radius, is different from the range of the nuclear force a. The spin-orbit potential is

$$V_{\rm s.o.} = -\lambda \left(\frac{\hbar}{2m_{\rm nuc}c}\right)^2 \frac{\boldsymbol{\sigma}\cdot\boldsymbol{\nabla}V_1(\boldsymbol{r})\times\boldsymbol{p}}{\hbar}, \tag{2.20}$$

where λ is the spin-orbit interaction strength, $m_{\rm nuc}$ is the nucleon mass, $\boldsymbol{\sigma}$ is the Pauli spin matrices, and $\boldsymbol{p}$ is the nucleon momentum. The third Coulomb potential is

$$V_{\rm C}(\boldsymbol{r}) = \frac{Ze^2}{(4\pi/3){r_0}^3 A}\int \frac{{\rm d}\boldsymbol{r'}}{|\boldsymbol{r}-\boldsymbol{r'}|}, \tag{2.21}$$

where the integral is over a (deformed) sharp-surfaced region, whose volume is $(4\pi/3){r_0}^3 A$ with r_0 being the charge-radius constant $r_0 = (4\pi\rho_0/3)^{-1/3}$.

From the potential V, a single-particle Schrödinger equation is solved to obtain single-particle energies e_i, which are then used to obtain the shell corrections using the standard averaging method based on the Strutinsky theorem. To solve for the single-particle energies, the matrix elements of the Hamiltonian are generated from a set of deformed, axially symmetric, harmonic-oscillator basis functions.

As for the pairing correction, the FRDM adopts the Lipkin-Nogami pairing model [138–140], which is a variation of the Bardeen-Cooper-Schrieffer (BCS) theory. The Lipkin-Nogami approximation overcomes the limitation of the BCS model, which is the large spacing of single-particle levels at the Fermi surface, by taking into account effects associated with particle-number fluctuations. The pairing strengths G for neutrons and protons are determined by postulating an effective-interaction pairing gap Δ_G:

$$\Delta_{G_n} = \frac{r_{\rm mic}B_{\rm S}}{N^{1/3}} \quad \text{for neutrons,} \tag{2.22}$$

$$\Delta_{G_p} = \frac{r_{\rm mic}B_{\rm S}}{Z^{1/3}} \quad \text{for protons,} \tag{2.23}$$

where B_S is one of the deformation-dependent factors and $r_{\rm mic}$ is the pairing parameter determined from a fit. In this picture, a constant level density in the vicinity of the Fermi surface, leading to a smooth level density which is obtained in the

Strutinsky method. This allows the sums in the gap equation to be replaced by an integral that can be evaluated analytically. Note that the pairing treated in the microscopic part of the FRDM only considers *nn* and *pp* pairing—*np* pairing is not considered.

In total, the most recent model FRDM2012 has 17 parameters which are determined from a fit to the mass data, and 21 parameters which are determined from other considerations. Improvements from the older version FRDM1992 include improvements of the parameter optimization method, new experimental mass data, improved energy minimization method, inclusion of axial symmetry, adjustment of additional parameters, and improvements of the ground state correlation energies. The FRDM2012 achieves an rms error of 0.602 MeV for nuclei with mass numbers $A \geq 20$ relative to the known masses in the AME2020 [10].

2.2.4 Hartree-Fock-Bogoliubov (HFB) Mass Models

The Hartree-Fock-Bogoliubov (HFB) mass models take a microscopic approach originally developed by Samyn et al. (2002) [141] and Goriely et al. 2002 [142], which achieved a performance comparable to FRDM in reproducing experimentally determined nuclear masses [143]. A high-level review of the Hartree-Fock method as well as its extension called the Hartree-Fock-Bogoliubov method is given in the following. The key design aspects of the HFB mass models will also be discussed.

The Hartree-Fock Method

A fully microscopic approach for modeling nuclear masses or binding energies is to start with a realistic nucleon-nucleon interaction and solving the many-body Schrödinger equation. Such approach is called the *ab initio* method. However, it is not yet possible to predict the properties of atomic nuclei across the whole chart of nuclides.

One of the more computationally tractable and scalable approaches to microscopically calculate nuclear masses is to assume that the nucleons in a nucleus move independently in an average (mean-field) potential generated by the other nucleons. Such a theoretical framework is provided by the Hartree-Fock (HF)

method. In the HF theory, the average single-particle potential is called the Hartree-Fock potential

$$H^{\mathrm{HF}} = \sum_{i=1}^{A} h(i), \tag{2.24}$$

whose ground state energy E_0^{HF} is an approximation to the exact ground state of the many-body system. The corresponding eigenfunction $\Phi(1,\ldots A)$ of the Hamiltonian is anti-symmetrized product of single-particle functions (Slater determinant)

$$|\mathrm{HF}\rangle = |\Phi(1\ldots A)\rangle = \prod_{i=1}^{A} a_i^{\dagger}\,|-\rangle\,, \tag{2.25}$$

where $a_k^{\dagger}$ and a_k are Fermion creation and annihilation operators corresponding to the single-particle wave functions φ_k, respectively, and $|-\rangle$ is the bare vacuum. The single-particle wave functions φ_k themselves are also eigenfunctions of the single-particle Hamiltonian h, and the single-particle Schrödinger equation is

$$\left(-\frac{\hbar^2}{2M}\boldsymbol{\nabla}^2 + U\right)\varphi_k = \varepsilon_k \varphi_k, \tag{2.26}$$

where U is the single-particle potential determined from the effective nuclear force of choice. The set of equations can be considered as the HF equations in the coordinate space, while it is common to work in a configuration space, which are characterized by the occupied and empty levels in the state $|\mathrm{HF}\rangle$. The set of Slater determinants $\{\Phi\}$ consisting of the A single-particle basis φ_k $(k = 1,2,\ldots,A)$ is used as a trial wave function for the variational method to minimizing the HF-energy

$$E^{\mathrm{HF}} = \langle\Phi|H|\Phi\rangle \equiv \int \mathrm{d}^3\boldsymbol{r}\;\mathcal{E}(\boldsymbol{r}), \tag{2.27}$$

where H is the many-body Hamiltonian and $\mathcal{E}(\boldsymbol{r})$ is called the energy density functional. Thus, the HF-wave function $|\mathrm{HF}\rangle$ is obtained by minimizing E^{HF}. It is important to note that the HF method is an approximation to the exact many-body system, therefore, the wave functions and corresponding energies are usually not identical to the exact ones.

The Hartree-Fock-Bogoliubov Method

As mentioned in the overview of the Hartree-Fock method, in general, wave functions obtained through a configuration mixing of Slater determinants are not identical to the exact nuclear wave functions. The deviations of the mean-field picture from the actual nuclear many-body systems are often referred to as *correlations*. One of the most prominent correlations is pairing of like nucleons (neutron-neutron and proton-proton), as observed in the odd-even staggering of nuclear binding energies (e.g. the pairing term in the semiempirical mass formula Eq. 2.6). One of the approaches to incorporate the pairing effect is to model the particle-particle correlations using the BCS theory, which was originally developed to describe superconductivity by introducing a concept called *quasi-particles*, which is appropriate for describing the pairing of fermions. An attempt has been made to create a global mass model using the so-called HF-BCS procedure [144]. In this model, quasi-particles and the pairing potential were introduced in a generalized single-particle picture described by the HF theory. However, this treatment of pairing is known to become unphysical for neutron-rich nuclei, which is a significant problem, especially in the modeling of the *r*-process nucleosynthesis.

The Hartree-Fock-Bogoliubov (HFB) method generalizes and unifies the HF method and the BCS model. The single-particle and pairing aspects are treated simultaneously by determining wave functions consisting of freely moving quasi-particles through the variational principle.

The first of the series of the HFB mass models was published in 2002 by Samyn et al. (2002) [141], which was named HFB-1, shortly followed by HFB-2 [142]. Among many, one of the common features of all the HFB mass models is the use of the Skyrme force. The ten-parameter form of the Skyrme interactions is a widely used zero-range phenomenological effective force between nucleons labeled with

i and j:

$$\begin{aligned} v_{ij} &= t_0(1+x_0P_\sigma)\delta(\boldsymbol{r}_{ij}) \\ &+ t_1(1+x_1P_\sigma)\frac{1}{2\hbar^2}\{\boldsymbol{p}_{ij}{}^2\delta(\boldsymbol{r}_{ij})+\delta(\boldsymbol{r}_{ij})\boldsymbol{p}_{ij}{}^2\} \\ &+ t_2(1+x_2P_\sigma)\frac{1}{2\hbar^2}\boldsymbol{p}_{ij}{}^2\cdot\delta(\boldsymbol{r}_{ij})\boldsymbol{p}_{ij}{}^2 \\ &+ \frac{1}{6}t_3(1+x_3P_\sigma)\rho^\gamma\delta(\boldsymbol{r}_{ij}) \\ &+ \frac{i}{\hbar^2}W_0(\boldsymbol{\sigma}_i+\boldsymbol{\sigma}_j)\cdot\boldsymbol{p}_{ij}\times\delta(\boldsymbol{r}_{ij})\boldsymbol{p}_{ij}, \end{aligned} \tag{2.28}$$

where $\boldsymbol{r}_{ij}=\boldsymbol{r}_i-\boldsymbol{r}_j$, $\boldsymbol{p}_{ij}=-i\hbar(\boldsymbol{\nabla}_i-\boldsymbol{\nabla}_j)$ is the relative momentum, $P_\sigma=\frac{1}{2}(1+\boldsymbol{\sigma}_1\cdot\boldsymbol{\sigma}_2)$ is the two-body spin-exchange operator, and $\rho=\rho_n+\rho_p$ is the local nucleonic density with ρ_n and ρ_p being the local neutron and proton density, respectively. The first term with t_0 describes a pure zero-range δ-force with a spin-exchange. The t_1 and t_2 terms simulate a finite effective range and the term with t_3 is a density dependent force. The last term is a two-body spin-orbit term.

In the recent developments of the HFB mass models, additional terms with t_4 and t_5 were introduced, which are density-dependent generalizations of the t_1 and t_2 terms, adding up the total number of parameters to 16. Furthermore, an additional spin-orbit degree of freedom was added at the level of the energy-density functional, which is the expectation value of an effective Hamiltonian on a quasiparticle vacuum. In the study of mass model averaging described in Chapter 4, we have used the HFB-31 mass model, which is the most recent development. In this model, the pairing force of like nucleons were modeled to fit the pairing gaps $\Delta_q(\rho_n,\rho_p)$, where q denotes neutron or proton ($q=n$ or p), to the calculations of pure neutron matter and charge-symmetric (equal numbers of neutrons and protons) nuclear matter based on realistic two- and three-body nuclear forces. This allows for a more consistent description from nuclei to neutron stars, which is one of the most neutron-rich systems. However, this treatment necessitates an inclusion of a phenomenological surface term, which depends on the local density gradients, in the pairing force to maintain a good fit to the experimentally measured nuclear masses. In addition to the pairing effect, corrections in the form of the Wigner terms and the spurious collective energy due to the rotation associated with the vi-

olation of angular momentum conservation and the deformation dependence of the vibration have been included to the model.

The parameters of the Skyrme force, the pairing effect, the Wigner terms, and the collective energy corrections were fitted to the 2353 measured masses of nuclei with N and $Z \geq 8$ listed in the Atomic Mass Evaluation (AME) 2012 [127]. The HFB-31 model resulted in an rms error of 0.579 MeV for nuclei with mass numbers $A \geq 20$ with respect to the AME2020 [10].

2.2.5 Extended Thomas-Fermi Plus Strutinsky Integral (ETFSI) Mass Models

One of the problems of macroscopic-microscopic mass models such as the FRDM is the inconsistency between the macroscopic and microscopic parts. In the FRDM, the parameter values of the microscopic shell corrections are known to differ from the macroscopic counterparts [145]. However, the problem associated with the microscopic HF methods (HFB and HF-BCS) when they were first developed was the prohibitive computational cost, especially for deformed nuclei. Therefore, the use of a semiclassical approximation to the HF method called the Extended Thomas-Fermi (ETF) approximation[1] was proposed to reduce the computational cost. The point of using the ETF method is to obtain the smooth macroscopic part of the mass model using a Skyrme force; then the same force can be used to calculate the shell corrections through the Strutinsky method (Section 2.2.2). This method is called the Extended Thomas-Fermi plus Strutinsky integral (ETFSI). Using the Skyrme force (Eq. 2.28) with appropriate constraints, the exact HF energy E_{HF} can be written as [146]

$$\begin{aligned} E_{\mathrm{HF}} &\equiv E[\rho_{\mathrm{HF}}] \\ &= \int \mathcal{E}(\tau_q(\boldsymbol{r}),\, \boldsymbol{J}_q(\boldsymbol{r}),\, \rho_q(\boldsymbol{r}),\, \rho'_q(\boldsymbol{r}),\, \ldots)\mathrm{d}^3\boldsymbol{r}, \end{aligned} \tag{2.29}$$

where ρ_{HF} is the HF density matrix, τ_q and $\boldsymbol{J}_q$ ($q = n$ or p) are the kinetic energy density and the spin-current density, respectively, $\rho_q(\boldsymbol{r}) = \sum_i^A \phi^*_{i,q}(\boldsymbol{r})\phi_{i,q}(\boldsymbol{r})$ is the

[1] The theoretical formalism of the extended Thomas-Fermi approximation is quite lengthy and the detailed discussion of this method is outside the scope of this thesis, therefore, interested readers are referred to e.g., Ref [95].

diagonal part of the single-particle density matrix, and $\rho'_q(\boldsymbol{r})$ is its gradient. τ_q and $\boldsymbol{J}_q$ are not only dependent on $\rho_q(\boldsymbol{r})$, but also on the off-diagonal elements of the density matrix $\rho_q(\boldsymbol{r},\boldsymbol{r}')$. According to Ref. [146], the essence of the ETF method is to approximate τ_q and $\boldsymbol{J}_q$ by $\tilde{\tau}_q$ and $\tilde{\boldsymbol{J}}_q$, respectively, which depend only on the diagonal elements of the density matrix, i.e., $\rho_q(\boldsymbol{r})$, so that

$$\begin{aligned} E[\rho_{\mathrm{HF}}] &\simeq E_{\mathrm{ETF}}[\rho_{\mathrm{ETF}}] \\ &\equiv \int \mathcal{E}_{\mathrm{ETF}}(\rho_q(\boldsymbol{r}),\, \rho'_q(\boldsymbol{r}),\, \ldots)\, \mathrm{d}^3\boldsymbol{r}. \end{aligned} \tag{2.30}$$

Eliminating the off-diagonal elements significantly speeds up the calculation compared to the full HF method, although not as fast as standard mic-mac models [147]. Now using the Strutinsky method (Sec. 2.2.2), the HF energy $E_{\mathrm{HF}} \equiv E[\rho_{\mathrm{HF}}]$ can be approximated as

$$E_{\mathrm{HF}} \simeq E_{\mathrm{ETF}} + \sum_i n_i \tilde{\varepsilon}_i - \mathrm{tr}\,\tilde{h}\rho_{\mathrm{ETF}} + O(\delta\rho_{\mathrm{ETF}}{}^2), \tag{2.31}$$

where the shell corrections can be obtained using the same Skyrme force used for calculating E_{ETF}. Since we have access to ρ_{ETF}, it is not necessary to perform averaging of the single-particle energies. While the ETFSI model is mostly redundant since full HF (HFB) calculations are now possible, it is still valuable in calculating fission barriers. The last version of the ETFSI mass model called ETFSI-2 [148] resulted in an rms deviation of 1.085 MeV for nuclei with mass numbers $A \geq 20$ with respect to the AME2020 [10].

2.2.6 Weizsäcker-Skyrme (WS) Mass Models

Another approach to improve the consistency between the macroscopic part and the microscopic part in mic-mac mass models has been proposed by Wang et al. [145, 149–152]. Similarly to Eq. 2.17, the total energy of the model E is the sum of the macroscopic part and the Strutinsky shell correction ΔE

$$E(A,Z,\beta) = E_{\mathrm{LD}}(A,Z)\prod_{k\geq 2}(1+b_k\beta_k^2) + \Delta E(A,Z,\beta), \tag{2.32}$$

where β_k are the deformation parameters for quadrupole ($k=2$), octupole ($k=3$) deformation and so on, and b_k are the corresponding adjustable parameters to take into account the effect of deformation in the macroscopic energy. $E_{\rm LD}$ is a variation of the semiempirical mass formula (Eq. 2.6)

$$E_{\rm LD}(A,Z) = a_V A + a_S A^{2/3} + a_C \frac{Z(Z-1)}{A^{1/3}}(1-Z^{-2/3}) + a_I I^2 A + a_{\rm pair} A^{-1/3}\delta_{np}, \tag{2.33}$$

where

$$\delta_{np} = \begin{cases} 2-|I| : N \text{ and } Z \text{ even }, \\ \quad |I| : N \text{ and } Z \text{ odd }, \\ 1-|I| : N \text{ even }, Z \text{ odd }, \text{ and } N > Z, \\ 1-|I| : N \text{ odd }, Z \text{ even }, \text{ and } N < Z, \\ \quad 1 : N \text{ even }, Z \text{ odd }, \text{ and } N < Z, \\ \quad 1 : N \text{ odd }, Z \text{ even }, \text{ and } N > Z, \end{cases} \tag{2.34}$$

and

$$a_I = c_{\rm sym}\left[1 - \frac{\kappa}{A^{1/3}} + \frac{2-|I|}{2+|I|A}\right], \tag{2.35}$$

with $c_{\rm sym}$ and κ being parameters determined from a fit. The term which involves I approximately works as the Wigner term.

Their approach to maintain the consistency between the macroscopic part and the microscopic corrections is to use the Skyrme force through the ETF approximation to determine or verify some of the parameters, such as b_k and $a_{\rm sym}$, then use the same force to calculate the shell correction by the Strutinsky method. Since the model consists of the semiempirical (Weizsäcker) mass formula and the shell correction based on the Skyrme force, it is often referred to as the Weizsäcker-Skyrme (WS) model.

The latest version WS4 includes further corrections such as constraints on mirror nuclei, residual pairing effect, triaxial deformation, and surface diffuseness. The mass model achieved an rms error of 0.293 MeV for nuclei with mass numbers $A \geq 20$, relative to the AME2020.

2.2.7 Duflo-Zuker (DZ) Mass Model

The mass model developed by Duflo and Zuker (1995) [153] (DZ) is another mass model often used in studies of the *r*-process nucleosynthesis. In this section, an overview of the basic concept of the model is provided. While this model is more fundamental than the mic-mac models, it is not fully microscopic since it is not explicitly built upon nucleon-nucleon interactions. The starting point of the construction of the model is the assumption that a two-body "pseudopotential" is smooth enough to perform HF calculations. Based on this assumption, the corresponding Hamiltonian H can be separated into the monopole part H_m and the multipole part H_M:

$$H = H_m + H_M. \tag{2.36}$$

The monopole part H_m is treated phenomenologically to reproduce the saturation property of the nuclear force and able to reproduce the exact energy of closed shells, as well as their single particle or hole states. The multipole part H_M can be derived in a parameter-free way from the realistic nucleon-nucleon interactions and contains residual interactions, which describe pairing, quadrupole correlations, Wigner correlations and so on.

There exist different versions of the DZ mass models with 10, 28, and 31 independent parameters. While the 10- and 28-parameter versions (referred to as DZ10 and DZ28, respectively) are described in their paper [153] and the mass tables are widely available, for the 31-parameter version (DZ31) only the code is distributed [154]. The performance based on the AME2012 is essentially comparable ($\sigma_{\rm rms}(\mathrm{DZ28}) = 0.360$ MeV and $\sigma_{\rm rms}(\mathrm{DZ31}) = 0.362$ MeV) [151], therefore, in the study described in Chapter 4, we employ the more accessible DZ28 version. The rms error of DZ28 for nuclei with mass numbers $A \geq 20$ with respect to the AME2020 is 0.427 MeV.

2.2.8 Models by Koura, Uno, Tachibana, and Yamada (KUTY)

A similar approach to standard mic-mac models was proposed by Koura et al. [155, 156]. The total mass predicted by the model $M(Z,N)$ is expressed as

$$M(Z,N) = M_{\rm g}(Z,N) + M_{\rm S}(Z,N) + M_{\rm eo}(Z,N), \tag{2.37}$$

where $M_{\mathrm{g}}(Z,N)$ is called the gross term, which captures the general trend of the masses, M_{S} is called the shell term, which accounts for the deviations from the general trend predicted by the gross term, and M_{eo} is called the even-odd term, which corrects for the even-odd staggering in masses that are not captured by the shell term. The gross term is similar to the semiempirical mass formula, but the physical meaning of each term is slightly different:

$$\begin{aligned} M_{\mathrm{g}}(Z,N)c^2 =& M_{\mathrm{H}}c^2 Z + M_n c^2 N + a(A)A + b(A)|N-Z| \\ &+ c(A)(N-Z)^2/A + E_C(Z,N) - k_{\mathrm{el}} Z^{2.39}, \end{aligned} \tag{2.38}$$

where M_H and M_n are the mass excess of a hydrogen atom and a neutron, respectively. E_C is the Coulomb term and k_{el} is the binding energy of the electrons. $a(A)$, $b(A)$, and $c(A)$ are further parametrized by a_i, b_i, c_i ($i = 1,2,3,4$) and α_j ($j = a,b,c$), which are determined from a fit.

The starting point of the shell effect term is the construction of a spherical single-particle potential for neutrons and protons. The potential consists of the spin independent component, which is a modified Woods-Saxon potential and the spin-orbit component. From this single-particle energies are obtained, from which crude shell energies are obtained. The crude shell energies are refined by pairing corrections obtained by assuming the BCS-type pairing. The effect of deformation is modeled by a superposition of spherical nuclei, which is computationally less expensive than modeling the deformation using deformed potentials.

The even-odd term is obtained from experimental masses and the gross + shell parts of the mass model, which corrects for the deviations that could not be accounted for by the treatment of the shell energies.

The rms error of the latest version KUTY05 for nuclei with mass numbers $A > 20$ is 1.109 MeV relative to the AME2020.

2.2.9 Brief Comparison of Mass Models

The performances (rms errors σ_{rms}) of the nuclear mass models discussed so far with respect to the experimentally determined nuclear masses (from the AME2020 [10]) are summarized in Table 2.1. The rms errors are calculated for nuclei with mass numbers $A \geq 20$, since some of the mass models do not provide predictions below

$A = 20$.

Mass Model	$\sigma_{\mathrm{rms}}(\mathrm{AME2020})$ [MeV]
FRDM2012 [119]	0.602
DZ28 [153]	0.427
HFB31 [143]	0.579
ETFSI-2 [148]	1.085
WS4 [152]	0.293
KUTY05 [156]	1.109

Table 2.1: A summary of rms errors of the mass models discussed in Section 2.2, with respect to the experimentally determined masses listed in the AME2020 [10]. The rms errors are calculated for nuclei with mass numbers $A \geq 20$.

Figure 2.4 shows the residuals of the theoretical mass models as functions of neutron number, with respect to the experimental nuclear masses from the AME2020. For most of the mass models, the discrepancies of the predictions from the experimental masses become large for small neutron number. This is largely due to the mean-field assumptions of the mass models, which become less valid for lighter masses.

Figure 2.5 shows comparisons of the mass models described in the previous sections for nickel (Ni, $Z = 28$), tin (Sn, $Z = 50$), and gadolinium (Gd, $Z = 64$) isotopes, as well as the experimentally determined masses listed in the AME2020 [10], relative to the FRDM2012 predictions. It can be seen that the predictions of nuclear masses by different models are in close agreement where experimental data exist since they have been constrained in this area. However, they start to diverge as the predictions are extrapolated towards neutron-rich regions, and the difference between the models can be as large as 15-20 MeV, which will result in large uncertainties in the calculations of *r*-process observables (e.g. abundance patterns and kilonova lightcurve). In Chapter 4, a method to incorporate the variations in the mass predictions by different models and to quantify the overall uncertainty will be explored.

The effect of employing different mass models on the predictions of the abundance patterns of the *r* process is shown in Figure 2.6. In these plots, in addition

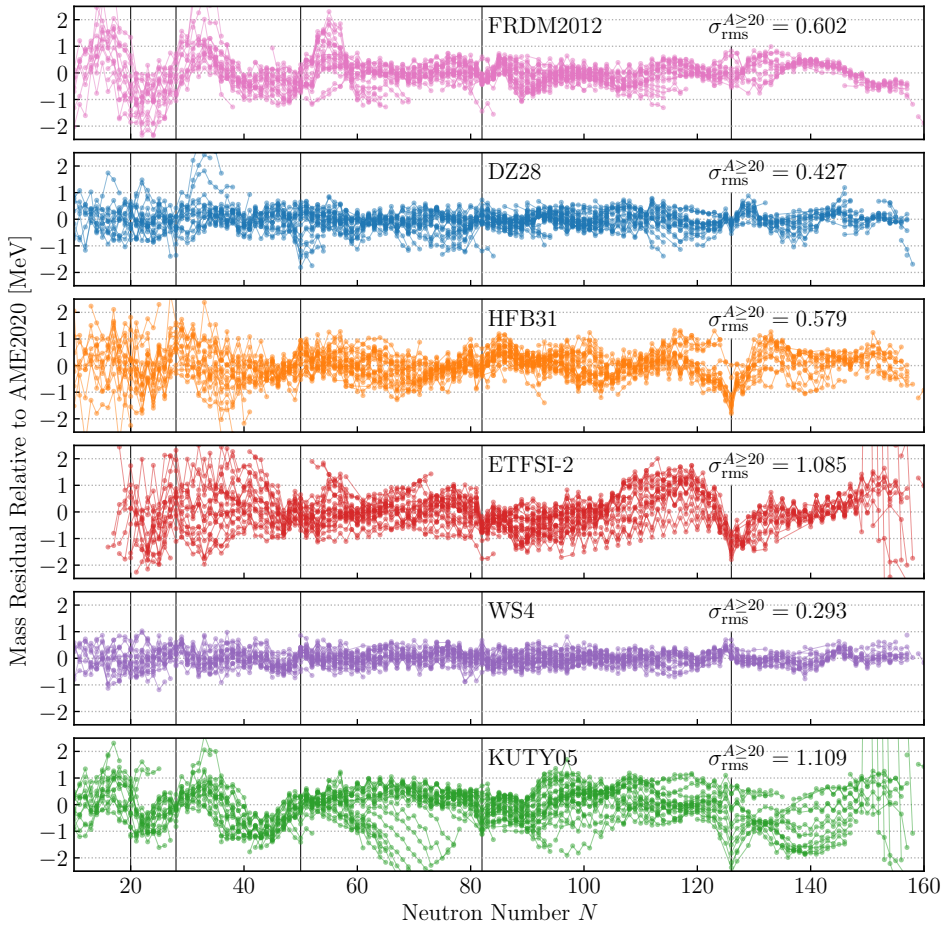

Figure 2.4: Residuals of mass excess of the theoretical mass models listed in Table 2.1 as functions of neutron number N, with respect to the experimental nuclear masses from the AME2020 [10]. The vertical lines correspond to the neutron magic numbers $N = 20, 28, 50, 82$, and 126, respectively.

to the explicit dependence of the photodissociation rates on the neutron separation energies (S_n) through the detailed balance (Eq. 2.2), the dependence of the forward rates, i.e., the neutron capture rates on the S_n values are considered for consistency. The astrophysical trajectories are neutron star merger (panel (a)) and hot neutrino-driven wind (panel (b)), same as the ones used in Chapters 5 and 6. Note that

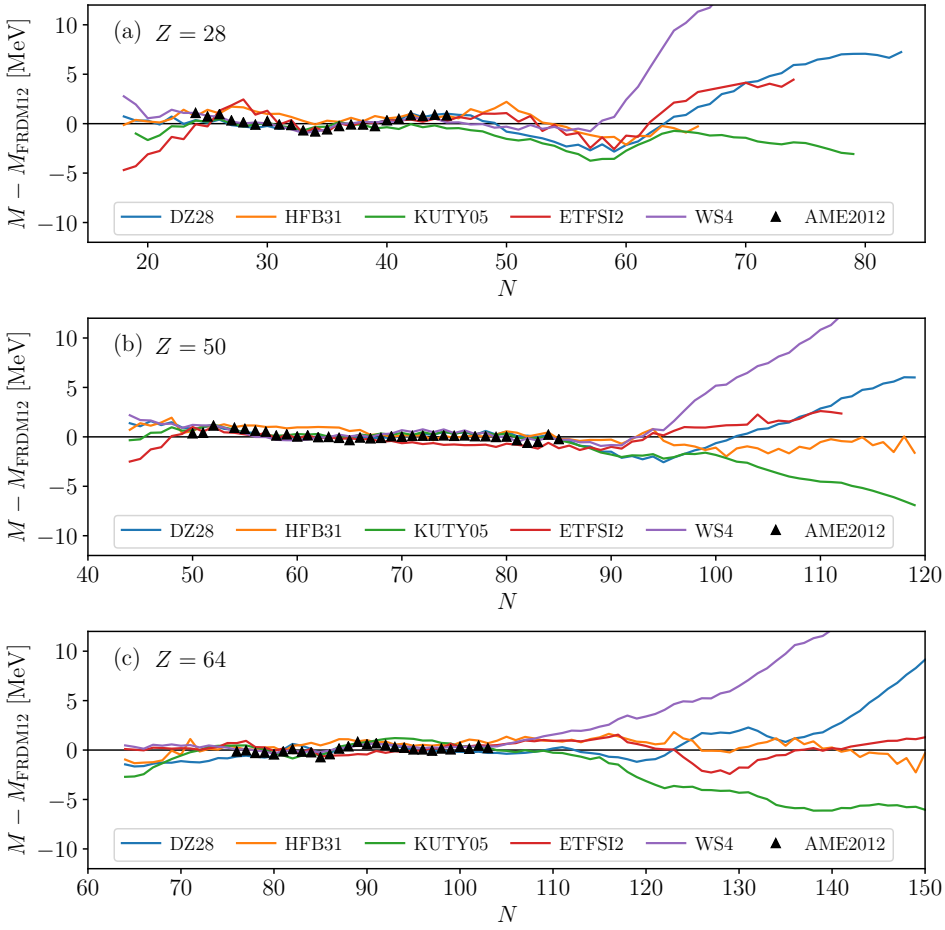

Figure 2.5: Comparisons of the mass models and the experimental masses listed in the AME2020 [10], relative to the predictions of the FRDM2012 for (a) $Z = 28$ (Ni), (b) $Z = 50$ (Sn), and (c) $Z = 64$ (Gd) isotopes.

instead of the DZ28 and ETFSI-2 models listed in Table 2.1, the DZ31 [154] and ETFSI [146] are used due to the availability of data. Data were provided by M. R. Mumpower (LANL, private communication). The plots show that the choice of mass models has a significant impact on the theoretical predictions of *r*-process abundance patterns. In reality, virtually all the reaction, decay, and fission rates, as well as fission fragment distributions, are affected by the choice of mass models.

Therefore, the impact of nuclear mass models is expected to be more significant than what is shown in Figure 2.6.

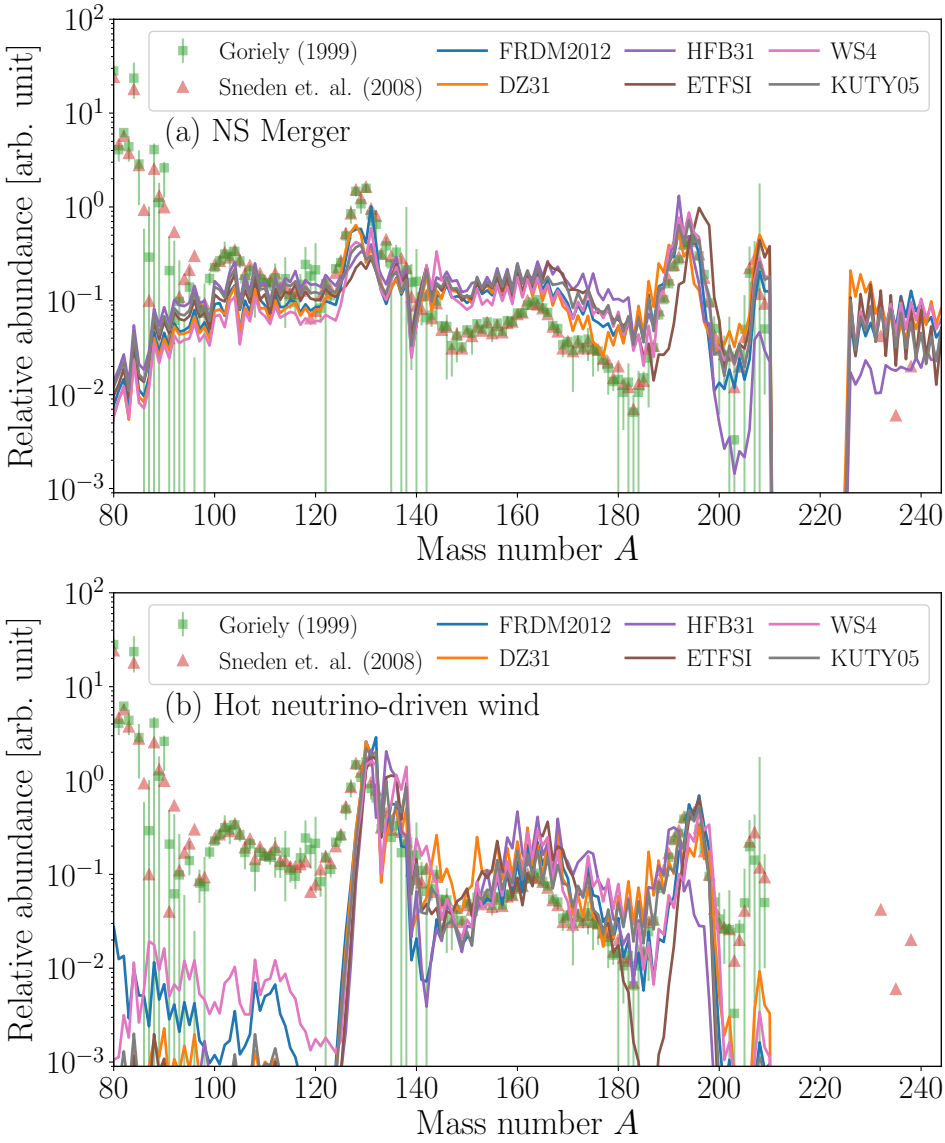

Figure 2.6: Comparisons of the predictions of the *r*-process abundance patterns employing different mass models. The top panel (a) shows the case of neutron star merger scenario, and the bottom panel (b) shows the case of hot neutrino-driven wind scenario. The astrophysical trajectories are the same as the ones used in Chapters 5 and 6. Note that instead of the DZ28 and ETFSI-2 models listed in Table 2.1, the DZ31 [154] and ETFSI [146] models are used due to the data availability. Data were provided by M. R. Mumpower (LANL, private communication).

Chapter 3

Statistical Inference and Machine Learning Methods

The method of science can be considered as a loop of *inference*, in which mathematical theories and hypotheses are constructed to explain observations, and new predictions by the theories and hypotheses are tested by further observations. Statistical inference, which is based on the language of probability, is a method of choice for testing such hypotheses and estimating unknown parameters in the mathematical theories from observed data.

In recent years, in many fields of physics and astronomy including low energy nuclear physics, estimating uncertainties associated with theoretical models has been a topic of investigation (see Refs. [157, 158] and references therein). Especially Bayesian statistics (Section 3.1) is gaining popularity since it provides a suitable framework for quantifying uncertainties in terms of probability statements. In Bayesian statistics, parameter estimations are often performed using the Markov chain Monte Carlo (MCMC) method. The basics of the method are described in Section 3.2. The Bayesian framework illustrated in these sections is applied to the uncertainty quantification of nuclear mass models in Chapter 4.

Monte Carlo methods can also be applied to sensitivity analyses, whose purpose is to identify influential inputs that contribute the most to the output uncertainty of a numerical model. In Section 3.3, the variance-based sensitivity analysis method is introduced, which infers the "sensitivity" indices based on Monte Carlo

estimators. This method is used in Chapter 5 to identify the β-decay properties of neutron-rich nuclei in the rare-earth peak region (see Section 2.1.2) which are the most responsible for the propagated uncertainty of the output of nuclear reaction network calculations (Section 1.3), within the newly obtained experimental results.

Section 3.4 discusses the basics of artificial neural networks (ANNs), which form the basis of the method explained in Chapter 6. ANNs are highly flexible machine learning models, which can be trained to learn, for example, the relations between the inputs and outputs of numerical simulations, e.g. nuclear reaction network calculations, thereby essentially *emulating* the simulations. In Chapter 6, *emulators* are constructed for nuclear reaction network calculations. This significantly speeds up the calculations and will help reduce the computational cost of statistical tasks such as variance-based sensitivity analyses.

3.1 Bayesian Statistics

It is shown that if a set of rational "beliefs" can be numerically represented, based on a simple set of axioms, manipulations of the degrees of beliefs follow the sum and product rules of probability [159–164]

$$\begin{aligned} p(x) &= \int p(x,y)\mathrm{d}y \ : \quad \text{sum rule,} \\ p(x,y) &= p(y \mid x)p(x) \ : \quad \text{product rule,} \end{aligned} \tag{3.1}$$

where $p(x)$ and $p(y)$ are the probability density functions (PDFs) of x and y, respectively, $p(x,y)$ is the joint PDF, $p(y \mid x)$ is the PDF of y conditional on x.

Let us assume that θ is a (set of) parameters that describe the characteristics of the population from which θ is obtained. If $p(\theta)$ describes our prior belief about the best value of θ before obtaining any observation that could provide information on θ, this $p(\theta)$ is called a *prior distribution*. When data $\mathcal{D}$ are obtained, for each θ, if $p(\mathcal{D} \mid \theta)$ describes the degree of our belief about $\mathcal{D}$ being the expected observation given that θ is the true value. This $p(\mathcal{D} \mid \theta)$ is called a sampling model or a *likelihood function*. From the sum and product rules (Eq.3.1), *Bayes' theorem* (*Bayes' rule*) can be derived, which provides an optimal method to update our

belief of θ given the new observation (data) $\mathcal{D}$ [163–165]

$$p(\theta \mid \mathcal{D}) = \frac{p(\theta, \mathcal{D})}{p(\mathcal{D})} = \frac{p(\mathcal{D} \mid \theta) p(\theta)}{\int p(\mathcal{D} \mid \tilde{\theta}) p(\tilde{\theta}) \, \mathrm{d}\tilde{\theta}}. \tag{3.2}$$

The probability distribution $p(\theta \mid \mathcal{D})$ obtained as a result of Bayes' theorem is called a *posterior distribution*. The Likelihood function and the prior distribution together constitute a probability model. The core of Bayesian computation is to develop the model $p(\theta, \mathcal{D}) = p(\mathcal{D} \mid \theta) p(\theta)$ and perform the computation to summarize $p(\theta \mid \mathcal{D})$ [166].

It is often challenging to mathematically formulate our prior beliefs to specify the prior distribution $p(\theta)$. The popular approach to overcome this challenge is the use of weakly informative priors. This means that with a reasonably large amount of data, likelihood dominates and the prior distribution has little effect on the outcome. This can be achieved, for example, by embedding the information on the scale of the parameters or the predictions of the probabilistic model [163, 167–169]. Note that unbounded flat priors (unbounded uniform distributions) are usually not recommended, partly because the integral of an unbounded uniform distribution gives infinity (called an improper prior), and the integral of likelihood functions does not necessarily equal one, therefore, the posterior would not have properties of a PDF [164, 167, 170].

Posterior distributions cannot usually be analytically obtained unless special types of priors are used (e.g. conjugate priors) [166]. Therefore, posteriors are numerically estimated by constructing an empirical distribution of the posterior, since often it is still possible to evaluate priors and likelihood at each point. The most commonly used method is Markov chain Monte Carlo (MCMC), which will be described in the following section.

Typically, a Bayesian posterior distribution is summarized by a (credible) interval that contains a certain fraction of the distribution, e.g., 95 %. This can be interpreted as the probability that the interval contains the unknown quantity of interest based on our prior belief and observations. This is a different concept from a frequentist (confidence) interval in a sense that the interval obtained with, for example, 95 % confidence indicates that if the same observation is repeated many times, 95 % of the constructed intervals would contain the true value of the quantity

of interest [166].

Furthermore, interpretation of the likelihood function $p(\mathcal{D} \mid \theta)$ also differs between Bayesian and frequentist paradigms. In Bayesian statistics, the observed data $\mathcal{D}$ is fixed and the uncertainty in the parameter θ is expressed as a distribution of θ. On the other hand, from a frequentist's point of view, the parameter θ is considered to be fixed, and its error bars are estimated by considering the distribution of possible data sets $\mathcal{D}$.

In Chapter 4, a concrete example of the Bayesian probabilistic modeling will be presented.

3.2 Monte Carlo Method and Markov Chain Monte Carlo

When the distribution of the quantity of interest cannot be analytically obtained, it is common to simulate a sequence random variables X^1, X^2, ... and compute the corresponding quantity of interest $g(X^i)$ ($i = 1, 2, , \ldots$), then compute the statistical quantities of interest, e.g., mean, variance, and so on.

Suppose that we can simulate independently and identically distributed random variables $X^1, X^2, \ldots, X^n$ and they have the same distribution as X, which is denoted as $f(X)$. If g is some function where $g(X)$ cannot be analytically obtained but we wish to estimate the expectation

$$\mu = \mathbb{E}[g(X)] = \int g(X) f(X) \, \mathrm{d}X, \tag{3.3}$$

then the *Monte Carlo* estimate of μ is

$$\hat{\mu}_n = \frac{1}{n} \sum_{i=1}^{n} g(X^i). \tag{3.4}$$

Similarly, the variance of $g(X)$, σ^2, can be estimated by

$$\hat{\sigma^2}_n = \frac{1}{n} \sum_{i=1}^{n} (g(X^i) - \hat{\mu}_n)^2. \tag{3.5}$$

This is the basic concept of (ordinary) *Monte Carlo*.

Markov Chain

As discussed in the previous Section 3.1, Markov chain Monte Carlo (MCMC) is often the method of choice to compute analytically intractable posterior distributions in Bayesian statistics. *Markov chain* is a sequence of random variables $X^1, X^2, \ldots$, where the conditional distribution of X^{d+1} given all the previous points x^i ($i = 1, 2, \ldots, d$) depends only on the last point x^d. The lower case means that they are realizations (observed values) of the variables X^i ($i = 1, 2, \ldots, d$). That is,

$$p(X^{d+1} \mid x^d, x^{d-1}, \ldots, x^1) = p(X^{d+1} \mid x^d). \tag{3.6}$$

The Metropolis Algorithm

Below, we will review the basic concept of MCMC by taking the random-walk Metropolis (Metropolis-Hastings) algorithm as an example. The notation follows that of Ref. [166]. Similarly to Section 3.1, let θ denote the parameter(s) of interest, and $\mathcal{D}$ be the observed data. The procedures of the algorithm are the following [166]:

1. Choose a starting point θ^0 where the posterior PDF $p(\theta^0 \mid \mathcal{D})$ is positive.

2. For $d = 1, 2, \ldots$, repeat:

   (a) Sample a proposal θ^* from a proposal distribution $J_d(\theta^* \mid \theta^{d-1})$. For the random-walk Metropolis algorithm, this proposal distribution is chosen to be symmetric, i.e., $J_d(\theta^a \mid \theta^b) = J_d(\theta^b \mid \theta^a)$ for any a, b, and d.

   (b) Compute the ratio of the density (acceptance ratio):

   $$r = \frac{p(\theta^* \mid \mathcal{D})/J_d(\theta^* \mid \theta^{d-1})}{p(\theta^{d-1} \mid \mathcal{D})/J_d(\theta^{d-1} \mid \theta^*)} = \frac{p(\theta^* \mid \mathcal{D})}{p(\theta^{d-1} \mid \mathcal{D})} \tag{3.7}$$

   (c) Set

   $$\theta^d = \begin{cases} \theta^* & \text{with probability } \min\{1, r\}, \\ \theta^{d-1} & \text{otherwise.} \end{cases} \tag{3.8}$$

The starting point in Step 1 can be based on some approximation of the property of the posterior. Practically, the first portion of the generated points before the Markov chain stabilizes is often discarded as a *burn-in* period. In Step 2 (a), a normal (Gaussian) distribution, for example, can be used as a symmetric proposal distribution. Step 2 (c) can be executed by generating a uniform random value u_d (a value drawn from the unit uniform distribution $[0, 1]$), then accepting the proposal θ^* if $r > u_d$, otherwise rejecting it and retaining the old value θ^{d-1}.

The reason why this simple algorithm can estimate the correct posterior distribution (*target distribution*) is due to the Ergodic Theorem. It states that, if the sequence $\{\theta^1, \theta^2, \ldots\}$ is an irreducible, aperiodic, and recurrent Markov chain, then it has a unique distribution that is *stationary*, and the stationary distribution equals the target distribution. The details of the proof for the case of the Metropolis algorithm are described in Refs. [163, 166].

In an *irreducible* Markov chain, it is possible to jump from any state eventually to any other state. This property is satisfied in a random-walk, since the proposal distribution J_d has positive probability everywhere. *Aperiodicity* is where a Markov chain does *not* visit a specific value periodically, e.g., every k-th iterations. Starting a Markov chain at some value θ, if the probability of returning to the value θ after an infinite number of steps is equal to 1, then this Markov chain is said to be *recurrent*. A random-walk Markov chain satisfies all of these properties.

When a sample θ^d is drawn from a *stationary* distribution π and θ^{d+1} is generated conditionally on θ^d from the Markov chain, then the unconditional distribution of θ^{d+1} is also π. The proof that the stationary distribution of the Metropolis algorithm is unique and equals the target distribution $p(\theta \mid \mathcal{D})$ can be given by computing the joint probability of θ^a and θ^b drawn from $p(\theta \mid \mathcal{D})$ labeled so that $p(\theta^b \mid \mathcal{D}) > p(\theta^a \mid \mathcal{D})$, and showing that the marginal distributions of θ^a and θ_b computed from the joint probability are identical to $p(\theta \mid \mathcal{D})$ (see e.g. Ref. [166]).

In practice, it is known that a random walk becomes increasingly inefficient in exploring high-dimensional parameter spaces. Most commonly used probabilistic programming languages, such as STAN, PYMC, BUGS, EMCEE, and so on, implement a sampler called the "No-U-Turn Sampler (NUTS)", which is an extension to the Hamiltonian Monte Carlo (HMC) method. In HMC, the parameter space is explored in analogy to Hamiltonian dynamics, like a ball moving on a friction-less

curved surface. Therefore, the point of the sample moves around as if the point has a momentum, and the movement of the point is affected by the gradient of the logarithmic of the posterior (log-posterior) distribution with respect to the parameters [171–173]. However, HMC has parameters that require manual and careful tuning to control its behavior. NUTS overcame this challenge by automatically tuning such parameters through a recursive algorithm [174]. In Chapter 4, we will employ NUTS implemented by PyMC [175].

3.3 Variance-Based Sensitivity Analysis Method

In the context of the *r*-process nucleosynthesis, a notable previous work on sensitivity analysis focusing on nuclear physics inputs in nucleosynthesis calculations has been performed by Ref. [82]. Sensitivity here means how much predicted observables of the *r*-process, such as abundance patterns and kilonova lightcurves, are affected by the change in the nuclear physics inputs such as nuclear masses, decay half-lives, and so on. Identifying nuclear physics inputs with large sensitivities allows us to focus the experimental and theoretical effort on such nuclei to improve our understanding of the *r*-process. In their work, sensitivities of the calculated abundances to various nuclear physics observables, such as β-decay half-lives, β-delayed neutron emission probabilities, neutron capture rates, and masses, were estimated for the entire chart of nuclide.

While this work has provided significant insight into the dependence of the calculated abundances on the individual nuclear physics inputs, their sensitivity analysis method faced several challenges. The sensitivities were estimated by changing one input at a time, with or without propagating the variation to other inputs, and summing the absolute differences of the output from the baseline over all mass numbers. This one-at-a-time scheme implicitly assumes linearity and additivity in the response of the calculation to the change in the input [176]. Since nucleosynthesis calculations often show non-linear relations between variations of reaction/decay rates and abundance changes [177], the sensitivity estimates based on this scheme are potentially unreliable. Furthermore, with this method the space of the input variables, whose dimension is equal to the number of the variables, is largely unexplored.

Ref. [177] studied the effect varying the (α,n) reaction rates employing a Monte Carlo approach, in the context of neutrino-driven ejecta in core collapse supernovae. With the Monte Carlo method it is possible to explore the entire variable space. In identifying the key reaction rates, Spearman's correlation coefficient was employed as sensitivity metric, which assumes a monotonic relationship between the output (elemental abundance) and the variation of an input (e.g. an (α,n) reaction rate). While the assumption of a monotonic relationship is an improvement from the linear assumption in Refs. [178, 179], which employed Pearson's correlation coefficient, there is no guarantee that the relationship is always monotonic.

In our sensitivity analysis, we employ the variance-based sensitivity analysis method. This method is also based on a Monte Carlo approach and it determines the individual contribution of input variables to the uncertainty (variance) of the output of the model [180]. The same method has recently been applied in a study of *ab initio* nuclear theory [181].

Below, we outline the variance-based sensitivity method based on the work presented in Ref. [180] The notation in this section follows that of the paper. Interested readers are referred to [180, 182] for more detailed discussions of the method. As explained in the main text of the current work, this method quantifies the contribution of the uncertainty (variance) of each input variable to the uncertainty of the output. In the work presented in Chapter 5, the input variables correspond to the experimental β-decay half-lives ($T_{1/2}$) and the β-delayed one-neutron emission probabilities (P_{1n}), and the output corresponds to the nuclear abundances as a function of mass numbers. A more detailed introduction to the variance-based sensitivity analysis method is provided below.

Suppose that a numerical model can be expressed as $Y = f(X_1, X_2, \ldots, X_k)$, where Y is the output (e.g. nuclear abundance for a given mass number), X_i $(i = 1, 2, \ldots, k)$ are the input variables (e.g. $T_{1/2}$ and P_{1n} values), and $f(\cdot)$ is the simulation (e.g. nucleosynthesis post-processing code). Assuming for now that $X_1, X_2, \ldots, X_k$ are independently and uniformly distributed in $[0,1]$, the following decomposition of the overall output variance $V(Y)$ is proven unique by [183]:

$$V(Y) = \sum_i V_i^{(1)} + \sum_i \sum_{j>i} V_{ij}^{(2)} + \cdots + V_{12\ldots k}^{(k)}, \tag{3.9}$$

where V_i is the output variance due to the variance of input variable X_i, and the definition is similar for V_{ij} and other higher order terms. Dividing both sides by $V(Y)$,

$$1 = \sum_i S_i^{(1)} + \sum_i \sum_{j>i} S_{ij}^{(2)} + \cdots + S_{12\ldots k}^{(k)}, \tag{3.10}$$

where $S_i^{(1)} = V_i^{(1)}/V(Y)$ is called a first-order sensitivity index for X_i, $S_{ij}^{(2)} = V_{ij}^{(2)}/V(Y)$ is a second-order sensitivity index, and so on. These partial variances $V_i^{(1)}$, $V_{ij}^{(2)}$ and so on can be written as (see [180, 183] for more details)

$$V_i^{(1)} = V_{X_i}\left(E_{\boldsymbol{X}_{\sim i}}(Y \mid X_i)\right), \tag{3.11}$$

$$V_{ij}^{(2)} = V_{X_i X_j}\left(E_{\boldsymbol{X}_{\sim ij}}(Y \mid X_i, X_j)\right) \tag{3.12}$$

$$- V_{X_i}\left(E_{\boldsymbol{X}_{\sim i}}(Y \mid X_i)\right) - V_{X_j}\left(E_{\boldsymbol{X}_{\sim j}}(Y \mid X_j)\right), \tag{3.13}$$

and so on. In Eq. 3.11, $E_{\boldsymbol{X}_{\sim i}}(Y \mid X_i)$ denotes the expectation value (average) of Y when the value of X_i is fixed, and $E_{\boldsymbol{X}_{\sim i}}$ means that the average is taken over all the possible values of all the variables except for X_i. Therefore, $V_{X_i}\left(E_{\boldsymbol{X}_{\sim i}}(Y \mid X_i)\right)$ means that the variance of the expected value is computed over all the possible values of X_i. More intuitively, as shown in Fig. 3.1, this is equivalent to calculating the average of the values of Y of the samples by "slicing" the samples at a given value of the input X_i, then estimating how much the average varies as the samples are sliced at all the possible values of X_i. With this, the sensitivity indices can be written as

$$S_i^{(1)} = \frac{V_{X_i}\left(E_{\boldsymbol{X}_{\sim i}}(Y \mid X_i)\right)}{V(Y)}, \tag{3.14}$$

$$\begin{aligned} S_{ij}^{(2)} &= \frac{V_{X_i X_j}\left(E_{\boldsymbol{X}_{\sim ij}}(Y \mid X_i, X_j)\right) - V_{X_i}\left(E_{\boldsymbol{X}_{\sim i}}(Y \mid X_i)\right) - V_{X_j}\left(E_{\boldsymbol{X}_{\sim j}}(Y \mid X_j)\right)}{V(Y)} \\ &= S_{ij}^{(2),\text{closed}} - S_i^{(1)} - S_j^{(1)}, \end{aligned} \tag{3.15}$$

and so on, where $S_i^{(1)}$ and $S_{ij}^{(2)}$ are called first-order and second-order sensitivity indices, respectively, and $S_{ij}^{(2),\text{closed}} \equiv \frac{V_{X_i X_j}\left(E_{\boldsymbol{X}_{\sim ij}}(Y|X_i,X_j)\right)}{V(Y)}$ is called the closed second-order sensitivity index, since the definition is closed within the subset of inputs $\{X_i, X_j\}$.

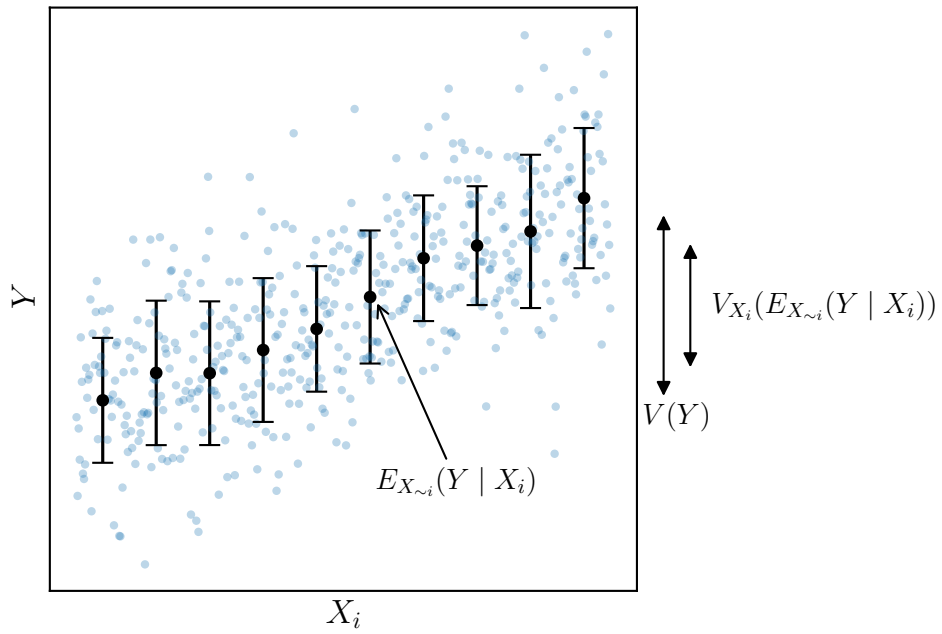

Figure 3.1: Conceptual schematics of the meaning of the value $V_{X_i}\left(E_{\boldsymbol{X}_{\sim i}}(Y \mid X_i)\right)$ in Eq. 3.11.

While we have assumed so far that the input variables are uniformly distributed in $[0,1]$, this method can be used with general distributions such as a normal distribution or uniform distributions that are not in $[0,1]$, since random numbers uniformly distributed in $[0,1]$ can be transformed to desired distributions through inverse transform sampling, as long as they are independently distributed and their cumulative distribution functions are known. The sensitivity indices can then be defined in a similar manner for general distributions [182].

Monte Carlo estimate of sensitivity indices

In practice, the sensitivity indices (e.g. Eqs. 3.14 and 3.15) cannot be computed analytically. Therefore, we compute their Monte Carlo estimates instead. In order to illustrate the Monte Carlo method, we use first-order sensitivity indices (Eq. 3.14) as an example.

Suppose that we have k variables of interest and wish to use N samples to com-

pute their Monte Carlo sensitivity estimates. The first step is to generate samples that are uniformly distributed in $[0,1]$. While random numbers can be used for this purpose, we employ a Sobol quasi-random sequence implemented in a `Python` library called `SALib` [184]. Sobol quasi-random sequences are designed to generate multi-dimensional uniform samples in $[0,1]$ to efficiently explore the entire variable space by filling the gap between previously sampled points [180]. Using the quasi-random sequence, we generate $N \times 2k$ samples and split them into two matrices of size $N \times k$.

The next step is to transform the uniformly distributed samples for each variable in the two matrices into the desired distributions. In the study described in Chapter 5, the half-lives are assumed to follow truncated normal (Gaussian) distributions with their means and standard deviations defined by the experimental values and uncertainties. The β-delayed one-neutron emission probabilities (P_{1n} values) are either truncated normal distributions or uniform distributions in $[0, (\text{upper limit of } P_{1n})]$. The samples uniformly distributed in $[0,1]$ can be transformed into these distributions through inverse transform sampling. For convenience, we call the first of the two transformed $N \times k$ matrices $\boldsymbol{A}$ and the second matrix $\boldsymbol{B}$. Using these matrices, the first-order sensitivity index is estimated by (based on Eq. 16 of [180] and Eq. 30 of [182])

$$\hat{S}_i{}^{(1)} = \frac{\frac{1}{N}\sum_{j=1}^{N} f(\boldsymbol{A})_j \left(f(\boldsymbol{B}_{\boldsymbol{A}}^{[i]})_j - f(\boldsymbol{B})_j \right)}{\hat{V}(Y)}, \tag{3.16}$$

where $\hat{S}_i{}^{(1)}$ denotes a Monte Carlo estimate of $S_i^{(1)}$, and $f(\boldsymbol{A})_j$ as well as $f(\boldsymbol{B})_j$ are the output of the simulation run with the j-th row ($j = 1,2,\ldots,N$) of the matrices $\boldsymbol{A}$ and $\boldsymbol{B}$, respectively. $\boldsymbol{B}_{\boldsymbol{A}}^{[i]}$ is a $N \times k$ matrix whose i-th column ($i = 1,2,\ldots,k$) comes from the matrix $\boldsymbol{A}$ but all the other columns come from the matrix $\boldsymbol{B}$. Consequently, $f(\boldsymbol{B}_{\boldsymbol{A}}^{[i]})_j$ is the output of the simulation run with the j-th row of $\boldsymbol{B}_{\boldsymbol{A}}^{[i]}$. $\hat{V}(Y)$ is the total variance of the output of the simulation, computed with all the generated samples. Errors of the computed sensitivity indices can be estimated using a method called bootstrapping [185].

3.4 Neural Networks

While the variance-based sensitivity analysis method (Section 3.3) is useful for identifying influential parameters in the model and MCMC (Section 3.2) is useful for estimating the likely values of the parameters from the data, one is sometimes interested in extracting the patterns and physical laws from the data. In such case, it is often effective to fit flexible models to the data. Neural networks have recently gained popularity due to their flexibility and ability to interpolate/extrapolate the observed data [186]. Such models can be used for constructing fast *emulators* of complex numerical models, which would otherwise take a large amount of computational cost and time. In this section, the basics of neural networks are presented, which are used in Chapter 6 to construct an emulator of a nuclear reaction network calculation code (Section 1.3).

Feed-forward Artificial Neural Network

Feed-forward artificial neural networks (ANNs) can be described as a series of functional transformations, where an input (vector) $\boldsymbol{x}$ is propagated through intermediate layers, and finally to the output (vector) $\boldsymbol{y}$ [164, 186]. For example, if an ANN has three layers that are connected in a chain, it can be expressed as $f(\boldsymbol{x}) = f^{(3)}\left(f^{(2)}\left(f^{(1)}(\boldsymbol{x})\right)\right)$. An ANN with trainable parameters, or *weights* $\boldsymbol{w}$, defines a mapping $\boldsymbol{y} = f(\boldsymbol{x}, \boldsymbol{w})$, which is trained to approximate some function $\boldsymbol{y} = f^*(\boldsymbol{x})$. Training is typically performed using variations of (stochastic) gradient descent algorithms to minimize cost functions, such as the mean squared error cost function. The information from the cost function is propagated backwards through the network to compute the gradient of the cost function with respect to the trainable parameters, using the back-propagation algorithm. Much of the design of architectures of ANNs goes into the choice of type, number (depth) and width of layers, and how each layer is connected. In what follows, the two types of layers used in the design of the current architecture of ANNs are described. Please see Ref. [186] for more details.

Implementation of the neural networks are done by using an ANN library called KERAS [187], which provides a high level application programming interface (API) for TENSORFLOW [188] in PYTHON.

Fully Connected Layers

In a fully connected (or dense) layer, linear combinations of the input of the layer are first constructed. Taking the first layer of the ANN as an example and following the notation in [164], the linear combination can be written as

$$a_j = \sum_{i=1}^{D} w_{ji}^{(1)} x_i + w_{j0}^{(1)}, \tag{3.17}$$

where $j = 1, \ldots, M$ with M being the dimension of the layer, D the dimension of the input $\boldsymbol{x} = x_1, \ldots, x_D$, $w_{ji}^{(1)}$ the weights with the superscript (1) denoting first layer, and $w_{j0}^{(1)}$ the biases. Each of a_j is subsequently transformed using nonlinear activation function $h(\cdot)$ to obtain outputs of the layer

$$z_j = h(a_j). \tag{3.18}$$

In the work presented in Chapter 6, the activation function is chosen to be the rectified linear unit (ReLU) $h(a_j) = \max\{0, a_j\}$ [189], which is one of the most widely used activation functions. The subsequent layers take the output of the previous layers, and the functional transformations can be operated in the same manner. In the final layer, the identity activation function (where the output of the function is identical to the input) is used to allow for unbounded values.

Convolutional Layers

Convolutional neural networks (CNNs) are a type of ANNs where convolution is used in at least one of the layers. CNNs are used most extensively in the field of computer vision. The central assumption in CNNs is that nearby pixels in the image data or neighboring data points in time-series data are strongly correlated [164, 186]. Based on this assumption, it is possible to extract the local features in the data. The general convolution operation for multidimensional arrays can be expressed as [186]

$$\begin{aligned} S(i,j) &= (I * K)(i,j) \\ &= \sum_m \sum_n I(m,n) K(i-m, j-n), \end{aligned} \tag{3.19}$$

where I is a multidimensional array image input, K is called a kernel (which is a multidimensional array that stores the adaptive weights), and $S(i, j)$ is the output and is often referred to as a feature map.

In the actual implementation of convolution for machine learning purposes, convolution is typically performed for a small subregion in an input image for each element in a feature map. Furthermore, the weights in a feature map are used for all the elements in an input, which is the concept called "weight (parameter) sharing". These reduce the number of weights that are stored in the memory, making it possible to process images that have a large number of pixels. Each unique set of weights is often referred to as a filter, which acts to detect different features in the input data. The use of convolutional layers for nuclear data is motivated by the fact that the properties of neighboring nuclei on the chart of nuclides are highly correlated.

Uncertainty quantification with deep ensembles

In emulation of computer codes, one of the most popular approaches is to use a probabilistic model called Gaussian processes (GPs) [190, 191, 191, 192]. GPs provide a natural way to quantify the prediction uncertainty in terms of the quality of the emulation. On the other hand, typical ANNs including CNNs have deterministic weights, therefore their predictions are also deterministic. One approach to overcome this limitation for ANNs is to employ Bayesian neural networks (BNNs) [171] where the weights are expressed as probability distributions. Similarly to GPs, it is possible to quantify the prediction uncertainty of BNNs due to their probabilistic nature. However, the computational complexity of BNNs is large compared to traditional ANNs, and the application to CNNs is technically challenging for non-experts.

The approach we employ in this thesis to quantify prediction uncertainty is called *deep ensembles*, which is a simple and scalable method and has been shown to provide robust and accurate estimates of uncertainty, comparable to BNNs [193]. The central idea of deep ensembles for regression is to create a copy of M (ensemble size, in our case, $M = 10$) ANNs with the same architecture with random initialization. The final layer of the ANN architecture is replaced with a layer with

two outputs: a predictive mean $\mu(\boldsymbol{x})$ and a predictive variance $\sigma^2(\boldsymbol{x})$. The predictive mean and variance of the ensemble are obtained by treating the ensemble of ANNs as a uniformly weighted mixture of Gaussian distributions.

Chapter 4

Ensemble Bayesian Model Averaging of Nuclear Mass Models

Since the first introduction of the nuclear liquid drop model, the theoretical description of nuclear masses has seen great progress, which gave rise to many related but different approaches. It is now possible to describe the ground state properties of nuclei across the chart of nuclei with theories of different scales (see Section 2.2): Macroscopic-microscopic theories such as the Finite-Range Droplet Model (FRDM) [119, 132], Weizsäcker-Skyrme (WS) models [145, 149, 150, 152], microscopically inspired Duflo-Zucker models [153], and more microscopic theories such as the nuclear density functional theory (DFT) with different interactions or energy density functionals (EDFs) [143, 194, 195].

These global mass models play a particularly important role in understanding the origin of heavy elements in the Universe via the rapid neutron capture process (*r*-process) [45, 82, 196, 197]. This is because the nuclear masses determine the Q-value (energy release) of nuclear reactions and decays, which also affect their rates (rates $\propto Q^{3-7}$ [198, 199]), but the masses of the vast majority of neutron-rich isotopes relevant to the *r*-process have yet to be experimentally studied. The masses also determine the fission barriers, which become important for very heavy nuclei where fission is the dominant decay mode. Therefore, mass models used in nucle-

osynthesis studies have a significant impact on the resulting abundance patterns and kilonova lightcurves. However, one of the challenges in understanding the impact of mass models in nucleosynthesis is that, in general, we do not have uncertainty estimates associated with the theoretical masses. While there has been an effort to quantify uncertainty in microscopic theories [200, 201], the mass models that are typically used in nucleosynthesis studies, especially macroscopic-microscopic and phenomenological models, do not come with quantified prediction uncertainty. One may calculate the root-mean-squared error of each mass model with respect to the observations, but it most likely underestimates the uncertainty where no data exist (see Figure 2.5). Furthermore, the possibility of quantifying the uncertainty by combining multiple mass models and observations has largely been unexplored. This poses a challenge in quantifying the uncertainty in r-process nucleosynthesis that arises from uncertain nuclear masses.

As the next-generation radioactive isotope beam facilities allow us to have access to more neutron-rich isotopes, it becomes possible to test the performances of the mass models in the extremely neutron-rich regions of the chart of nuclides. However, in experimental studies of nuclear masses, usually only the new experimental results are compared to the theoretical predictions. It is often done by calculating the root mean squared (RMS) error (for examples of mass measurements relevant to the *r*-process, see Refs. [202–205]), but this does not fully combine all the available experimental data. Therefore, a statistical method to test the predictions of various theoretical models and evaluate the impact of new measurements on the uncertainty of extrapolated masses would be an improvement to the current situation.

In this work, we will apply a method called *ensemble Bayesian model averaging* (EBMA) introduced by Ref. [206] to combine available experimental data and multiple theoretical mass models as well as quantify the mass uncertainty. This method models an ensemble of theoretical mass models as a mixture of normal distributions, whose parameters are estimated based on the observations. The EBMA combines model calibration, selection, averaging, and uncertainty quantification in a single framework and the resulting probabilistic model is highly interpretable. This Bayesian method is quite general and it can be readily applied to other nuclear physics observables such as β-decay half-lives.

Recently, data-driven modeling of nuclear masses using machine learning techniques has been quickly gaining popularity [207–214]. Especially, probabilistic models have achieved high accuracy while providing an estimate of uncertainty. These machine learning approaches usually model the residuals of a theoretical nuclear mass model from experimental data, and are providing corrections to the theoretical mass model. However, while there have been attempts to construct physically interpretable models [214], it is generally difficult to gain insight into the underlying physics from the learned residuals. Furthermore, these machine learning methods do not provide a way to perform a model selection to test existing theoretical models that are described with known physics.

The purpose of this study, on the other hand, is not to create another mass model or to improve existing ones. Rather, we aim to investigate how well a set of theoretical models can reproduce experimental data and quantify the performance of each model in the ensemble. This quantifies the uncertainty in extrapolating the experimental data. Our approach should be considered as a method for model averaging, selection, calibration, and uncertainty quantification, using only existing theoretical models.

4.1 Method

4.1.1 Bayesian model averaging

We start by describing the general framework of Bayesian model averaging (BMA). BMA is applicable when more than one statistical model that describes the data reasonably well is available, and one wishes to account for the uncertainty in the analysis arising from conditioning on a single model. BMA computes a weighted average of the probability density functions (PDFs), weighted by the posterior probability of the "correctness" of each model given the training data. Following the description in Refs. [206, 215], the posterior distribution of the observable of interest Δ, defined by BMA, is

$$p(\Delta \mid D) = \sum_{k=1}^{K} p(\Delta \mid M_k, D)\, p(M_k \mid D), \tag{4.1}$$

where $p(\Delta \mid M_k, D)$ is the posterior PDF of the observable of interest based on a single statistical model M_k, and $p(M_k \mid D)$ is the corresponding posterior model probability, which represents how well model M_k fits the data D. The posterior model probabilities can be considered as weights, since their sum is equal to 1.

4.1.2 Ensemble Bayesian model averaging

One of the limitations in the applicability of the BMA method is that the participating models themselves need to be probabilistic. However, in nuclear physics, many models only provide point estimates of the quantity of interest. Therefore, we need to extend the BMA framework to handle such deterministic models. Raftery et al. [206] introduced the *ensemble Bayesian model averaging* (EBMA) method, which computes the weighted average of an ensemble of bias-corrected deterministic models, as a finite mixture of normal distributions. In the EBMA framework, the predictive model is

$$p(\Delta \mid m_1, \ldots, m_k) = \sum_{k=1}^{K} w_k \, g_k(\Delta \mid m_k), \tag{4.2}$$

where w_k is the weight of the model m_k, whose posterior represents the probability of the model k being the best one, based on the observed data D. $g_k(\Delta \mid m_k)$ is a normal PDF with mean defined by the bias-corrected deterministic model predictions and standard deviation σ_k:

$$g_k(\Delta \mid m_k) = N(\Delta \mid a_k + b_k m_k, \sigma_k^2), \tag{4.3}$$

where a_k and b_k are the bias-correction coefficients, which are discussed in more detail in the following section. In the original EBMA by Raftery et al. [206], a constant standard deviation was used across all the models in the ensemble; however, we take it as model dependent (denoted by subscript k), which is a more natural way to construct a mixture model.

Bias correction

In constructing EBMA models, although not strictly necessary, Ref. [206] linearly corrects the bias of the prediction of each model, as shown in Equation 4.3. Since most mass models are already fit to experimental data, the values of the bias-correction coefficients are expected to be $a_k \sim 0$ and $b_k \sim 1$, where the original prediction of the model is obtained when $a_k = 0$ and $b_k = 1$.

Ref. [206] suggests that a_k and b_k for each $k = 1, \ldots, K$ are determined by linear regression. Another way to determine these parameters a_k and b_k is by Bayesian linear regression and taking the *maximum a posteriori* (MAP) values, which is a slightly more probabilistic treatment. However, in our case, the two approaches yield virtually identical values.

Bayesian inference

The parameters of interest in our statistical inference are the weights $w_k (k = 1, \ldots, K)$ and the standard deviations of the normal distributions that correspond to each of the theoretical mass models in the ensemble. Therefore, prior distributions for the parameters must be specified. In general, we try to choose the prior distributions to be as weakly informative as possible. For the weights, since the weights have to sum up to one: $\sum_{k=1}^{K} w_k = 1$, we model the parameters with a Dirichlet distribution of order K, which meets this requirement. Therefore, the prior for the weights is

$$\begin{aligned} p(w_1, w_2, \ldots, w_k) &= \text{Dirichlet}(w_1, w_2, \ldots, w_k \mid \alpha_1, \alpha_2, \ldots, \alpha_k) \\ &= \frac{\Gamma\left(\sum_{k=1}^{K} \alpha_k\right)}{\prod_{k=1}^{K} \Gamma(\alpha_k)} \prod_{k=1}^{K} w_k^{\alpha_k - 1}, \end{aligned} \tag{4.4}$$

where $\alpha_1, \alpha_2, \ldots, \alpha_k$ are called the "concentration parameters", and $\Gamma(\cdot)$ is the gamma function[1]. The concentration parameters of the Dirichlet distribution are set to 1 to ensure that the prior distributions are only weakly informative. The prior distributions for the standard deviations are chosen to be exponential distributions with the rate parameters equal to 1, which has been suggested to be one of the weaker priors [168].

[1] $\Gamma(z) \equiv \int_0^\infty t^{z-1} e^{-t} \mathrm{d}t$.

The likelihood of the normal mixture model is defined as

$$L(w_1, \ldots, w_K, \sigma_1^2, \ldots, \sigma_K^2) = \prod_{n,p} \left(\sum_{k=1}^{K} w_k g_k(\Delta_{n,p} \mid m_{k,n,p}) \right), \tag{4.5}$$

where the subscripts n and p represent the neutron and proton number of the nuclei where the observations exist. In practice, the logarithm of the likelihood (log-likelihood) is often used for computation to avoid numerical problems.

With the prior distributions and the likelihood function, it is now possible to formulate the posterior distributions for the parameters of the EBMA model.

$$p(\boldsymbol{w}, \boldsymbol{\sigma^2} \mid D) \propto L(\boldsymbol{w}, \boldsymbol{\sigma^2})\ p(\boldsymbol{w})\ p(\boldsymbol{\sigma^2}), \tag{4.6}$$

where $\boldsymbol{w} = w_1, \ldots, w_K$ and $\boldsymbol{\sigma^2} = \sigma_1^2, \ldots, \sigma_K^2$ and D denote observational data. The prior distributions are denoted as $p(\boldsymbol{w})$ and $p(\sigma^2)$, respectively.

Predictive variance

In EBMA models, the uncertainty of the quantity of interest is provided in the form of variance of the posterior predictive distribution. Based on Ref.[206] but reflecting the fact that our σ_k depends on model k, the predictive variance can be written as

$$\mathrm{Var}(\Delta \mid m_1, m_2, \ldots, m_K) = \sum_{k=1}^{K} w_k \left((a_k + b_k m_k) - \sum_{k_1}^{K} w_k (a_k + b_k m_k) \right)^2 + \sum_{k=1}^{K} w_k \sigma_k^2, \tag{4.7}$$

where the first term corresponds to the spread of predictions by the member mass models of the ensemble, and the second term corresponds to the expected deviation from the observations of each mass model, weighted by the posterior weights.

Differences to related works

It is worth discussing the key differences between our framework and the related studies that use the BMA method, namely, Refs.[209, 210, 216–218]. In their BMA framework, the uncertainty quantification of the considered mass models is performed by constructing Gaussian Process (GP) emulators, which learn the corrections to the mass models from the residuals with respect to the observed values. Therefore, the quality of prediction and corresponding uncertainty mainly rely on the performance of the GP emulator. The BMA weights are calculated either based on some criteria such as nuclei being bound, or the performances of each mass model on the test data. One of the drawbacks of this method is that the derived weights are point estimates and the resulting BMA uncertainty is a deterministic weighted average of the GP uncertainties. Furthermore, one has to be cautious in performing extrapolations using GPs, since an unconstrained GP converges to its mean with fixed uncertainty away from the data [190, 219].

On the other hand, the EBMA framework keeps the deterministic nature of the mass models in the ensemble. Instead, the weights and variances associated with each mass model are modeled probabilistically based on the experimental data. The probabilistic distributions are reflected onto the resulting predictive uncertainty through the Bayesian framework. In this framework, the predictions of each mass model that constitute the EBMA model are only linearly calibrated; therefore, the local trend of the predictions remain unchanged.

4.1.3 Setup of numerical experiment

In the numerical experiments discussed in the current work, all the probabilistic models have been implemented using PyMC [175], which is a probabilistic programming language written in Python. PyMC offers an implementation of a highly efficient sampler called No-U-Turn-Sampler (NUTS), which adaptively tunes the parameters associated with the Hamiltonian (or Hybrid) Monte Carlo method [171, 220]. Conventionally, parameter estimation in mixture models is performed with the Expectation Maximization (EM) algorithm to avoid the so-called "label switching problem" [221, 222]. The label switching problem arises in mixture models like the EBMA models, since the likelihood (Eq. 4.5) remains

unchanged under permutation of the labels ($k = 1, \ldots K$) of the mixture components $g_k(\Delta \mid m_k)$. This makes the analysis of the posterior distributions challenging. However, the EM algorithm does not guarantee convergence to the global optimal weights and variances, especially in high-dimensional problems. Furthermore, MCMC methods would be able to provide much more complete information on the posterior distributions. In our numerical experiments, we did not find evidence of a label switching problem due to employing the MCMC method. This is most likely because, in our normal mixture models, the means of the normal distributions are always specified by the predictions of bias-corrected mass models, which works as an identifiability constraint.

The quantity of interest in our study is the one-neutron separation energy (S_n), which is directly relevant to the *r*-process. The mass models included in our ensembles are the Duflo-Zucker mass model with 29 parameters (DZ29) [153], FRDM2012 [119], HFB31 [143], KUTY05 [156], ETFSI2 [148], and WS4 [152]. In most of our numerical experiments, we take the S_n values from the AME2020 [10] as observations. In evaluating the quality of uncertainty estimates for unseen data, we use the S_n values from AME2003 [223] for constructing our models and then test them with the new data points in AME2020. In the AME2020, 319 new S_n data points with proton number $Z = 16$-105 are available compared to the AME2003. The new data points in the AME2020 compared to the AME2003 are shown in Figure 4.1.

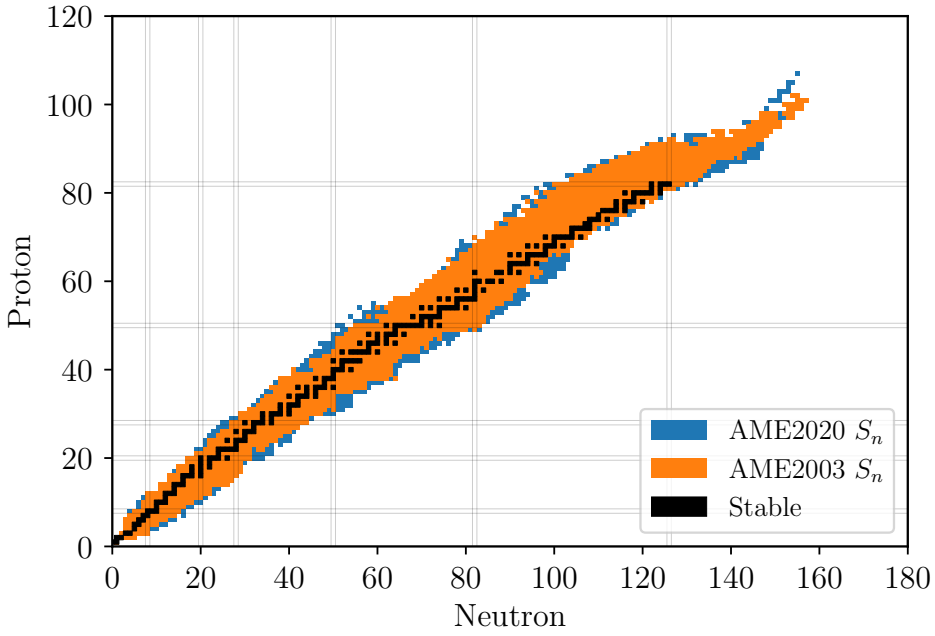

Figure 4.1: Comparison of the AME2003 data with the latest AME2020 data for one-neutron separation energies S_n, illustrated on the chart of nuclides. The blue squares show the new S_n in the AME2020 values that did not exist in the AME2003. The S_n values listed in the AME2003 are shown in orange color.

We consider four different ways to categorize the S_n data. The first category is the data for the whole chart of nuclides, which employs all the available experimental data at once. The second and third are data for each isotopic and isotonic chain, respectively. This focuses on the evolution of the S_n values as a function of proton and neutron number (isotopic and isotonic, respectively). The last is isobaric (equal mass number A), to demonstrate that it is possible to create an EBMA model for each isobaric chain, which is relevant to the trend of β^--decay Q-values.

4.2 Results and Discussion

4.2.1 Comparison with observations

To compare the predictions of the EBMA model with the observations (data from AME2020), nominal EBMA predictions are taken as the MAP values of the predictive distributions of S_n, with the bias-correction parameters, weights, and the standard deviations σ_k (Equation 4.3) determined also from the AME2020 values. Since the AME2020 values are used for both fitting and evaluation of the performance, this analysis reveals how well the EBMA method can reproduce known experimental data using the constituent mass models.

Figures 4.2 and 4.3 show the deviations of the EBMA predictions of the one-neutron separation energies (S_n) from the AME2020 values. The value of the σ_{Sn} of the fit of the entire chart of nuclides (panel (a)) shows that the averaged mass model created by the EBMA method can reproduce the experimental values slightly better ($\sigma^{(a)}_{\mathrm{RMSE}} = 0.232$ MeV) than the best performing model, which is the WS4 model [152] with $\sigma^{\mathrm{WS4}}_{\mathrm{RMSE}} = 0.257$ MeV (see Table 4.1). Further reduction in σ_{RMSE} is achieved when S_n of each isotopic chain is fit separately (panel (b) of Figure 4.2). This suggests that some models in the ensemble perform better than the overall best-performing mass model (WS4) for some isotopic chains. This can be verified by inspecting the weights of the EBMA model and will be discussed in more detail in Section 4.2.2. The best performance in reproducing the experimental S_n is obtained when separate EBMA models are optimized for each isotonic chain (panel (c) of Figure 4.3). This means that the mass models can capture the isotonic trends of S_n (S_n as functions of neutron number N) much better than the isotopic trends (S_n as functions of proton number Z), at least for the available experimental data. The fit of each isobaric chain resulted in the RMSE value of 0.171 MeV, which sits between the isotopic and isotonic models (panel (d) of Figure 4.3).

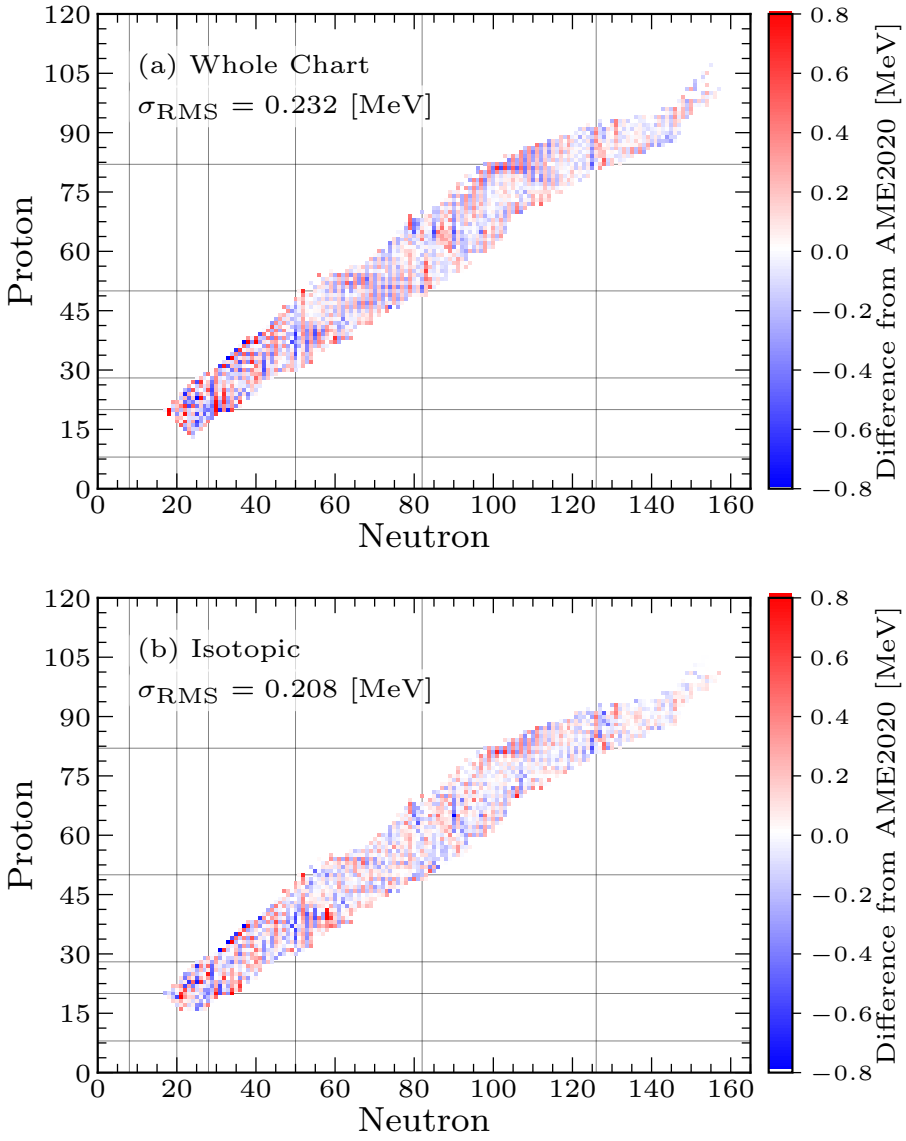

Figure 4.2: Root mean squared error (RMSE) [MeV] of the neutron separation energies S_n reconstructed by the EBMA models fitted with (a) the whole chart of nuclides and (b) each isotopic chain ($Z = \text{const.}$), compared to the AME2020 [10].

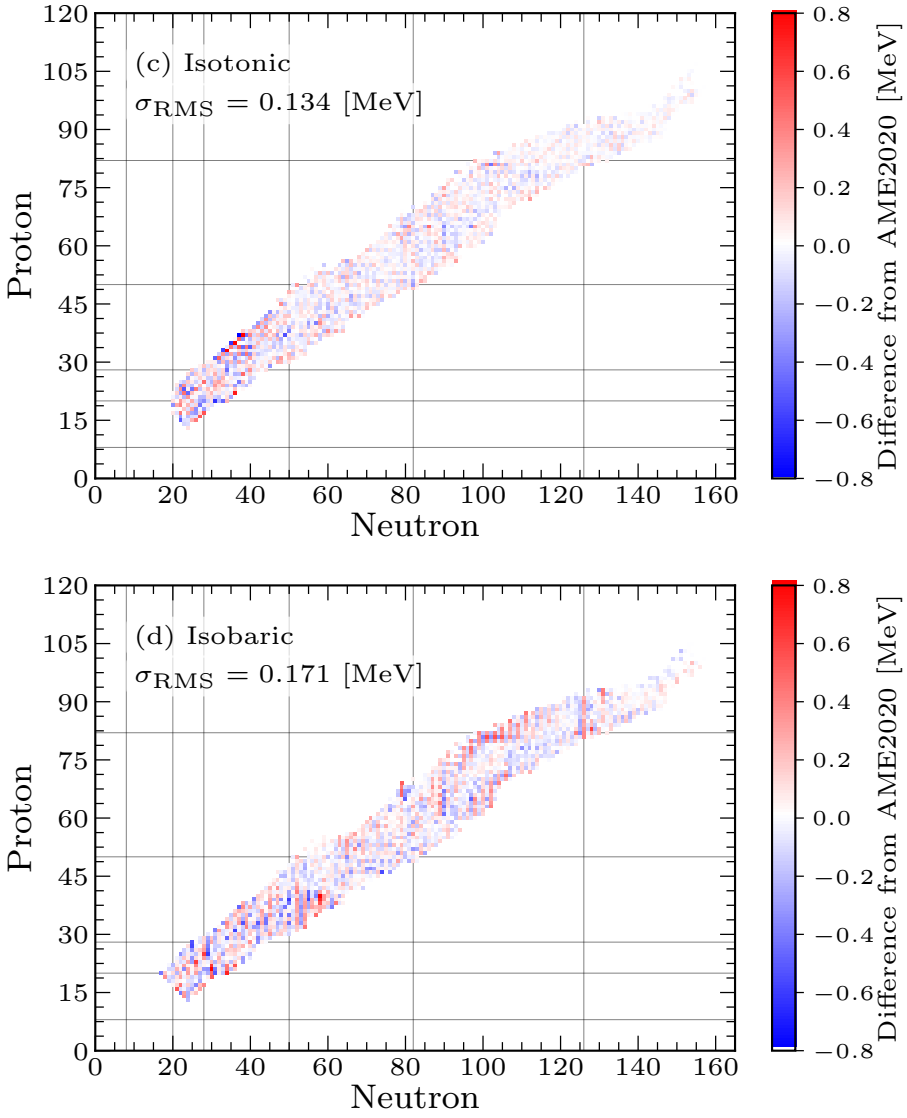

Figure 4.3: Same plot as Figure 4.2, but for (c) each isotonic chain ($N =$ const.), and (d) each isobaric chain ($A =$ const.).

4.2.2 Weights in the EBMA models

EBMA models are constructed using the S_n data from AME2020 in three different ways: optimizing the EBMA models with 1) the data for the whole chart of nuclides, 2) each isotopic chain, and 3) each isotonic chain, respectively. Table 4.1 lists the 95 % posterior highest density intervals (HDIs) of the EBMA weights and variances, which are the narrowest intervals that include 95 % of the posterior distributions, when the EBMA model is optimized with the observed S_n data for the whole chart of nuclides. The posterior weight, which can be interpreted as the probability of the model being the best one, is the largest for the WS4 model, followed by DZ29 and FRDM12. The order of the top three mass models is the same as the order of the smallest root-mean-squared errors (RMSEs) with respect to the AME2020 [10]. On the other hand, the standard deviations or variances of the normal distributions in the mixture model do not agree with the RMSE values. This is because the mixture model is a weighted sum of the normal distributions and is fitted to the data at once, not individually. It is not apparent why the posterior weight of the HFB-31 model is much smaller than the others, although the RMSE value (0.472 MeV) is smaller than the KUTY05 (0.746 MeV) and ETFSI2 (0.828 MeV) models. The HFB-31 mass model performs relatively well on average in reproducing the observed data, but it is possible that the local trend of the S_n values does not agree with the observation, therefore resulting in the small weight. Such local disagreement could also explain the large interval of the posterior standard deviation for the model (Table 4.1).

Table 4.1: 95 % posterior highest density intervals (HDI) of the EBMA weights and standard deviations (variances), fitted with the AME2020 S_n values. The notation (a, b) denotes an interval with a being the lower bound and b being the upper bound, respectively. RMSE shows the root mean squared error of each mass model with respect to the AME2020 values.

Mass model	Weight	Standard deviation	RMSE [MeV]
WS4	(0.392, 0.539)	(0.186, 0.221)	0.257
DZ29	(0.154, 0.277)	(0.134, 0.196)	0.292
FRDM12	(0.145, 0.264)	(0.143, 0.196)	0.350
KUTY05	(0.021, 0.127)	(0.134, 0.292)	0.746
ETFSI2	(0.001, 0.048)	(0.063, 0.450)	0.828
HFB31	(0.000, 0.029)	(0.138, 1.073)	0.472

The colors in Figure 4.4 show the mass model with the largest weight within the ensemble for each isotopic (panel (a)), isotonic (panel (b)), and isobaric chain (panel (c)). The color scale represents the value of the weight. The weight is the posterior probability of the mass model being the best one, based on the training using the AME2020 data. Trends of the best models in different regions are visible, especially when the ensembles are created for each isotopic chain.

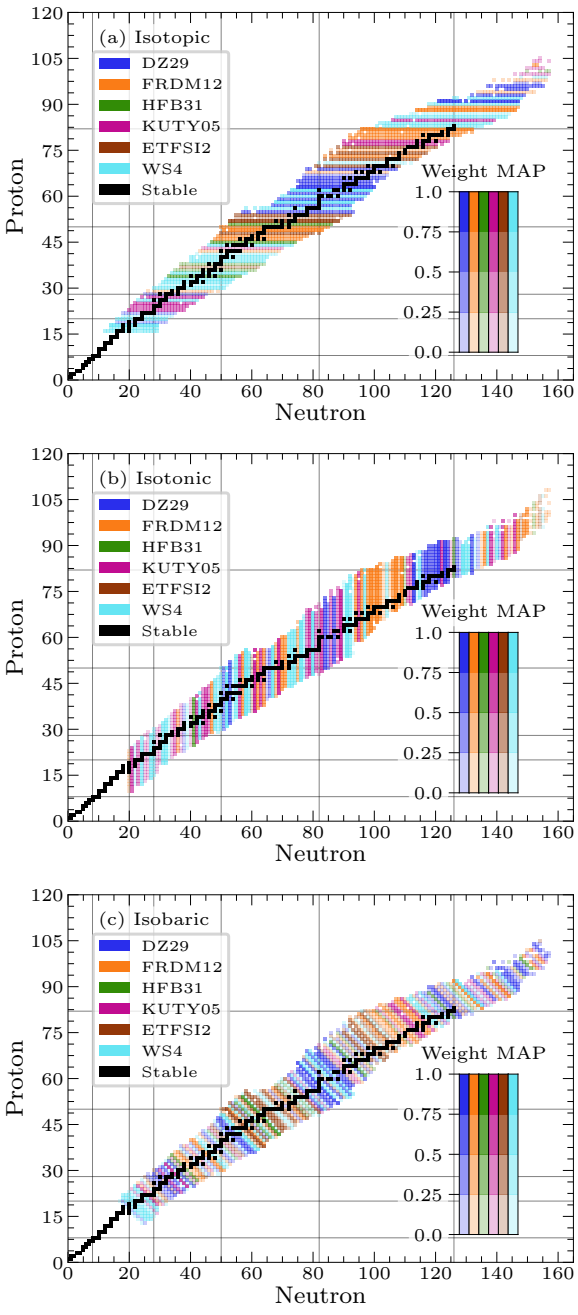

Figure 4.4: Maximum a posteriori (MAP) values of the largest weight in the EBMA ensemble determined for each (a) isotopic chain, (b) isotonic chain, and (c) isobaric chain.

4.2.3 Uncertainty quantification with EBMA

One of the main goals of this study is to quantify the uncertainty of deterministic mass models. EBMA achieves it by creating a weighted average of a collection of mass models, based on the performance of each model during the training. In the EBMA model, the predictive uncertainty includes not only the spread of the forecasts among the member of the ensemble but also take into account the weighted variance of each member model according to the performance during the training [206]. The interpretability of the uncertainty is another advantage of the EBMA method.

Figure 4.5 shows the size of the 68% highest density interval (HDI), which is roughly comparable to $\pm 1\sigma$ interval of the normal distribution, with EBMA models fitted for the entire chart of nuclides (panel (a)), each isotopic chain (panel (b)), each isotonic chain (panel (c)), and each isobaric chain (panel (d)), respectively. The fit is performed using the AME2020 data and the predictions are made for all the nuclei available in all the member mass models within the ensemble. In all the cases, it can be seen that the size of the uncertainty is constrained where the data exist, but increases towards the edge of the chart of nuclides, especially in the neutron-rich direction. This means that the predictions by the mass models constituting the ensemble start to diverge as we move further from the last data point, regardless of how the ensembles are made, as shown in Figure 4.6.

Comparing the four plots of Figure 4.5, the increase in the size of uncertainty in the neutron-rich region is the smallest for the fit using the whole chart of nuclides (panel (a)). This is likely because the weights for the whole chart of nuclides can be determined using all the available data, whereas for each isotopic, isotonic, and isobaric chains, the weights are determined only from the data in each chain. Although the isotonic fit was best performing in terms of reproducing the experimental data (Figure 4.3), it can be seen from the panel (c) of Figure 4.5, the size of uncertainty rapidly grows where experimental data do not exist.

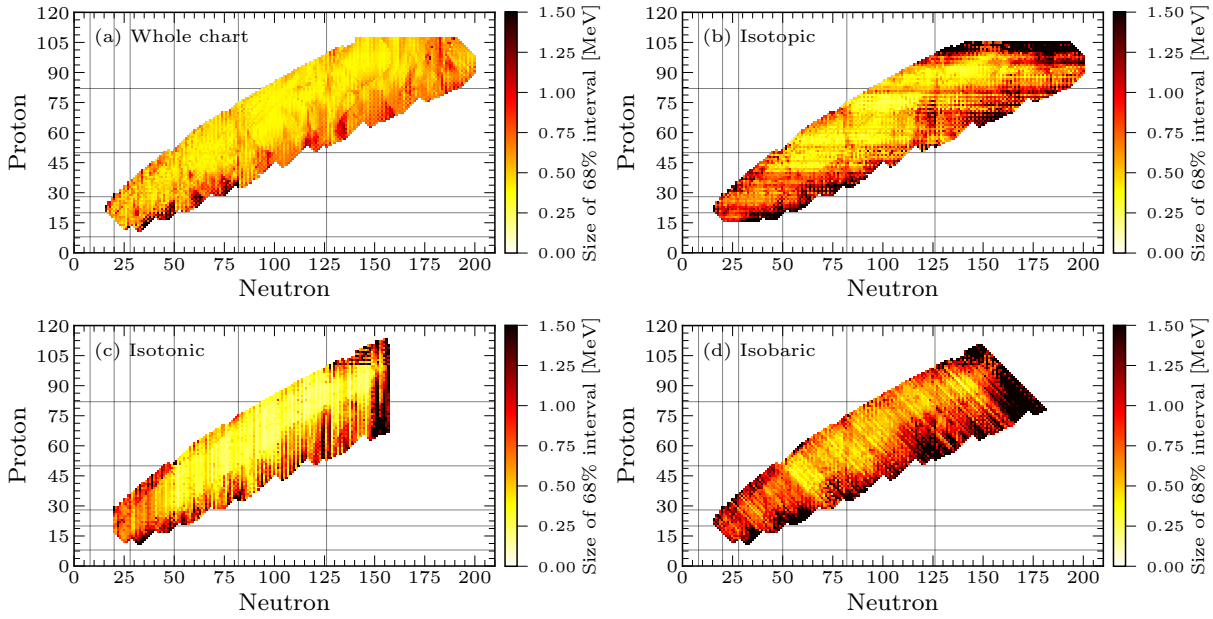

Figure 4.5: Trends of the sizes of 68% highest density intervals of the EBMA models, fitted with the AME2020 S_n data for (a) the whole chart of nuclides, (b) each isotopic chain, (c) each isotonic chain, and (d) each isobaric chain. The charts with isotonic and isobaric fits are truncated at large neutron number and mass number, respectively, because there are not enough data points within the chains to determine the EBMA parameters.

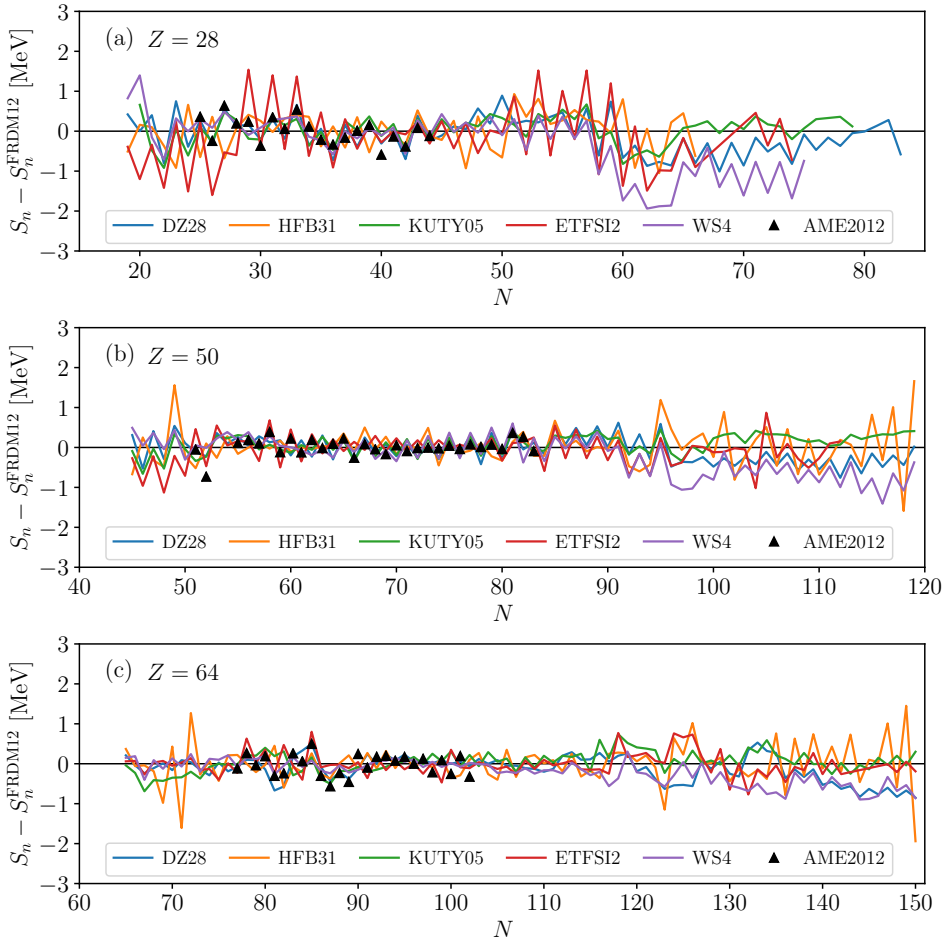

Figure 4.6: Comparisons of one-neutron separation energies (S_n) predicted by each mass model used in this study and the experimental masses from the AME2020 [10], relative to the predictions of the FRDM2012 for (a) $Z = 28$ (Ni), (b) $Z = 50$ (Sn), and (c) $Z = 64$ (Gd) isotopes.

Quality of uncertainty estimates

As discussed in Section 4.1.2, the predictive uncertainty given by the EBMA model has a straightforward interpretation. Now we investigate the quality of the estimation of the size of uncertainty. We first construct EBMA models and quantify prediction uncertainties using the data from the AME2003 [223], then evaluate the

quality of the uncertainties based on the new data from the AME2020 [10].

Figure 4.7 shows the distribution of the new S_n data relative to the sizes of uncertainties given by the EBMA models fitted with the data for the whole chart of nuclides (panel (a)), fitted for each isotopic chain (panel (b)), isotonic chain (panel (c)), and isobaric chain (panel (d)). The number of new data points included in the fit (n in Figure 4.7) is not necessarily 319 for the isotopic/isotonic/isobaric fits because at the edge of the chart of nuclides, often there are not enough data points in the isotopic/isotonic/isobaric chains and the posterior weights do not converge. Such data points are excluded from the fits. The size of the EBMA uncertainty is taken as the 68% highest (posterior) density interval ($\mathrm{HDI}_{.68}$), which is the narrowest 68% credible interval on the posterior distribution. If the distribution is a perfect normal distribution, 68% corresponds to the $\pm 1\sigma$ interval symmetric about the mean. To study how the observation distributes relatively to the $\mathrm{HDI}_{.68}$, we define δ, which represents an observed S_n value normalized by the size of $\mathrm{HDI}_{.68}$. Let h^{low} and h^{up} represents the lower and upper boundaries of the $\mathrm{HDI}_{.68}$, respectively,

$$\delta = \frac{S_n - h^{\mathrm{low}}}{h^{\mathrm{up}} - h^{\mathrm{low}}} - 0.5, \tag{4.8}$$

where 0.5 is subtracted to symmetrize the distribution around 0. Comparing the average sizes of the 68% intervals ($\overline{\mathrm{HDI}_{.68}}$), on average, the model fitted with the whole chart of nuclides (panel (a) of Figure 4.7) provides the most constrained size of the uncertainty of 0.48 MeV. On the other hand, the models fitted for each isotopic (panel (b)), isotonic (panel (c)), and isobaric (panel (d)) chain have larger credible intervals. This is most likely due to the fewer observation data points in each isotopic, isotonic, or isobaric chain compared to the data for the whole chart of nuclides. For the isotopic and isotonic fits (panels (c) and (d)), some data points around $\delta \sim 2$ can be seen, suggesting that the models optimized for isotopic/isotonic chains may be more sensitive to observations that do not follow the trend within the isotopic/isotonic chain. This means that the isotopic/isotonic models may be used for detecting anomalous masses or separation energies with respect to the trend within the isotopic/isotonic chain. The quantified uncertainty may also be used to estimate the probabilities of certain nuclei to be bound as in Refs [210, 217, 224], which will be addressed in future work.

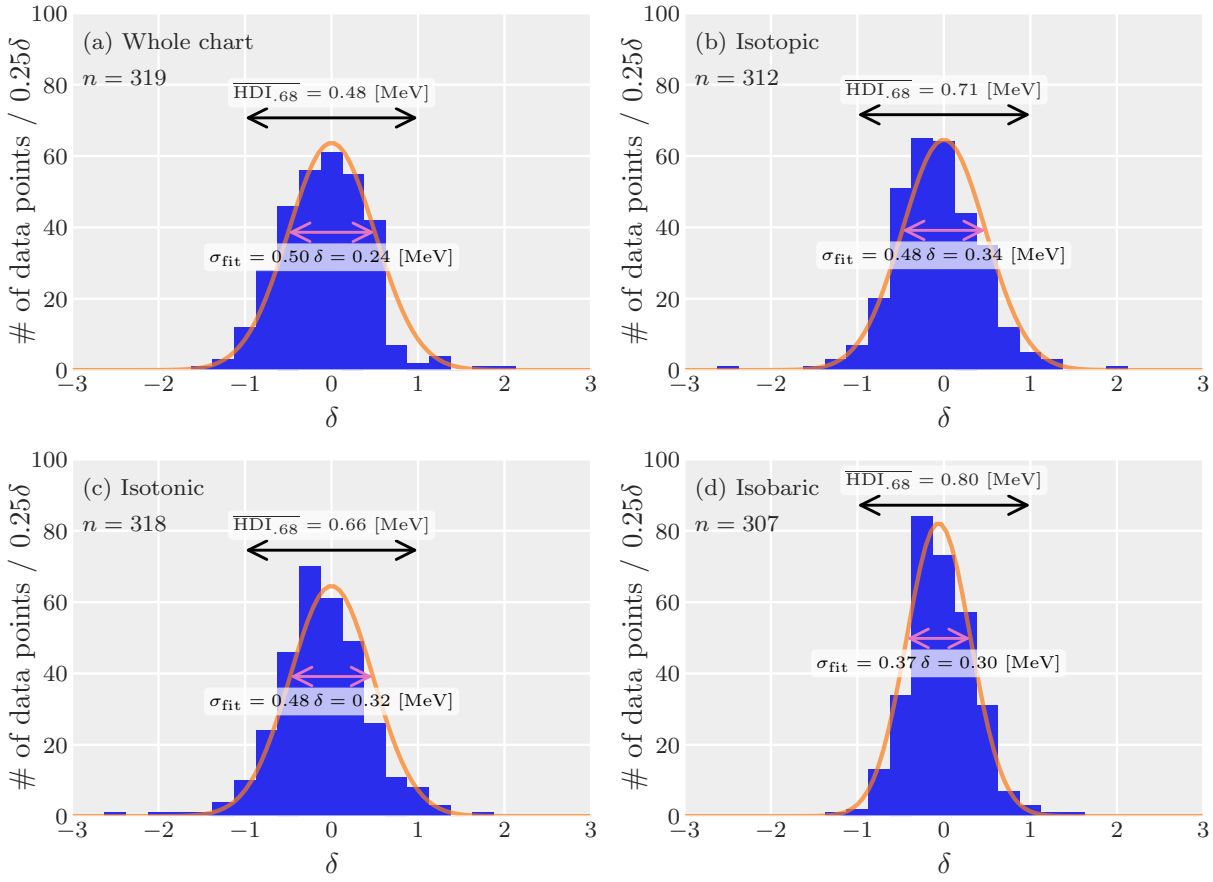

Figure 4.7: Distributions of the new data points in AME2020 compared to AME2003, with respect to the 68% HDIs predicted by the EBMA models fitted with the AME2003 data for (a) the whole chart of nuclides, (b) each isotopic chain, (c) each isotonic chain, and (d) each isobaric chain.

4.3 Conclusions

We have explored the possibility of quantifying the uncertainty of deterministic mass models using the EBMA method. The EBMA method models an ensemble of bias-corrected mass models as a mixture of normal distributions, whose parameters are estimated by MCMC using the No-U-Turn-Sampler (NUTS). The EBMA models have been constructed in four different ways of fitting, namely, the whole

chart of nuclides, each isotopic chain, each isotonic chain, and each isobaric chain.

In reproducing the observed one-neutron separation energies (S_n), in all cases, the maximum a posteriori (MAP) estimates of the EBMA models result in smaller root mean squared deviations from the AME2020 data than the best model in the ensemble, namely the WS4 model. While the EBMA model fitted for the whole chart of nuclides results in a larger σ_{RMS} value than the isotopic/isotonic/isobaric fit, it provides a more constrained and accurate uncertainty.

For all cases, the 68% HDIs estimated from AME2003 data contain roughly 95% of the new observations in AME2020. This suggests that the extrapolations of the S_n values provided by the current EBMA models based on the AME2003 data and the six deterministic theoretical mass models work well for the new data in AME2020. Furthermore, based on the distributions of the new AME2020 data with respect to the size of the 68% HDIs, we conclude that the EBMA method provides meaningful but conservative uncertainty estimates.

The advantage of the current method is its simplicity of the model. As opposed to the previous works [209, 210, 216–218], the current EBMA method does not require probabilistic machine learning models that quantify the uncertainties while correcting for the deviations of each model from the experimental values. Therefore, the EBMA method is applicable to various nuclear physics observables such as β-decay rates and possibly neutron capture rates.

Chapter 5

Variance-Based Sensitivity Study with Experimental Data

In this chapter, a proof-of-concept work of the variance-based sensitivity analysis method, which was introduced in Section 3.3 is presented. This study utilized newly measured β-decay half-lives ($T_{1/2}$) and β-delayed one-neutron emission probabilities (P_{1n}) by the BRIKEN collaboration [225], using the radioactive isotope beam produced at the RIKEN Nishina center in Japan. The BRIKEN detector array consists of 140 ^{3}He neutron counters and at the center of the array, a double-sided silicon strip detector array called AIDA is placed for the detection of beam implantation and β-particles from the radioactive decays. This chapter is based on our recent publication [93]. The experimental data analysis was performed by G. Kiss and A. Vitéz-Sveiczer (ATOMKI, Hungary), and my role was to perform an analysis regarding the astrophysical implications of the new experimental data in the context of the rapid neutron capture process (r-process), which is described in detail below.

In this experiment, $T_{1/2}$ and P_{1n} values of 28 neutron-rich rare-earth isotopes ($^{159–166}$Pm, $^{161–168}$Sm, $^{165–170}$Eu, and $^{167–172}$Gd) were measured. The isotopes were produced at the Radioactive Isotope Beam Factory (RIBF) at RIKEN Nishina Center by impinging a 345 MeV / nucleon ^{238}U primary beam with an intensity of 60 pnA onto a 5 mm-thick ^{9}Be target. The fragments of the primary beam were selected and identified by the BigRIPS fragment separator [226].

Out of the 28 half-lives, 9 half-lives were determined for the first time and all the P_{1n} values were newly determined. Figures 5.1 and 5.2 summarize the experimental results, compared to the previous experimental data and various theoretical predictions.

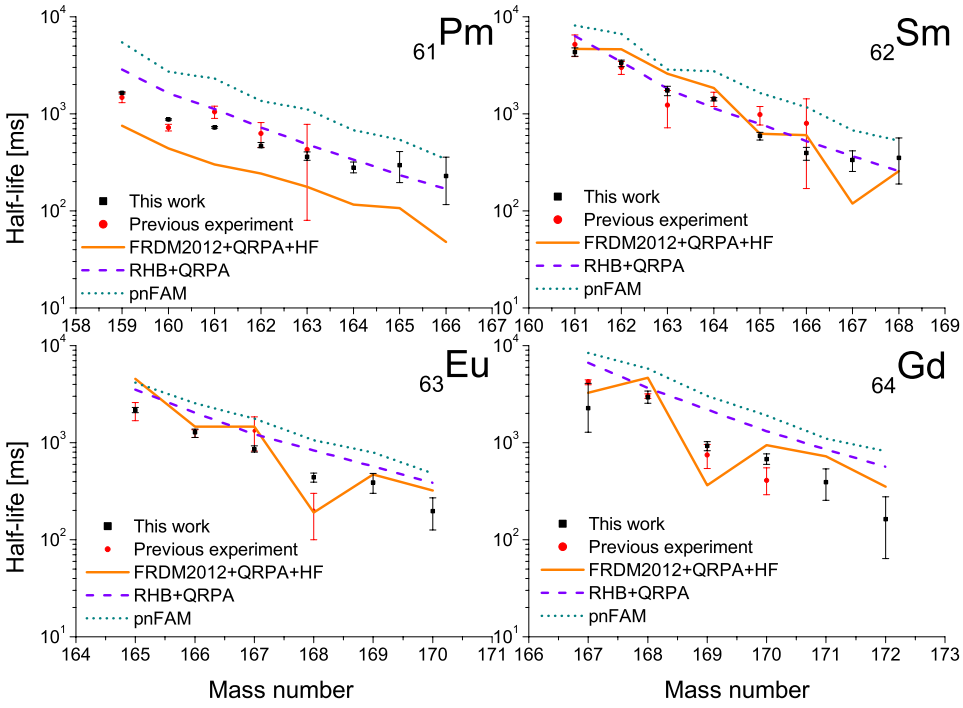

Figure 5.1: Half-lives determined in this experiment (black squares), in comparison to previous measurements (red circles) from Ref.[227], as well as theoretical predictions of different models: FRDM+QRPA+HF [98], RQRPA (labeled as RHB+QRPA) [100], and pnFAM [99]. Figure taken from our publication Ref. [93].

5.1 Astrophysical implication of the experimental results

5.1.1 Method

With respect to the current experimental values and their uncertainties, we perform an uncertainty quantification and a variance-based sensitivity analysis [180] (Sec-

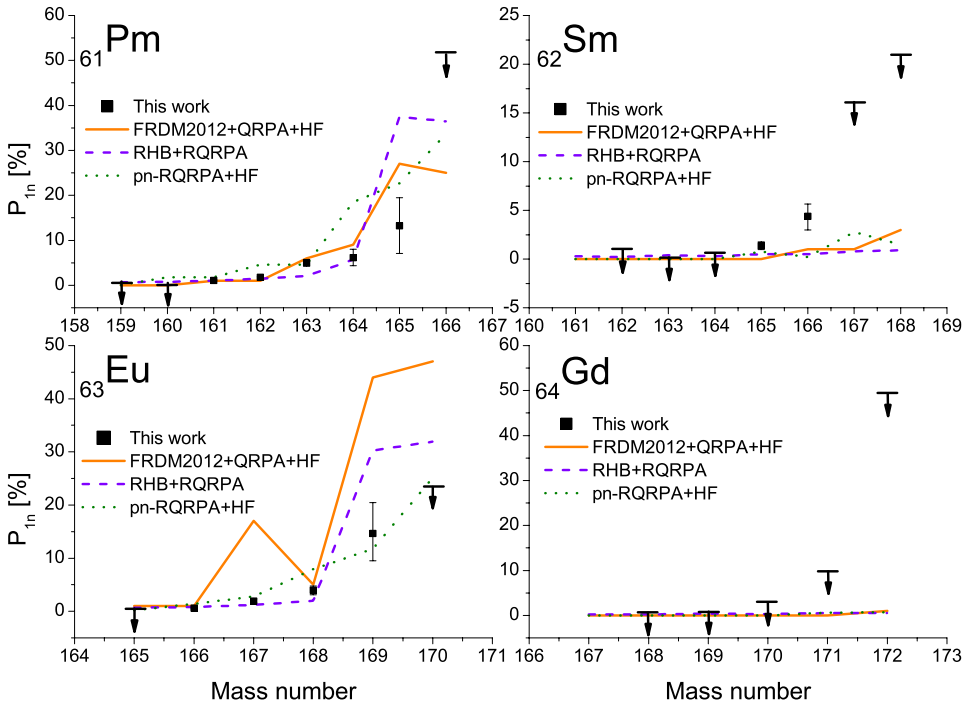

Figure 5.2: β-delayed one-neutron emission probabilities (P_{1n}) determined in this experiment (black squares), in comparison to theoretical predictions of different models: FRDM+QRPA+HF [98], RQRPA [100], and RQRPA+HF (labeled as pn-RQRPA+HF) [228]. Figure taken from our publication Ref. [93].

tion 3.3) of the calculated *r*-process abundance pattern. As discussed in detail below, by treating the physical quantities of interest, namely $T_{1/2}$ and P_{1n}, as variable inputs of the nuclear reaction network calculation, we can assess their influence on the calculated abundance patterns.

Uncertainty quantification

Uncertainty quantification reveals how the uncertainties of the nuclear observables collectively translate to the uncertainty of the calculated abundance pattern. This has been performed in various previous studies [82, 196, 229], mainly using theoretical values for a wide range of nuclides and focusing on the uncertainty of the overall abundance pattern.

Table 5.1. Half-lives ($T_{1/2}$) and β-delayed neutron emission probabilities (P_{1n}) measured in the present work. Table taken from our publication Ref. [93].

Isotope	$T_{1/2}$ [ms]	P_{1n} [%]	Isotope	$T_{1/2}$ [ms]	P_{1n} [%]
^{159}Pm	1648^{+43}_{-42}	≤ 0.6	^{167}Sm	334^{+83}_{-78}	≤ 16
^{160}Pm*	874^{+16}_{-12}	≤ 0.1	^{168}Sm	353^{+210}_{-164}	≤ 21
^{161}Pm	724^{+20}_{-12}	$1.09^{+0.11}_{-0.11}$	^{165}Eu*	2163^{+139}_{-120}	≤ 0.4
^{162}Pm	467^{+38}_{-18}	$1.79^{+0.19}_{-0.19}$	^{166}Eu	1277^{+100}_{-145}	$0.63^{+0.17}_{-0.17}$
^{163}Pm*	362^{+42}_{-30}	$5.00^{+0.73}_{-0.74}$	^{167}Eu	852^{+76}_{-54}	$1.95^{+0.38}_{-0.38}$
^{164}Pm	280^{+38}_{-33}	$6.18^{+1.80}_{-1.79}$	^{168}Eu	440^{+48}_{-47}	$3.95^{+0.83}_{-0.83}$
^{165}Pm	297^{+111}_{-101}	$13.26^{+6.23}_{-6.15}$	^{169}Eu	389^{+92}_{-88}	$14.62^{+5.82}_{-5.09}$
^{166}Pm	228^{+131}_{-112}	≤ 52	^{170}Eu	197^{+74}_{-71}	≤ 24
^{161}Sm	4349^{+425}_{-441}	≤ 2.7	^{167}Gd	2269^{+1817}_{-988}	≤ 12
^{162}Sm	3369^{+200}_{-303}	≤ 1.0	^{168}Gd	2947^{+467}_{-387}	≤ 0.8
^{163}Sm	1744^{+180}_{-204}	≤ 0.1	^{169}Gd*	926^{+95}_{-102}	≤ 0.7
^{164}Sm	1422^{+54}_{-59}	≤ 0.7	^{170}Gd	675^{+94}_{-75}	≤ 3
^{165}Sm	592^{+51}_{-55}	$1.36^{+0.40}_{-0.40}$	^{171}Gd	392^{+145}_{-136}	≤ 10
^{166}Sm	396^{+56}_{-63}	$4.38^{+1.25}_{-1.38}$	^{172}Gd	163^{+113}_{-99}	≤ 50

*The half-lives may include both ground-state and isomeric state decays.

In this work, we perform an uncertainty quantification with the experimental uncertainties of the half-lives and β-delayed one-neutron emission probabilities (P_{1n}), specifically focusing on the rare-earth peak (REP). This assesses the uncertainty of the abundance pattern induced by the current experimental uncertainties. If the size of the induced uncertainty is significantly larger than that of the measured solar abundance, it generally means that a more precise measurement is necessary within the set of nuclides. Since there are other sources of uncertainties from nuclear physics inputs, as well as astrophysical inputs, this uncertainty provides a lower limit.

We further compare these uncertainties of the calculated abundance patterns obtained from this experiment with the ones calculated with the previously mea-

sured β^--decay half-lives taken from [227], supplemented with the theoretical values from FRDM2012+QRPA [98] where previous experimental values do not exist. In this comparison, however, the uncertainties of P_{1n} from the current measurement have been used for both calculations. This is because it is difficult to assume reasonable uncertainties on theoretical values and, as will be shown in Section 5.1.2, the largest contribution to the uncertainties come from the half-lives. Therefore, this comparison quantifies the impact of the current measurements on the β^--decay half-lives.

Variance-based sensitivity analysis

The aim of this work is to apply the analysis method to the calculation of *r*-process abundances in the REP region, with the nuclear reaction network calculation being our model, $T_{1/2}$ and P_{1n} values from the current experiment being the inputs to be varied, and the abundances as a function of mass number in the REP region being the output of the model. In this study, we compute the first-order sensitivity indices $S^{(1)}$ (see Section 3.3), which account for the contributions of the uncertainty of individual variables to the uncertainty (variance) of the output. Since the sensitivity metric is based on the variance, i.e. the size of variation in the output in response to the variation of inputs, it does not rely on any assumption of the type of relationship, e.g. monotonic or linear. This allows for a straightforward interpretation of the sensitivity metric and identification of key nuclides and their nuclear properties that are responsible for the uncertainty of the calculated abundance pattern.

Furthermore, this framework allows for taking into account the dependence of the output on multiple input variables (second- or higher-order sensitivity indices), if they exist, which has not been addressed in the previous applied sensitivity analysis methods.

Generation of Monte Carlo samples

The values of the first-order sensitivity indices $S^{(1)}$ are estimated from the samples generated from Sobol quasi-random sequences. Sobol sequences are deterministic and designed to fill variable spaces more evenly and efficiently than ordinary pseudo-random sequences, which allow for a faster convergence of Monte Carlo

estimators (Eq. 3.16).

In both of the tasks of uncertainty quantification and sensitivity analysis, we use normal (Gaussian) distributions as distributions of most of the experimental values, where the mean values are equal to the nominal experimental values and the standard deviations are equal to the experimental uncertainties. In case of asymmetric uncertainties, the larger values have been used. Picking larger uncertainties to symmetrize the Gaussian distributions greatly simplifies the analysis while providing a conservative estimate of the uncertainty of the abundance pattern. When only upper limits are provided for P_{1n} values, it is assumed that they follow uniform distributions between 0 % and the upper limit values (accordingly, if we had lower limits the distribution would go from the lower limit value up to 100%).

For the uncertainties of the FRDM2012+QRPA half-lives used in the comparison described in Section 5.1.1, the size is assumed to be a factor of 10 around the predicted decay rates, following the uncertainty analysis in Ref. [82]. Any non-physical samples, such as negative half-lives or P_{1n} values, are discarded.

1000 samples of each of $T_{1/2}$ and P_{1n} value have been generated and used as inputs for nuclear reaction network calculations to obtain the nucleosynthesis yields of the *r*-process. The nuclear reaction network code `PRISM` [81] has been used for the calculations. We employ two astrophysical trajectories (temperature and density evolution): a dynamical ejecta from a neutron-star merger and a neutrino-driven wind. Both scenarios have been extensively studied as some of the most promising sites of the *r*-process.

The neutron-star merger trajectory is from Ref. [230] based on the simulations by Refs. [231] and [232], which takes into account the self-heating based on the FRDM2012 mass model [119].

The hot neutrino-driven wind trajectory (hereafter referred to as hot wind) corresponds to a hot *r*-process condition with low entropy of S=30 k_B, an initial electron fraction of $Y_e = 0.20$, and an expansion timescale of 70 ms based on Ref. [233], which is discussed in more detail in Ref. [82]. In the calculations, it is assumed that the emitted neutrons following the β-decays instantly thermalize and reach energies equal to the average energy of the neutrons in the environment, which is determined by the temperature of the astrophysical site.

Rates of β^--decays, β^--delayed neutron emission probabilities, neutron cap-

ture rates, fission rates and yields, etc., included in the network are identical to the ones in Ref. [234]. Whenever available, the theoretical rates and reaction Q-values have been replaced by the experimental values reported in AME2016 and Nubase2016 [235, 236]. For the nuclides measured in this study (Table 5.1), the current experimental values replaced any of the existing β^--decay rates ($T_{1/2}$) and β-delayed one-neutron emission probabilities (P_{1n}).

5.1.2 Results

Figure 5.3 shows the 2σ intervals of the abundances calculated with the samples drawn from the distributions discussed above, allowing variation of the half-lives and P_{1n} values of $^{159\text{-}166}$Pm, $^{161\text{-}168}$Sm, $^{165\text{-}170}$Eu, and $^{167\text{-}172}$Gd, for both of the employed astrophysical trajectories. Derived isotopic solar *r*-process abundances [26, 27] are also shown for reference. The averages of the abundance patterns have been scaled at $A = 157$ to match the calculation of the neutron star merger scenario. It is common practice to scale either calculated or solar abundance patterns to make a comparison, as they are both relative abundances. In this work, we choose to scale all the abundances to match $A = 157$, which is the base of the REP on the low mass side. This allows for a clear comparison of the height of the peaks of the calculated and the solar abundance patterns. While the calculations do not provide a great match to the solar abundances, the idea of this work is to learn about the dependence of calculated abundances in the REP region on the varied nuclear physics inputs, using some of the representative astrophysical conditions. In order to identify the cause of the significant discrepancies between the calculated abundance patterns and the solar abundance pattern, it is necessary to quantify the abundance uncertainties due to the assumptions and approximations in the astrophysical trajectories, in addition to the quantification of nuclear physics uncertainties.

Comparisons between the 2σ uncertainty bands calculated from the current experimental uncertainties (solid bands), and the uncertainty bands calculated with the previous experimental half-lives taken from [227], supplemented with the theoretical half-lives from FRDM2012+QRPA [98] (hatched band), are shown in Figure 5.4. As stated above, the uncertainty of the theoretical values are assumed to

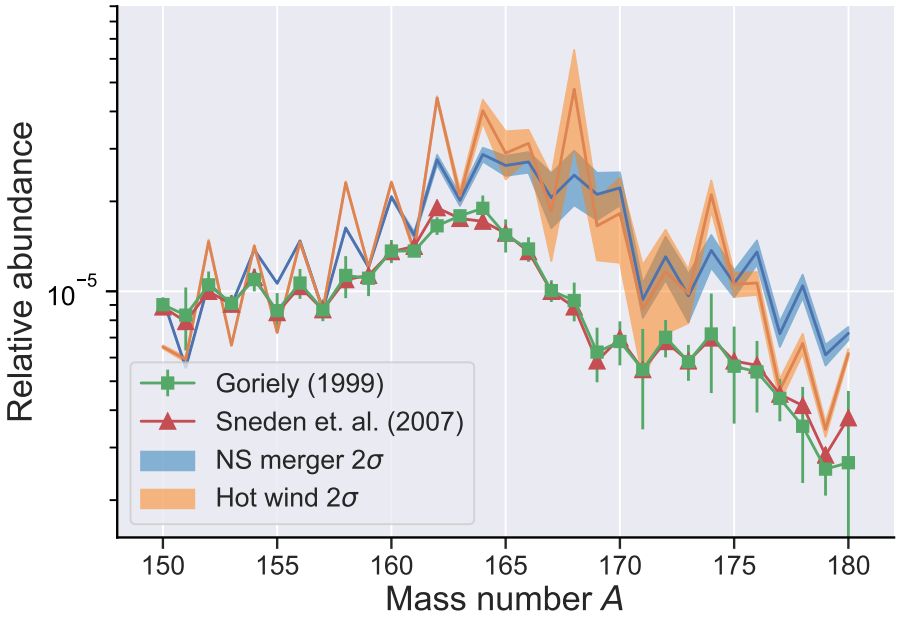

Figure 5.3: Calculated relative r-process abundance pattern for the neutron star merger scenario (blue line) and the hot wind scenario (orange). The band represents the 2σ interval propagated from the uncertainties of the current experimental results. The green boxes and red triangles indicate the derived relative solar r-process abundance pattern from [26] and [27]. The abundance patterns are scaled to match the mean value of the calculated abundance in the neutron star merger scenario at $A = 157$.

be a factor of 10, following the analysis by [82]. Both calculations use the current experimental uncertainties of the P_{1n} values for the β-delayed neutron emission probabilities, therefore, this comparison quantifies the impact of the current experimental half-lives.

In the neutron star merger scenario (Figure 5.4, top panel), the current experiment reduces the uncertainties for the mass numbers $A = 162$-176. The reduction is especially significant for $A = 162$-166 and 169-172. For the hot wind scenario (Figure 5.4, bottom panel), while the reduction in uncertainty is not as significant, the effect of the new data can be seen at $A = 165$-167 and $A = 169$-170.

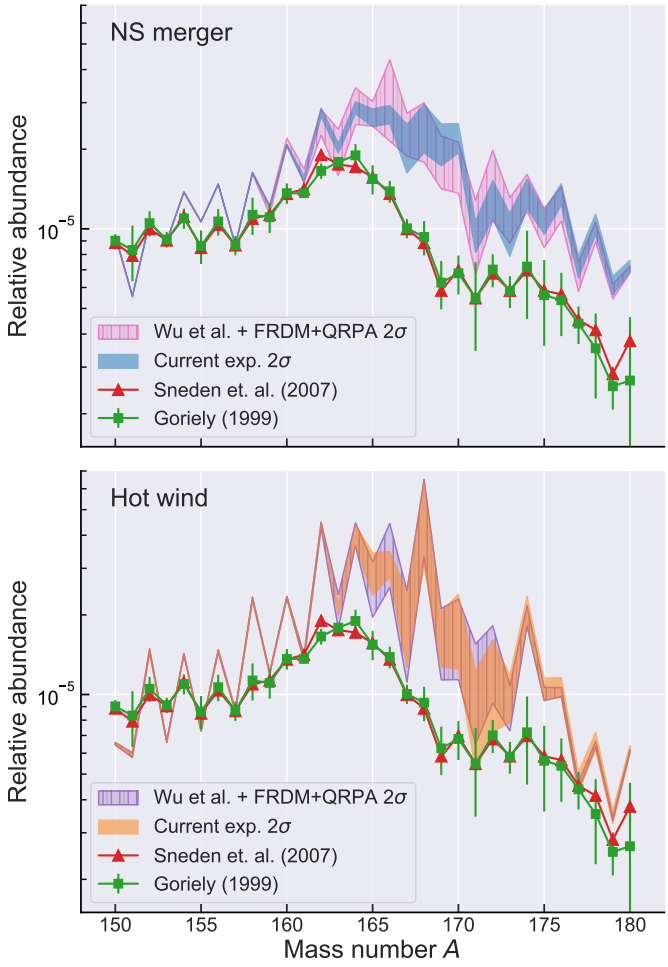

Figure 5.4: Comparisons of 2σ uncertainty bands of the calculated abundance patterns between the current experimental uncertainties of $T_{1/2}$ and P_{1n} values (solid bands), and the uncertainties of $T_{1/2}$ from Ref. [227] supplemented with the theoretical half-lives from FRDM2012+QRPA [98] where previous experimental values do not exist, with the uncertainties of P_{1n} values also from the current experiment (hatched bands). The top panel corresponds to the neutron star merger scenario and the bottom panel corresponds to the hot wind scenario. In both cases, all the abundance patterns are scaled to match the mean of the abundance in the neutron star merger scenario at $A = 157$. See text for details.

In both trajectories, Figures 5.3 and 5.4 show that the current experimental data still have significant effect on the uncertainties of the right (heavier) wing of the REP. Therefore, in our following analysis, we will mainly focus on the abundances of the mass numbers $A = 168$-173 and identify the sources of the uncertainty within the current set of experimental values. Since this analysis accounts only for the uncertainty of the current measurements, it should be noted that the size of uncertainty on the abundance pattern represents only a lower limit.

Figure 5.5 shows a snapshot the *r*-process path (at t= 0.732 s) of the neutron star merger scenario. The location of the isotopes of interest in the chart of nuclides relative to the path suggests that they are synthesized completely during freeze-out when the material decays back to stability. Therefore, analyzing how the decay properties such as half-lives and P_{1n} affect the abundances around the rare-earth peak through the variance-based sensitivity analysis may provide further insights into the freeze-out of the *r*-process. Since most of the analyses below will be common for both trajectories, i.e. neutron star merger and hot wind, we primarily focus on the neutron star merger scenario.

First order sensitivity indices

First-order sensitivity indices $S^{(1)}$ estimate the amount of contribution of each variable ($T_{1/2}$ and P_{1n} values, in this study) to the variance of the abundances. Tables 5.2 and 5.3 show the nuclides with the largest $S^{(1)}$ values, which means the largest contribution to the abundance variances, for $A = 168$-173, for the neutron star merger and hot wind trajectory, respectively.

From the Tables 5.2 and 5.3, it can be seen that samarium (Z=62) and gadolinium isotopes (Z=64) account for most of the abundance variances for these mass numbers in both astrophysical scenarios. For example, in the case of the neutron star merger scenario, based on the values of the sensitivity indices, it can be concluded that the half-lives of ^{168}Sm and ^{168}Gd account for 60.9 ($\pm$ 6.6)% and 24.3 ($\pm$ 4.6)% of the variance (propagated uncertainty) of the abundances at $A = 168$, respectively. The effect of the half-life of ^{168}Sm propagates also to the uncertainties of abundances for $A = 172$ and 173, which is discussed in more detail below. On the other hand, the influence of the P_{1n} values is relatively small in this astro-

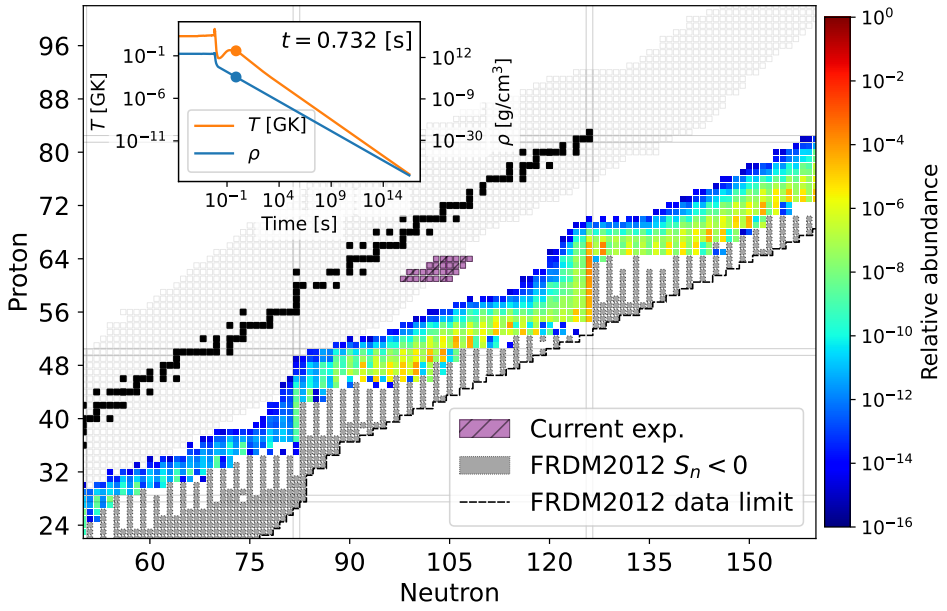

Figure 5.5: A snapshot of the *r*-process path in the neutron star merger scenario at t=0.732 s. The purple squares show the isotopes whose half-lives and β-delayed neutron emission probabilities have been measured in this work. The solid gray boxes indicate the isotopes with negative one-neutron separation energies ($S_{1n} < 0$) in the FRDM2012 mass model [119]. The inset shows the temperature and density profile of the trajectory.

physical scenario.

In the case of the hot wind scenario, on average, a larger contribution from the uncertainty of the P_{1n} values has been observed (Table 5.3). This is likely because the environment is less neutron-rich compared to the neutron star merger scenario [82], therefore, β-delayed neutron emissions become a more important source of neutrons, especially in the late time of the *r*-process.

As a general trend, the uncertainties of half-lives have the largest effect on the abundances for the corresponding mass number of the isotope, and a smaller effect for larger mass numbers. As one might expect, one-neutron emission probabilities (P_{1n}) can have influence on the abundance for the mass number $A-1$, where A is the mass number of the parent nucleus. For example the uncertainty of $P_{1n}(^{165}\mathrm{Pm})$

Table 5.2: Table of nuclear input variables that have a significant contribution to the uncertainties of the calculated abundances for $A = 168$-173 in the neutron star merger scenario. Columns 4–9 show the first-order sensitivity indices ($S^{(1)}$), which represent the contribution of individual variables to the abundance uncertainty, with 95 % confidence intervals. The maximum relative uncertainty (third column) is the ratio of the size of the larger one of upper or lower experimental uncertainty to the nominal value, in percentage. (100) indicates that the P_{1n} value only has an upper limit and the size of its relative uncertainty is 100%, according to the convention in [237]. Long dashes (—) indicate that the nominal value of $100 \times S^{(1)}$ is smaller than 0.5 [%]. Values larger than 10 [%] are highlighted in boldface.

		Max. relative	$100 \times S^{(1)}$ (95% C.I.) [%]					
Nuclide	Variable	uncertainty [%]	$A = 168$	169	170	171	172	173
^{165}Pm	$T_{1/2}$	37.4	1.9 (± 1.1)	3.2 (± 1.5)	4.9 (± 1.9)	2.7 (± 1.5)	0.8 (± 0.9)	—
^{166}Pm	$T_{1/2}$	57.5	—	—	0.5 (± 0.6)	0.7 (± 0.7)	—	—
^{166}Sm	$T_{1/2}$	15.9	—	1.7 (± 1.2)	4.8 (± 1.9)	3.8 (± 1.7)	1.5 (± 1.0)	0.8 (± 0.7)
^{167}Sm	$T_{1/2}$	24.9	0.6 (± 0.6)	—	—	1.1 (± 0.9)	0.9 (± 0.8)	0.6 (± 0.7)
^{168}Sm	$T_{1/2}$	59.5	**60.9** (± 6.6)	**55.1** (± 7.1)	**14.6** (± 4.4)	**32.6** (± 5.0)	**43.5** (± 5.5)	**41.6** (± 5.6)
^{168}Eu	$T_{1/2}$	10.9	0.5 (± 0.7)	—	—	—	—	—
^{169}Eu	$T_{1/2}$	23.7	—	3.6 (± 1.4)	—	—	0.9 (± 0.8)	0.7 (± 0.7)
^{170}Eu	$T_{1/2}$	37.6	—	—	0.6 (± 0.9)	—	—	—
^{167}Gd	$T_{1/2}$	80.1	6.1 (± 2.5)	**26.6** (± 4.3)	**34.2** (± 6.2)	**14.6** (± 3.9)	3.5 (± 1.8)	1.2 (± 1.1)
^{168}Gd	$T_{1/2}$	15.8	**24.3** (± 4.6)	8.3 (± 2.7)	8.1 (± 2.8)	2.2 (± 1.5)	—	—
^{169}Gd	$T_{1/2}$	11.0	—	0.8 (± 0.8)	—	—	—	—
^{170}Gd	$T_{1/2}$	13.9	—	—	**25.2** (± 4.7)	1.4 (± 1.2)	2.6 (± 1.4)	3.5 (± 1.7)
^{171}Gd	$T_{1/2}$	37.0	—	—	—	**20.5** (± 4.1)	4.6 (± 2.0)	1.0 (± 1.1)
^{172}Gd	$T_{1/2}$	69.3	—	—	—	3.6 (± 2.1)	**35.7** (± 5.1)	**49.3** (± 5.9)
^{165}Pm	P_{1n}	47.0	—	0.6 (± 0.6)	0.7 (± 0.5)	—	—	—
^{168}Sm	P_{1n}	(100)	—	—	—	0.8 (± 0.8)	0.6 (± 0.6)	—
^{169}Eu	P_{1n}	39.8	5.4 (± 2.1)	—	3.7 (± 1.6)	3.6 (± 1.7)	1.3 (± 1.0)	0.6 (± 0.7)
^{170}Eu	P_{1n}	(100)	—	0.5 (± 0.6)	—	—	—	—
^{172}Gd	P_{1n}	(100)	—	—	—	5.5 (± 2.0)	3.2 (± 1.5)	0.6 (± 0.7)
$S^{(1)}(T_{1/2})$ total:			94.9 (± 8.6)	100.1 (± 9.2)	93.9 (± 9.9)	84.0 (± 8.5)	95.1 (± 8.3)	99.7 (± 8.6)
$S^{(1)}(P_{1n})$ total:			5.9 (± 2.3)	1.1 (± 1.1)	5.6 (± 2.0)	11.0 (± 2.9)	5.7 (± 2.0)	2.0 (± 1.1)
$S^{(1)}$ total:			100.9 (± 8.9)	101.3 (± 9.2)	99.5 (± 10.1)	95.0 (± 9.0)	100.7 (± 8.6)	101.6 (± 8.6)

Table 5.3: Table of nuclear physics inputs that have a significant contribution to the uncertainties of calculated abundances for $A = 168$-173 in the hot wind scenario. Columns 4–9 show the first-order sensitivity indices ($S^{(1)}$), which represent the contribution of individual variables to the abundance uncertainty, with 95 % confidence intervals. The maximum relative uncertainty (third column) is the ratio of the size of the larger one of upper or lower experimental uncertainty to the nominal value, in percentage. (100) indicates that the P_{1n} value only has an upper limit and the size of its relative uncertainty is 100%, according to the convention in [237]. Long dashes (—) indicate that the nominal value of $100 \times S^{(1)}$ is smaller than 0.5 [%]. Values larger than 10 [%] are highlighted in boldface.

Nuclide	Variable	Max. relative uncertainty [%]	$100 \times S^{(1)}$ (95% C.I.) [%] $A = 168$	169	170	171	172	173
^{165}Pm	$T_{1/2}$	37.4	—	0.5 (± 0.6)	—	—	—	—
^{168}Sm	$T_{1/2}$	59.5	**96.1** (± 14.1)	**71.4** (± 7.0)	**95.2** (± 8.2)	**56.8** (± 7.1)	**44.6** (± 7.2)	**80.7** (± 13.3)
^{169}Eu	$T_{1/2}$	23.7	—	2.6 (± 1.4)	0.5 (± 0.6)	—	—	—
^{167}Gd	$T_{1/2}$	80.1	—	0.6 (± 0.6)	—	—	—	—
^{168}Gd	$T_{1/2}$	15.8	—	2.8 (± 1.5)	—	—	—	—
^{170}Gd	$T_{1/2}$	13.9	—	—	1.1 (± 0.9)	0.7 (± 0.8)	—	—
^{171}Gd	$T_{1/2}$	37.0	—	—	—	6.9 (± 2.6)	0.5 (± 0.7)	1.8 (± 1.2)
^{172}Gd	$T_{1/2}$	69.3	—	—	—	9.9 (± 3.2)	**53.3** (± 7.6)	**11.1** (± 3.3)
^{168}Sm	P_{1n}	(100)	2.0 (± 1.5)	3.5 (± 1.7)	0.5 (± 0.6)	—	—	—
^{169}Eu	P_{1n}	39.8	1.0 (± 0.9)	**10.8** (± 2.9)	0.5 (± 0.7)	—	—	—
^{170}Eu	P_{1n}	(100)	—	6.7 (± 2.3)	2.1 (± 1.2)	—	—	—
^{172}Gd	P_{1n}	(100)	—	—	—	**25.2** (± 4.6)	2.6 (± 1.7)	5.5 (± 2.1)
	$S^{(1)}(T_{1/2})$ total:		97.0 (± 14.1)	78.9 (± 7.4)	97.4 (± 8.3)	74.6 (± 8.2)	98.6 (± 10.5)	93.8 (± 13.7)
	$S^{(1)}(P_{1n})$ total:		3.0 (± 1.8)	21.5 (± 4.1)	3.7 (± 1.6)	25.9 (± 4.7)	2.8 (± 1.7)	5.6 (± 2.1)
	$S^{(1)}$ total:		100.0 (± 14.3)	100.5 (± 8.5)	101.1 (± 8.4)	100.5 (± 9.5)	101.3 (± 10.7)	99.4 (± 13.9)

accounts for 59.7% of the variance for $A = 164$ in the neutron star merger scenario.

Effect of the size of uncertainty

Maximum relative uncertainties of each input variable, which we define to be the size of the ratio of the larger one of upper or lower uncertainty to the nominal value, are also shown in the third column of Tables 5.2 and 5.3. The half-lives of ^{168}Sm, ^{167}Gd, and ^{172}Gd, which are some of the most influential in the neutron star merger scenario within the current data set, all have relatively large uncertainties of 60-80 %. However, a large relative uncertainty does not necessarily mean a large influence on the abundance uncertainty, as can be seen from the Tables 5.2 and 5.3. For example, the half-life of ^{172}Gd, whose relative uncertainty is larger than that of ^{168}Sm, has a similar or smaller contribution to the abundance at $A = 172$ and 173

than ^{168}Sm, which may also suggest that the mechanisms of the abundance pattern formation are different between inside the rare-earth peak (A = 155-170) and the heavy-mass wing of the peak ($A > 170$).

In order to investigate the effect of the size of input uncertainty on the sensitivity indices, we conduct a test under the neutron star merger condition. In this test, the size of uncertainty of the half-life of ^{168}Sm, which has been identified as one of the most influential inputs in both of the astrophysical trajectories, is artificially decreased to the relative uncertainty of 20 % from the current value of 59.5 %, while the mean value is kept the same. Note that this does not consider the possibility that the true mean value of the half-life can lie outside the currently considered 20 % relative uncertainty.

In the neutron star merger scenario, the half-life of ^{168}Sm has first order sensitivity indices of $S^{(1)}$= 60.9 %, 43.5 %, and 41.6 % for A = 168, 172, and 173, respectively (Table 5.2) when the relative uncertainty is 59.5 %. This means that if the half-life could be fixed without any uncertainty, we would be able to reduce the uncertainty of the calculated abundances by 60.9 %, 43.5 %, and 41.6 % for A = 168, 172, and 173, respectively. Since experimentally fixing the half-life or any other observables without uncertainty is impossible, therefore, it is worthwhile to investigate the effect of reducing the uncertainty.

Figure 5.6 shows a comparison between the calculated uncertainty (variance) of the abundance pattern using the original experimental uncertainty (light blue) and when the relative uncertainty of the half-life of ^{168}Sm is reduced to 20 % from 59.5 % (dark blue), in the neutron star merger scenario. As predicted from the sensitivity indices, the uncertainties have been significantly reduced for A = 168 and 169, and to a smaller degree for the larger mass numbers.

Table 5.4 shows the sensitivity indices with the reduced ^{168}Sm half-life uncertainty. While the value of $100 \times S^{(1)}$ of the half-life of ^{168}Sm for A = 168 decreased to 17.6 % from 60.9 % (Table 5.2), it is still a significant contribution to the output variances. It is also worth pointing out that the half-life of ^{168}Gd now has a larger contribution to the variance at A = 168, although its relative uncertainty is only 15.8 %. For the mass numbers A = 172 and 173, now the half-life of ^{172}Gd has the dominant contributions. At the same time, it can be seen from the table that the sensitivity has been more fragmented across the input variables compared to

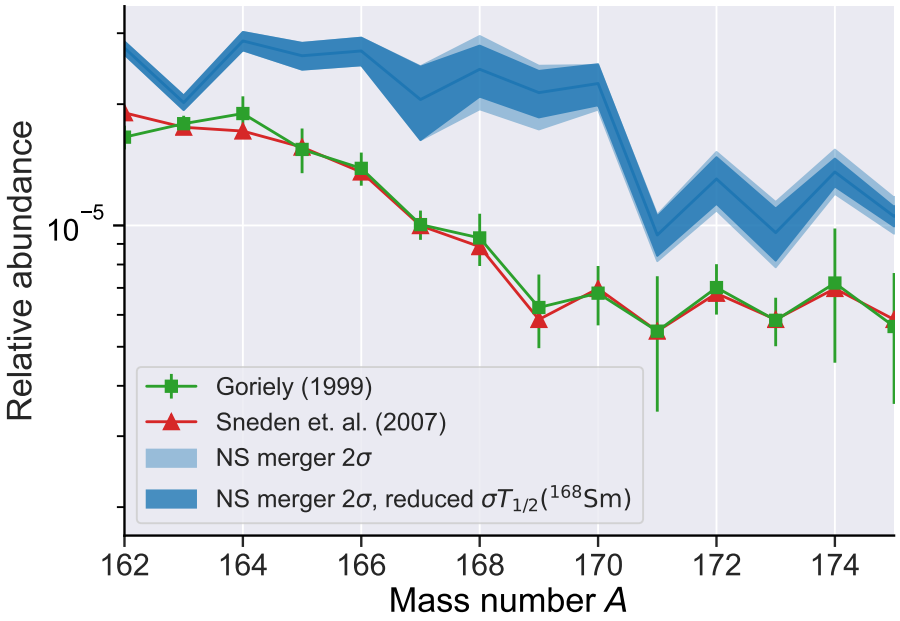

Figure 5.6: Calculated relative *r*-process abundance pattern for the neutron star merger scenario (blue line). The green and red boxes are the derived relative solar *r*-process abundance pattern from [26, 27]. The band in light blue color represents the 2σ interval propagated from the uncertainties of the original experimental results. The band in dark blue color represents the 2σ interval when the relative uncertainty of the half-life of ^{168}Sm is artificially reduced to 20 %, with the same mean value. All the abundance patterns are scaled to match the mean of the calculated abundances at $A = 157$ for the neutron star merger scenario.

the case shown in Table 5.2, elevating the relative sensitivity of the half-lives of the gadolinium isotopes.

Therefore, the half-lives of gadolinium isotopes may be considered significant sources of uncertainty of the calculated abundances in addition to the ^{168}Sm half-life, within the set of isotopes of interest in the current study.

Table 5.4: Table of nuclear input variables that have a significant contribution to the uncertainties of the calculated abundances for $A = 168$-173 for the neutron star merger scenario, with the relative uncertainty of the half-life of ^{168}Sm reduced to 20.0 %. Columns 4–8 show the first-order sensitivity indices ($S^{(1)}$), which represent the contribution of individual variables to the abundance uncertainty, with 95 % confidence intervals. The maximum relative uncertainty (third column) is the ratio of the size of the larger one of upper or lower experimental uncertainty to the nominal value, in percentage. (100) indicates that the P_{1n} value only has an upper limit and the size of its relative uncertainty is 100%, according to the convention in [237]. 20.0* for the half-life of ^{168}Sm denotes that the relative uncertainty is artificially reduced to 20.0 %. Long dashes (—) indicate that the nominal value of $100 \times S^{(1)}$ is smaller than 0.5 [%]. Values larger than 10 [%] are highlighted in boldface.

Nuclide	Variable	Max. relative uncertainty [%]	$100 \times S^{(1)}$ (95% C.I.) [%] $A = 168$	169	170	171	172	173
^{165}Pm	$T_{1/2}$	37.4	3.5 (± 1.5)	5.9 (± 2.0)	5.4 (± 2.2)	3.6 (± 1.8)	1.3 (± 1.1)	0.6 (± 0.7)
^{166}Pm	$T_{1/2}$	57.5	—	0.6 (± 0.4)	0.5 (± 0.6)	0.8 (± 0.7)	0.5 (± 0.6)	—
^{166}Sm	$T_{1/2}$	15.9	0.8 (± 0.7)	3.1 (± 1.6)	5.2 (± 2.0)	4.9 (± 2.0)	2.2 (± 1.2)	1.1 (± 0.9)
^{167}Sm	$T_{1/2}$	24.9	1.4 (± 1.0)	0.5 (± 0.6)	—	1.5 (± 1.1)	1.5 (± 1.1)	1.0 (± 0.9)
^{168}Sm	$T_{1/2}$	20.0*	**17.6** (± 3.8)	**13.0** (± 3.3)	1.0 (± 0.9)	9.4 (± 2.8)	12.1 (± 3.1)	9.7 (± 2.8)
^{167}Eu	$T_{1/2}$	8.9	—	0.5 (± 0.6)	—	—	—	—
^{169}Eu	$T_{1/2}$	23.7	—	7.1 (± 2.1)	—	0.6 (± 0.7)	1.4 (± 1.1)	1.0 (± 0.9)
^{170}Eu	$T_{1/2}$	37.6	—	—	0.8 (± 0.9)	—	—	—
^{167}Gd	$T_{1/2}$	80.1	**12.5** (± 4.3)	**50.8** (± 6.4)	**39.7** (± 6.8)	**19.8** (± 4.9)	5.4 (± 2.4)	1.8 (± 1.4)
^{168}Gd	$T_{1/2}$	15.8	**50.6** (± 6.9)	**16.0** (± 3.5)	9.5 (± 2.9)	3.0 (± 1.7)	0.6 (± 0.8)	—
^{169}Gd	$T_{1/2}$	11.0	—	1.6 (± 1.1)	—	—	—	—
^{170}Gd	$T_{1/2}$	13.9	—	—	**29.2** (± 5.2)	1.9 (± 1.4)	4.1 (± 1.8)	5.5 (± 2.1)
^{171}Gd	$T_{1/2}$	37.0	—	—	—	**28.0** (± 4.8)	7.0 (± 2.7)	1.5 (± 1.5)
^{172}Gd	$T_{1/2}$	69.3	—	—	—	4.8 (± 2.5)	**54.4** (± 6.1)	**73.8** (± 6.9)
^{165}Pm	P_{1n}	47.0	—	1.2 (± 0.8)	0.9 (± 0.5)	0.6 (± 0.4)	—	—
^{168}Sm	P_{1n}	(100)	—	—	0.6 (± 0.8)	1.4 (± 1.0)	1.1 (± 0.7)	0.7 (± 0.6)
^{169}Eu	P_{1n}	39.8	**11.3** (± 3.0)	—	4.5 (± 1.8)	5.0 (± 2.1)	2.1 (± 1.3)	1.0 (± 0.8)
^{172}Gd	P_{1n}	(100)	—	—	—	7.4 (± 2.4)	4.8 (± 1.8)	0.9 (± 0.8)

Impact of ^{168}Sm half-life during the freeze-out

By inspecting the samples generated for the variance-based sensitivity analysis, one may learn how the abundances depend on the nuclear physics inputs. We again take the half-life of ^{168}Sm as an example to demonstrate this, focusing on the neutron star merger scenario. Figure 5.7 shows the correlations of abundances for several mass numbers with the half-life of ^{168}Sm. Comparing the panels (a) and (b) of the figure, it can be seen that the abundance has a clear correlation with the

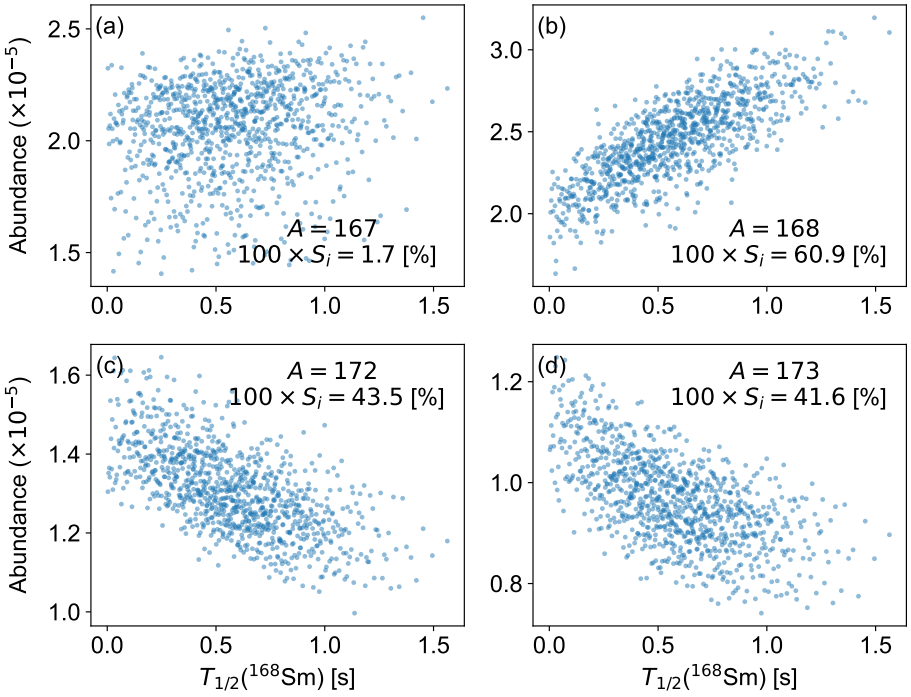

Figure 5.7: Correlation of abundances for $A = 167, 168, 172$, and 173 with the half-life of ^{168}Sm, as well as the first-order sensitivity indices ($S^{(1)}$), in the neutron star merger scenario. The correlation is sharp for a large sensitivity index (e.g. panel (b)), and the distribution is blurred for a small sensitivity index (e.g. panel (a)).

half-life when the sensitivity index is large.

The mechanism of this correlation becomes clear by analyzing the abundance flows due to β-decay and neutron capture. Figure 5.8 shows the relative isotopic abundances as functions of time (upper panels), the abundance flows (middle panels) and their total contributions, i.e. integrals of the abundance flows over time (lower panels) due to neutron capture and β-decay (labeled as (n,γ) and β^- in the figure, respectively) for ^{168}Sm, ^{168}Eu, and ^{168}Gd. They are separated into two cases: the sampled half-life of ^{168}Sm is larger than 0.55 [s] (Case 1) or smaller than 0.20 [s] (Case 2), for the neutron star merger scenario. The red dashed lines in the upper and middle panels represent the relative abundance of neutrons as a function

of time.

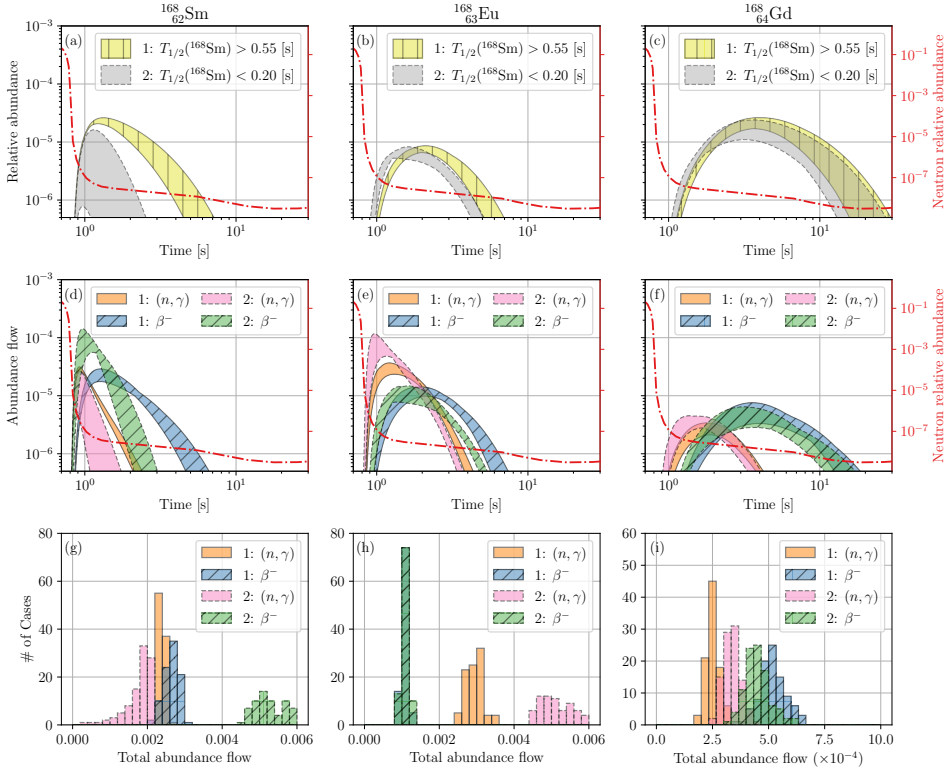

Figure 5.8: The top panels (a)–(c) show the abundance evolution of the isotopes ^{168}Sm, ^{168}Eu, and ^{168}Gd as functions of time in the neutron star merger scenario. The vertically hatched yellow bands correspond to the case where the half-life of ^{168}Sm is greater than 0.55 [s], and the solid gray bands correspond to the half-life smaller than 0.20 [s]. The middle panels (d)–(f) show the abundance flows of β^--decay (labeled as β^-, hatched with "//") and neutron capture (labeled as (n,γ), solid bands) as functions of time, for ^{168}Sm, ^{168}Eu, and ^{168}Gd, respectively, extracted from the generated samples. The red dash-dotted line is the neutron abundance as a function of time, which shows that these isotopes are synthesized after the neutron abundance significantly drops (freeze-out). The bottom panels (g)–(i) show the integrals of the abundance flows, i.e., the areas below the solid and dotted lines in the top panels. In all the panels, the solid outlines represent Case 1: $T_{1/2}(^{168}\mathrm{Sm}) > 0.55$ [s] and the dashed outlines represent Case 2: $T_{1/2}(^{168}\mathrm{Sm}) < 0.20$ [s].

It shows that these isotopes are synthesized after the neutron abundance drops significantly (freeze-out). The total contributions of the flows of (n,γ) and β^- are also shown in Figure 5.9 for the isotopic chains of Sm, Eu, and Gd up to mass number $A = 172$. In the figure, the width of the arrows correspond to the total amount of (n,γ) and β^--decay flows. Contributions from the reverse reaction of neutron capture (i.e. photodissociation) are negligible for all cases. Flows due to β-delayed neutron emission are also not shown since they only have contributions up to a few % on average, in this neutron star mergers scenario (Table 5.2).

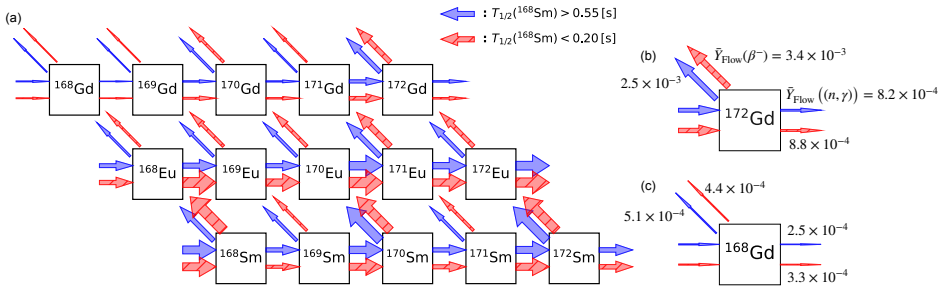

Figure 5.9: The arrows show the total abundance flows (the same quantity as the panels (g)–(i) in Figure 5.8), averaged over the generated samples, in the neutron star merger scenario. The red color corresponds to the case where the half-life of ^{168}Sm is smaller than 0.20 [s] and blue color larger than 0.55 [s]. The panels (b) and (c) focus on the flows from ^{172}Gd and ^{168}Gd, respectively. The propagated influence of the half-life of ^{168}Sm is visible, which results in affecting the final abundances.

Panel (d) of Figure 5.8 shows that the half-life of ^{168}Sm has a significant effect on the abundance flow from the isotope due to β-decay, while leaving the flow due to neutron capture relatively unaffected. The integrated abundance flow from ^{168}Sm shown in panel (g) indicates that the flow due to β-decay is increased when the half-life of ^{168}Sm is small. The increased amount of ^{168}Eu is quickly consumed by neutron captures, as shown in pink color in the panels (e) and (h). This, in turn, means that the longer half-life of ^{168}Sm provides a smaller amount of ^{168}Eu that can be converted to larger masses through neutron capture, therefore resulting in the smaller abundances for higher mass numbers, as shown in panels (c) and (d) of Figure 5.7. This effect can also be seen in panels (a) and (b) of Figure 5.9 and

explains why the abundances for $A = 172$ or 173 decrease as the half-life of ^{168}Sm increases.

This means that the half-life of ^{168}Sm has a significant influence on the neutron capture flow in the Eu isotopic chain, since ^{168}Sm is synthesized almost at the same time as the neutron abundance starts to drop (panel (a), Figure 5.8), meaning that some neutrons are still available for neutron capture, while photodissociation is no longer active. In panels (i) of Figure 5.8 and (b) of Figure 5.9, it can be seen that the flow from ^{168}Gd due to β-decay (hatched histogram in blue color) is larger when the half-life of ^{168}Sm is longer. This is because the longer half-life of ^{168}Sm extends the flow of β-decay of ^{168}Eu into the late time of the *r*-process where neutron capture is no longer significantly active, thus leaving more material at the same isobaric mass chain by avoiding being consumed by neutron capture.

Overall, the half-life of ^{168}Sm affects not only the flow of β-decay of ^{168}Sm but also the flow of neutron capture in the Eu isotopic chain up to mass number $A = 172$, 173 and heavier. This is also the case in the Gd isotopic chain, however, to a lesser extent. The balance between the β-decays and the neutron captures determine the final abundance pattern. Therefore, in order to properly account for the uncertainties of the abundance pattern from the nuclear physics inputs, uncertainties of neutron capture rates have to be included as well. This will be addressed in future work.

5.2 Summary and Conclusions

The β-decay properties of 28 neutron-rich Pm, Sm, Eu, and Gd isotopes were measured at RIKEN Nishina Center. Using the BRIKEN neutron counter array, β-delayed neutron emission probabilities were derived for the first time in this mass region. The existing half-life database has been significantly extended towards more neutron-rich species.

Nuclear reaction network calculations for the *r*-process employing a neutron star merger and a hot wind scenario have been carried out. Uncertainty quantification through the network calculations and comparison with the previous measurement supplemented with the assumed theoretical uncertainties showed that the currently measured half-lives reduce the propagated uncertainty (variance) of the

calculated abundances of the heavier wing of the REP at $A = 165$–173.

A new variance-based sensitivity analysis method has been introduced to identify nuclear physics inputs of importance within the current experimental uncertainties. The analysis has been performed using the characteristic abundance pattern of the rare-earth peak region.

The results of the analysis indicate that only a handful of variables account for nearly all the uncertainty (variance) of the abundance pattern. The results also suggest that the contributions of the uncertainty of the currently measured β-delayed one-neutron emission probabilities (P_{1n}) are significantly smaller than the half-lives in the case of neutron star mergers. The uncertainties of the P_{1n} values have larger contributions to the abundance pattern in the hot wind scenario, most likely due to the less neutron-rich environment compared to the neutron star merger scenario.

The half-life of ^{168}Sm, which has been measured for the first time in the current experiment, shows a significant influence on the high-mass tail of the rare-earth peak ($A = 168$-173) in both astrophysical scenarios. The calculated sensitivity indices and the numerical experiment on artificially reducing the uncertainty of the half-life of ^{168}Sm also indicate that the half-lives of $^{167\text{-}172}$Gd are significant sources of the uncertainty on the calculated abundance patterns. The analysis of the abundance flows due to neutron captures and β-decays in the neutron star merger scenario revealed that when the time scales of the β-decays of ^{168}Sm and neutron captures are comparable, the material can be transferred to higher masses such as $A = 172$ and 173 through chains of neutron capture mainly within the Eu isotopic chain.

The large sensitivity of the abundances to the half-life of ^{168}Sm is most likely due to ^{168}Sm being synthesized at the beginning of the *r*-process freeze-out when some neutrons are still available for neutron capture. This sensitivity analysis method thus provides a detailed view of how the flows of material in the *r*-process are affected by the nuclear physics inputs, in addition to identifying influential input variables.

In general, the observation that only a handful of nuclides contribute to the uncertainty of the abundance pattern is consistent with the fact that the *r*-process nuclear reaction network is a highly over-parameterized model. This means that the number of input variables (rates, initial condition, astrophysical trajectory etc.)

is larger than the number of output variables (abundances).

From a large number of input variables, the variance-based sensitivity analysis method can effectively identify influential variables, as demonstrated above, by focusing on localized features of the abundance pattern and a subset of input variables. This method relies on an assumption that the variables of interest have "reasonable" uncertainties. If experimental uncertainties are not available, which is currently the case for many of the nuclear observables of neutron-rich nuclei, theoretical uncertainties would be required to identify influential input variables.

The astrophysical analysis in this work does not concern theoretical β-decay properties of nuclei that are outside of the current experiment. However, as shown in Fig. 5.1, some systematic discrepancies between the observed β-decay half-lives and the theoretical predictions are present. In future work, it may be useful to calibrate the theoretical predictions based on the available experimental data and perform uncertainty quantification and a sensitivity analysis, in order to investigate the implication on the trend of β-decay properties by the experimental data, and its effect on calculated abundance patterns. Furthermore, it will be necessary to include more isotopes as well as more nuclear observables, such as masses and neutron capture rates to draw more general conclusions. Possible dependence between the observables, e.g. masses and β^--decay half-lives, should also be accounted for within the sensitivity analysis method.

Chapter 6

Emulation of a Nuclear Reaction Network Calculation Code

In studies of heavy element nucleosynthesis, especially the rapid neutron capture process (r-process), it is widely recognized that the properties of atomic nuclei, e.g. masses, shell structures, decay half-lives, and β-delayed neutron emission probabilities, affect the resulting abundance pattern of astrophysical nucleosynthesis events (Chapter 2).

A common method to investigate the impact of nuclear physics inputs on the r-process abundance pattern is to run a large number of nuclear reaction network calculations while varying the relevant inputs, e.g. β-decay half-lives ($T_{1/2}$), neutron separation energies (S_n), neutron capture rates, etc., following the design of the numerical experiment [82, 177–179, 196, 229]. The resulting calculated abundance patterns can then be used to obtain Monte Carlo estimates of the propagated uncertainty and sensitivity of the varied inputs. While the nuclear reaction network calculations can be run in parallel (in a so-called *embarrassingly parallel* scheme) for these purposes, the computational cost will still be significant. If one hopes to include a large number of inputs in the Monte Carlo studies, the required number of data points exponentially grows due to "the curse of dimensionality". In variance-based sensitivity analyses (e.g., Ref. [93]), the problem is even more challenging since a "sufficient" number of unique data points is required for each of the input variables of interest, and it is difficult, if not impossible, to know *a priori* how

many data points are sufficient.

Another class of statistical analysis using nuclear reaction network calculations is solving inverse problems, that is, to find the optimal values of nuclear physics inputs that best reproduce the observed solar *r*-process abundance pattern [238, 239]. Usually the Markov chain Monte Carlo method is used for minimizing the χ^2 likelihood . The nature of Markov chains forces sequential evaluation of nuclear reaction network calculations (Section 3.2). Since each of the calculations typically takes a few minutes, it would take an extremely long time before sufficient statistics is obtained. This will prevent us from verifying the convergence of the posterior distributions and detailed analysis of them. To avoid this problem, Refs. [238, 239] reduced the number of independent variables by parameterizing the correction to the mass surface to reproduce the detailed features of the rare earth peak. However, in this method, ambiguity around the probabilistic models still remains since such constraints on the parameters should ideally be embedded in the prior distributions.

Another way to tackle the problem is to reduce the computational cost. A common approach is to model the map between inputs and outputs with a flexible function such as Gaussian processes (GPs) [190, 191, 191, 192]. In this work, however, we aim to model the map between a large number of inputs and outputs, where GPs are not suitable. Therefore, we employ artificial neural networks which can work well with a large number of input and output dimensions [186]. We also introduce a way to quantify the uncertainty associated with the emulator, using a technique called "deep ensembles" (Section 3.4) [193].

6.1 Numerical Experiment

6.1.1 Emulating nuclear reaction network calculations with ANNs

The basic idea of this work is to emulate the variation in the calculated *r*-process nucleosynthesis yield when varying the nuclear physics inputs of nuclei of interest. The nucleosynthesis yields, or the final abundances as a function of the mass number A are calculated by performing nuclear reaction network calculations. As discussed in Section 1.3, performing a nuclear reaction network calculation amounts to solving an initial value problem of a system of ODEs. Therefore,

in our work, emulating the abundance calculations means modeling the function $f(\cdot)$ that takes some nuclear physics quantities as inputs and maps the initial abundance pattern a function of the mass number A, $\boldsymbol{Y_A}(t = t_0)$, to the final abundance pattern $\boldsymbol{Y_A}(t = t_f)$, where t_f is sufficiently larger than the timescale of the r-process nucleosynthesis, e.g. $t_f = 1$ Gyr.

In this work, we vary one-neutron separation energies (S_n) and the β-decay half-lives ($T_{1/2}$) of the 212 nuclei in the rare-earth region shown in Figure 6.1 and focus on their effect on the rare-earth peak (Section 2.1.2). Therefore, this model has 424 input variables in total. The neutron separation energies and half-lives are stored as a vector and we denote them as $\boldsymbol{S_n}$ and $\boldsymbol{T}_{1/2}$, respectively. They are sorted first by the proton number of the nuclei and then the number of neutrons. Therefore, the function $f(\cdot)$ we aim to model with an ANN is expressed as

$$\boldsymbol{Y_A}(t = t_f) = f(\boldsymbol{S_n}, \boldsymbol{T}_{1/2}). \tag{6.1}$$

Note that the function $f(\cdot)$ is conditional on the initial abundance pattern $Y_A(t = t_0)$, astrophysical trajectory, other nuclear physics inputs, and all the other inputs of the nuclear reaction network calculations.

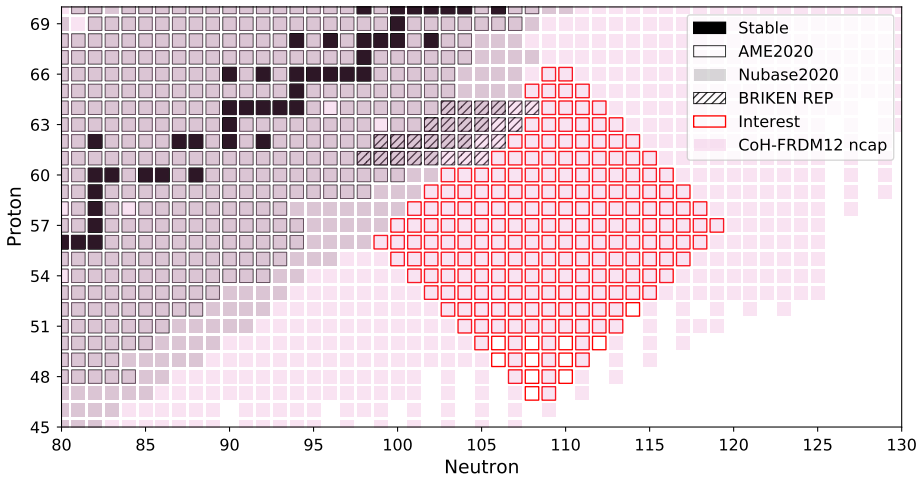

Figure 6.1: The red squares in the figure shows the nuclei included as input variables in the construction of the emulator. For comparison, the nuclei included in the experimental databases are shown too: AME2020 [10] and Nubase2020 [240]. Furthermore, the nuclei measured in Ref. [93] and discussed in Chapter 5 are shown as well with the label "BRIKEN REP". The "CoH+FRDM12 ncap" shows where theoretical neutron capture rates exist, which are identical to Refs. [82, 229].

6.1.2 Distributions of theoretical nuclear physics inputs

For the training of an ANN emulator, we first need to define how the input variables, namely each S_n and $T_{1/2}$, are distributed. If the distributions of the variables of interest are known from uncertainty quantification of theoretical models or from experimental uncertainties, they may be used. However, the FRDM2012 mass model [119] and the β-decay half-lives from FRDM+QRPA [98] used in this work currently do not have well-defined uncertainties associated with the theoretical predictions. In this work, we employ the distributions introduced in Ref. [82]. The size of the uncertainties for the S_n values are assumed to be ± 0.5 MeV, uniformly distributed around the FRDM values. For the β-decay half-lives ($T_{1/2}$), we assume that the decay rates ($\lambda = \ln(2)/T_{1/2}$) are distributed according to log-normal

distributions:

$$p(\lambda) = \frac{1}{\lambda\sqrt{2\pi}\sigma} \exp\left[-\frac{(\mu - \ln(\lambda))^2}{2\sigma^2}\right], \tag{6.2}$$

where μ is the theoretical rate from the FRDM+QRPA prediction and σ^2 is the variance of the underlying normal distribution, which is set to $\sigma = \ln(2)$ to allow for a factor of 10 in the decay rate variation.

Practically, however, if samples drawn from the distributions of the variables are directly used for training of the ANNs, it is likely that the tails of the distributions do not have a sufficient number of samples. This would be especially the case for the log-normal distributions introduced above. Therefore, we replace the log-normal distributions with log-uniform distributions that cover the $\pm 3\sigma$ intervals of the underlying normal distributions described by Equation 6.2:

$$p(\ln(\lambda)) = \begin{cases} \dfrac{1}{6\sigma} & \text{for } \ln(\lambda) \in [\mu - 3\sigma,\ \mu + 3\sigma], \\ 0 & \text{otherwise.} \end{cases} \tag{6.3}$$

Furthermore, to ensure that the samples evenly cover the entire variable space, we employ Sobol sequences, which are designed to efficiently fill up multidimensional variable spaces [180].

6.1.3 Data pre-processing and training of ANNs

In order for ANNs to achieve optimal performance, it is necessary to pre-process the input data [241]. The main strategy for input data pre-processing in this work is standardization, which makes the input samples distribute with zero means and standard deviations of one. For the β-decay rates λ, standardization is performed on a logarithmic scale. Standardization of one-neutron separation energies (S_n) is

performed on a linear scale:

$$\bar{p}(\lambda) = \frac{\ln(p(\lambda)) - \ln\left(\lambda^{\text{th}}\right)}{\sigma_{\lambda}^{\text{sample}}}, \tag{6.4}$$

$$\bar{p}(S_n) = \frac{p(S_n) - {S_n}^{\text{th}}}{\sigma_{S_n}^{\text{sample}}}, \tag{6.5}$$

where λ^{th} and ${S_n}^{\text{th}}$ denote the theoretical predictions of the FRDM+QRPA model [98] and the FRDM2012 mass model [119], respectively, $\sigma_{\lambda}^{\text{sample}}$ and $\sigma_{S_n}^{\text{sample}}$ are the standard deviations of the sample distributions of λ and S_n, respectively.

ANN models have been constructed using a deep learning application programming interface (API) written in PYTHON called KERAS [187], which is built on TENSORFLOW [188]. See the following section for the optimized architecture of the ANN models.

Training has been performed using a type of stochastic gradient descent method called AMSGRAD [242], which is a variant of one of the most commonly used methods called ADAM [243]. Training of our ANNs has been done with 300k samples, of which 280k have been used to optimize the weights in the ANN, and the remaining 20k samples have been used for validation to check the performance of the ANN for unseen input data. 10k samples have been additionally generated after the training is complete, to be used as a test data set for performance evaluation.

We consider two astrophysical scenarios: neutron star (NS) merger and hot neutrino-driven wind, identical to the ones used in Chapter 5. See Section 5.1.1 for details.

6.2 Results and Discussion

6.2.1 Optimized Emulator Architecture

Since no previous literature has been found on emulating nuclear reaction network calculations with ANNs to the best of our knowledge, we employ a systematic and automated way to explore optimal ANN architectures to establish the starting point for the architecture optimization. For this purpose, we use a method called neural

architecture search (NAS), implemented in a library called AUTOKERAS [244]. AUTOKERAS systematically varies the architecture and automatically records the best performing model. The architecture search is guided by Bayesian optimization, which allows for an efficient exploration of neural network architecture.

Based on the best performing architecture found by NAS, we further tune the architecture by hand, mostly by changing the number of layers, the number of filters in the convolutional layers, and the number of units in the fully connected layers.

The results of the neural network architecture optimization by NAS and by hand are summarized in Table 6.1. Our best performing architecture consists of convolutional layers followed by fully connected (dense) layers. In total, including the "Flatten" layer, which converts the stacked 2D data into a single vector, there are 7 layers. We have found that the use of convolutional layers is essential for achieving satisfactory performance. As discussed in Section 3.4, the advantage of using convolutional layers is that they can take into account the correlation between the properties of neighboring nuclei on the chart of nuclides. Rectified Linear Unit (ReLU) [189], which is one of the most widely used activation functions, has been used for all the layers except for the final layer. For the final layer, a linear activation was used to allow for unbounded output values. Since the output of this layer is simply a (weighted) linear combination of the output of the previous layer, it is called a "linear" layer. Note that the architecture does not have any physical interpretation. The performance of the ANN model is evaluated in detail in the following sections.

Table 6.1: Architecture of the neural network optimized by neural architecture search, then by hand. See Section 6.2.1 for discussion.

Layer No.	Layer type	Activation	Kernel size	Number of filters	Number of units
1	Convolutional	ReLU	3	128	—
2	Convolutional	ReLU	3	128	—
3	Convolutional	ReLU	3	128	—
4	Convolutional	ReLU	3	128	—
5	Flatten	—	—	—	—
6	Fully connected	ReLU	—	—	1024
7	Fully connected	Linear	—	—	31

6.2.2 Performance

Figures 6.2 and 6.3 show comparisons between the output of the original nuclear reaction network calculations (PRISM) [81] and the output of the ANN emulator, using the test data set consisting of 10k samples for the two astrophysical scenarios employed. Note that the figures only show 1k samples to avoid overcrowding the plot. Comparing the top two panels of the figures indicates that the ANN emulator captures the general trends of the calculated abundances very well. The bottom panel of the figures shows the deviations of the output of the emulator ($\log Y_A^{\rm emu}$) from the original (PRISM) calculations ($\log Y_A^{\rm orig}$), relative to the original calculations, defined as

$$y \equiv \frac{\log Y_A^{\rm emu} - \log Y_A^{\rm orig}}{\log Y_A^{\rm orig}}. \tag{6.6}$$

The σ_y shown in the bottom panel is the standard deviation of y, calculated using the entire 10k test samples. For the neutron star (NS) merger scenario, the standard deviation of the value y is $\sigma_y = 0.011$ (1.1%). For the hot neutrino-driven wind scenario, it is $\sigma = 0.02$ (2%). The larger variation of the abundances in the hot neutrino-driven wind scenario is most likely because the $(n,\ \gamma) \leftrightarrows (\gamma,\ n)$ equilibrium (see Section 2.1.1) is established, which is affected by the neutron

separation energies. In the NS merger scenario, due to its extremely neutron-rich condition, the path of the *r*-process nucleosynthesis is pushed all the way to the neutron dripline, therefore the final abundance pattern is less affected by the variation of the values of S_n.

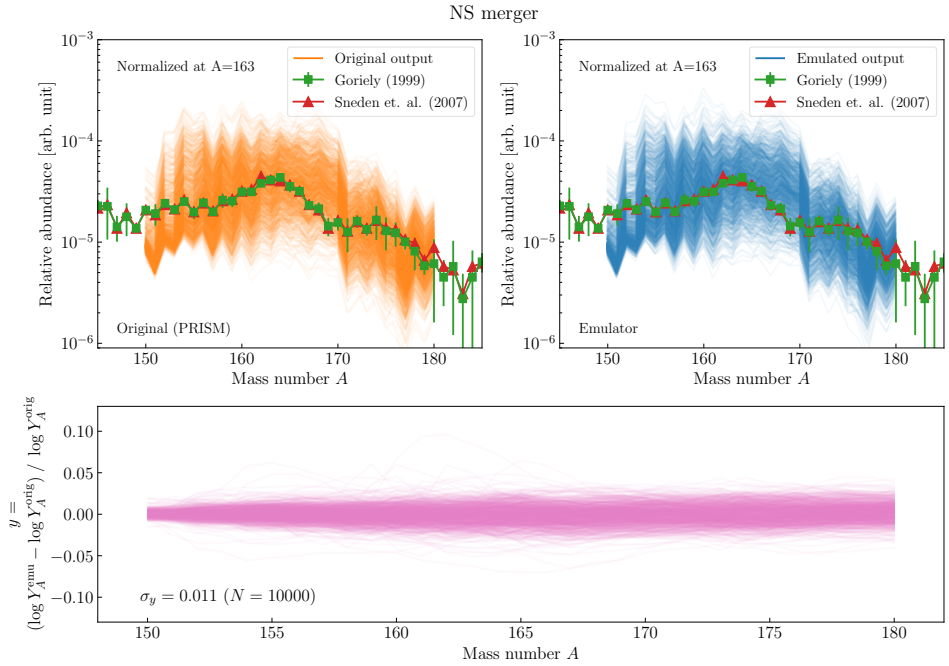

Figure 6.2: Comparison of the results between the original nuclear network calculation by PRISM [81] (top left panel) and our ANN emulator (top right panel), using the test data set, for the neutron star merger scenario, focusing on the rare-earth peak (REP) region $A = 150$–180. The bottom panel shows the deviations of the output of the emulator from the original (PRISM) calculations, relative to the original calculations. σ_y is their standard deviation, calculated using 10k samples. The plot only shows 1k samples to avoid overcrowding the plot. The solar abundance patterns are from Refs. [26] and [27], and they are scaled to match the average of the PRISM calculations at $A = 163$, which is the local abundance maximum in this mass region.

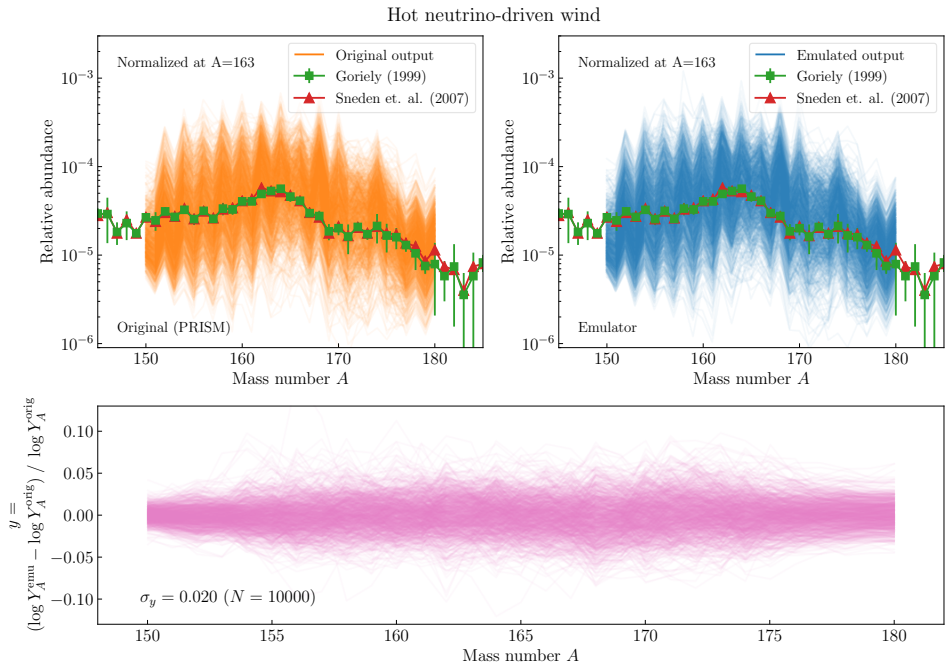

Figure 6.3: Same figure as Figure 6.2, but for the neutrino-driven hot wind scenario.

The main advantage of using emulators is their speed. While a nuclear reaction network calculation is not an extremely computationally expensive calculation, a single run of PRISM for the neutron star merger scenario takes roughly 400 seconds on an Intel Xeon CPU E5-2683 v4, available on the compute cluster Graham of the Digital Research Alliance of Canada. Multiple calculations can be run independently in parallel, but each run requires a compute core and about 4 GB of memory. On the other hand, obtaining a single abundance pattern from our emulator only takes about 0.1 second, using a NVIDIA Tesla P100 GPU, also available on GRAHAM. Furthermore, returning outputs for multiple input samples is also efficient—it takes about 1 second to predict 10k abundance patterns for the test data set.

6.2.3 Uncertainty Quantification

Uncertainty quantification of ANN predictions has been performed using deep ensembles (Section 3.4) [193]. The top panel of Figure 6.4 shows an example of the uncertainty quantification of an ANN prediction of an abundance pattern for the REP region (mass number $150 \leq A \leq 180$) drawn from the test dataset, compared to the original abundance pattern calculated with PRISM. It shows that the size of the uncertainty band is small enough to resolve the details of the abundance pattern. The bottom panel of the same figure shows how many of the 10k test samples of the original calculations are covered by the $\pm 1\sigma$ and $\pm 2\sigma$ uncertainty bands. Since our uncertainty is assumed to follow a Gaussian distribution, roughly 68 % and 95 % of the data points are expected to be covered by the $\pm 1\sigma$ and $\pm 2\sigma$ uncertainty bands, respectively. In our numerical experiment, it can be seen from the figure that about 80-94 % and 98-99 % of the original calculations are covered by the $\pm 1\sigma$ and $\pm 2\sigma$ uncertainty bands, respectively. This means that our uncertainty bands are somewhat under-confident (the size of uncertainty is overestimated); nevertheless, this simple method can provide meaningful estimates of prediction uncertainty.

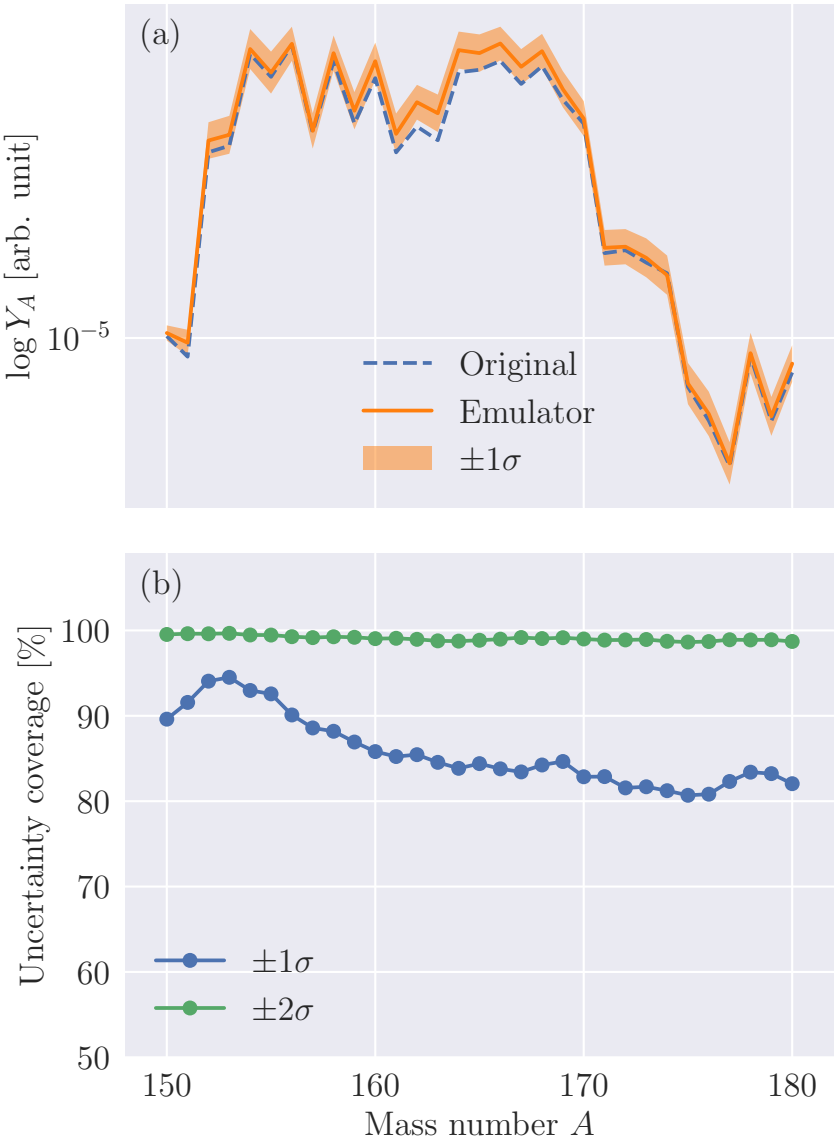

Figure 6.4: Panel (a) shows the emulated abundance pattern and the estimated $\pm 1\sigma$ uncertainty band of one of the test samples, compared to the original (PRISM) calculation. Panel (b) shows how many of the original calculations of the 10k test samples are covered by the $\pm 1\sigma$ and $\pm 2\sigma$ uncertainty bands, respectively.

6.3 Conclusions

In this chapter, we have shown that it is possible to emulate nuclear reaction network calculations with traditional ANNs consisting of convolutional layers followed by fully connected layers. Emulators have been constructed for two astrophysical scenarios: neutron star mergers and the hot neutrino-driven wind. The performance of the emulator has been demonstrated focusing on the rare-earth peak region ($150 \leq A \leq 180$), by treating the β-decay rates and the one-neutron separation energies of 212 isotopes as input variables for our ANN (in total 424 input variables). For both astrophysical trajectories, the ANNs can approximate the original calculations by the nuclear reaction network calculation code PRISM with less than 5 % deviation.

The dramatic speed-up of *r*-process abundance calculations, roughly by a factor of 4000, would enable large-scale statistical analyses that require performing nuclear reaction network calculations a large number of times, such as uncertainty quantification, Bayesian inverse problems, and variance-based sensitivity analyses.

Furthermore, we have demonstrated a simple method for estimating the predictive uncertainty of the ANN using deep ensembles, and the quality of the uncertainty estimation has been evaluated. The method provides conservative but meaningful uncertainty bands.

In future work, an exploration of more optimized ANN architectures possibly beyond the traditional ANNs will be performed. It would also be ideal to include many more isotopes and different types of nuclear reactions and decays, such as fission, and include more broader features of the *r*-process abundance patterns, such as second and third abundance peaks ($N = 82$ and $N = 126$, respectively).

Chapter 7

Summary and Outlook

7.1 Summary of the Contributions of This Thesis

The current thesis has discussed the applications of various statistical techniques to the problems relevant to the *r*-process nucleosynthesis. The following is a summary of the main contributions of this thesis.

The Ensemble Bayesian Model Averaging Method

In Chapter 4, the ensemble Bayesian model averaging (EBMA) method has been applied to the uncertainty quantification of neutron separation energies (S_n). The EBMA method determines the weights of the theoretical models in the ensemble based on the experimental data. The Bayesian posterior distributions of the EBMA model parameters are then used to quantify the uncertainty of S_n. The numerical experiments have shown that the EBMA method provides reasonable uncertainty estimates, although their sizes are somewhat overestimated.

The Variance-Based Sensitivity Analysis Method

In Chapter 5, the variance-based sensitivity analysis method has been demonstrated using the newly determined experimental uncertainties of the β-decay properties of neutron-rich nuclei in the rare-earth peak (REP) region. Influential β-decay properties that affect the calculated abundance patterns have been identified within

the set of nuclei of interest.

The "sensitivity" in this method is defined as the contribution of the input(s) to the variance (propagated uncertainty) of the output, therefore, the interpretation of the sensitivity is clearer in terms of the corresponding *r*-process observables, compared to previous work such as Refs. [82, 177–179]. Since this method relies on the Monte Carlo method, inspection of the Monte Carlo samples allows for detailed investigations of how certain nuclear physics inputs affect the observables such as abundance patterns, as demonstrated in Chapter 5.

Emulation of a Nuclear Reaction Network Calculation Code

In Chapter 6, it has been demonstrated that artificial neural networks are capable of emulating nuclear reaction network calculations that compute *r*-process abundance patterns, employing two astrophysical scenarios. This work also focused on the rare-earth peak (REP) region. The ANN models were able to reproduce well the changes in abundances corresponding to the variation in the β-decay half-lives and one-neutron separation energies (S_n) of 212 isotopes. Uncertainty quantification of the predictions of the ANN models was also demonstrated using the method called "deep-ensemble".

The benefit of emulators is their speed. For calculating a single abundance pattern, the emulator achieved a factor of 4000 improvement in speed, compared to one of the state-of-the-art nuclear reaction network calculation codes PRISM [81].

7.2 Outlook

The EBMA method is readily applicable to other nuclear physics observables that are relevant to the *r*-process nucleosynthesis, such as decay rates and temperature-dependent reaction rates. This would allow us to quantify the uncertainty in the calculations of the *r*-process observables (e.g., abundance patterns and kilonova lightcurves) coming from the choices of nuclear physics models. Effect of different nuclear physics models are usually studied by simply comparing the results of the calculations with different models, therefore, quantification of such uncertainties would be a meaningful development. Furthermore, as investigated in the literature using different approaches, as in Refs. [210, 217, 224], this method can also be used

to compute the probabilities that certain nuclei are predicted to be bound. In the future, it would be of interest to investigate the agreement of the results obtained from the EBMA method with the previous predictions.

The variance-based sensitivity analysis in the context of the *r*-process can be greatly generalized by using the nuclear reaction network calculation emulators. The fast emulators would allow for a significant increase in the number of inputs in the analysis, which would otherwise have been challenging, since it would require millions of runs of nuclear reaction network calculations. Although the variance-based method requires well-defined input uncertainties, which makes the sensitivity analyses of theoretical nuclear physics inputs difficult, since their uncertainties are not usually available, the EBMA method can overcome this problem. Therefore, combining the methods developed in the current thesis will open up a way to perform rigorous and detailed sensitivity analyses for a large number of neutron-rich nuclei.

Furthermore, the framework of the variance-based method allows for inclusion of correlated uncertainties, which will be useful for studying the effect of nuclear masses on the uncertainties of decay and reaction rates, for example. While propagation of mass uncertainties to the decay / reaction rates has been previously performed, they typically neglect the uncertainties of the decay / reaction rate calculations. Therefore, the variance-based method provides a suitable framework for improving this situation. Accurate sensitivity analyses are crucial for motivating and directing the experimental effort to measure key nuclear physics properties relevant to the *r*-process. This can help efficiently reduce the uncertainty in our understanding of the *r*-process nucleosynthesis originating from nuclear physics.

The fast nuclear reaction network calculation emulator would also benefit other studies such as "reverse-engineering" of nuclear physics properties from the *r*-process observables using the MCMC method, as in Refs. [238, 239]. Since the MCMC method generally requires numerous sequential runs of nuclear reaction network calculations, the impact of the speed-up by a factor of thousands will be particularly large.

With more multi-messenger observations of the *r*-process nucleosynthesis events (such as binary neutron star and neutron star-black hole mergers) in the future, applications of statistical methods can play an important role in analyzing the impli-

cations of the multi-messenger observations in terms of the physics of neutron-rich nuclei. For example, comprehensive and detailed sensitivity analyses of the nuclear physics inputs for the kilonova lightcurves would be of great interest. Furthermore, with fast emulators, it may become possible to constrain the properties of neutron-rich nuclei from the observations of kilonovae through statistical inference methods. Thus, this thesis contributes to laying the groundwork for the development of statistical tools that can be used for such analyses.

Statistical methods are appropriate tools for studying nuclear physics in the context of the *r*-process nucleosynthesis, considering that thousands of nuclei are involved in the process. They also provide convenient frameworks for uncertainty quantification, sensitivity analysis, and other inference tasks. However, the convenience of statistical methods could also result in flawed conclusions without understanding the assumptions and limitations of the method, as can be seen in some literature. Therefore, it will be important to carefully analyze and understand the foundation as well as the applicability of the methods.

Bibliography

[1] E. M. Burbidge, G. R. Burbidge, W. A. Fowler, and F. Hoyle. Synthesis of the elements in stars. *Rev. Mod. Phys.*, 29:547–650, 1957. doi:10.1103/RevModPhys.29.547. → pages 2, 5

[2] A. G. W. Cameron. Stellar evolution, nuclear astrophysics, and nucleogenesis. Technical Report CRL-41, Atomic Energy of Canada Ltd., 1957. → page 2

[3] K. Lodders. Solar system abundances and condensation temperatures of the elements. *The Astrophysical Journal*, 591(2):1220, 2003. doi:10.1086/375492. → page 4

[4] J. J. Cowan, C. Sneden, J. E. Lawler, A. Aprahamian, M. Wiescher, K. Langanke, G. Martínez-Pinedo, and F.-K. Thielemann. Origin of the heaviest elements: The rapid neutron-capture process. *Rev. Mod. Phys.*, 93: 015002, 2021. doi:10.1103/RevModPhys.93.015002. → pages xii, 4, 14, 16, 18, 19, 28, 31, 36

[5] D. Tytler, J. M. O'Meara, N. Suzuki, and D. Lubin. Review of big bang nucleosynthesis and primordial abundances. *Physica Scripta*, 2000(T85): 12, 2000. doi:10.1238/Physica.Topical.085a00012. → page 5

[6] R. H. Cyburt, B. D. Fields, K. A. Olive, and T.-H. Yeh. Big bang nucleosynthesis: Present status. *Rev. Mod. Phys.*, 88:015004, 2016. doi:10.1103/RevModPhys.88.015004. → page 5

[7] N. Prantzos. Production and evolution of li, be, and b isotopes in the galaxy. *Astronomy & Astrophysics*, 542:A67, 2012. doi:10.1051/0004-6361/201219043. → page 5

[8] C. Iliadis. *Nuclear physics of stars*. John Wiley & Sons, 2015. → pages 6, 7, 8, 9, 10, 28, 30

[9] T. Rauscher. *Essentials of Nucleosynthesis and Theoretical Nuclear Astrophysics*. 2514-3433. IOP Publishing, 2020. doi:10.1088/2514-3433/ab8737. → pages 6, 7, 8, 9, 10

[10] W. J. Huang, M. Wang, F. G. Kondev, G. Audi, and S. Naimi. The ame 2020 atomic mass evaluation (i). evaluation of input data, and adjustment procedures. *Chinese Physics C*, 45(3):030002, 2021. doi:10.1088/1674-1137/abddb0. → pages xi, xiii, xiv, 6, 37, 38, 41, 47, 51, 52, 55, 56, 57, 58, 83, 86, 88, 93, 94, 122

[11] D. Arnett. *Supernovae and nucleosynthesis: an investigation of the history of matter, from the big bang to the present*. Princeton University Press, 1996. → pages 6, 7, 8, 28

[12] D. D. Clayton. *Principles of stellar evolution and nucleosynthesis*. University of Chicago press, 1983. → page 7

[13] S. Höfner and H. Olofsson. Mass loss of stars on the asymptotic giant branch. *The Astronomy and Astrophysics Review*, 26(1):1, 2018. doi:10.1007/s00159-017-0106-5. → page 7

[14] H.-T. Janka. Explosion mechanisms of core-collapse supernovae. *Annual Review of Nuclear and Particle Science*, 62(1):407–451, 2012. doi:10.1146/annurev-nucl-102711-094901. → page 8

[15] A. Burrows and D. Vartanyan. Core-collapse supernova explosion theory. *Nature*, 589(7840):29–39, 2021. doi:10.1038/s41586-020-03059-w. → page 9

[16] M. Livio and P. Mazzali. On the progenitors of type ia supernovae. *Physics Reports*, 736:1–23, 2018. ISSN 0370-1573. doi:10.1016/j.physrep.2018.02.002. On the progenitors of Type Ia supernovae. → page 9

[17] K. Nomoto, K. Iwamoto, N. Nakasato, F.-K. Thielemann, F. Brachwitz, T. Tsujimoto, Y. Kubo, and N. Kishimoto. Nucleosynthesis in type ia supernovae. *Nuclear Physics A*, 621(1):467–476, 1997. doi:https://doi.org/10.1016/S0375-9474(97)00291-1. → page 9

[18] F.-K. Thielemann, J. Isern, A. Perego, and P. von Ballmoos. Nucleosynthesis in supernovae. *Space Science Reviews*, 214(3):62, 2018. doi:10.1007/s11214-018-0494-5. → page 9

[19] F. Käppeler, R. Gallino, S. Bisterzo, and Wako Aoki. The *s* process: Nuclear physics, stellar models, and observations. *Rev. Mod. Phys.*, 83: 157–193, Apr 2011. doi:10.1103/RevModPhys.83.157. → page 10

[20] F. Käppeler, R. Gallino, S. Bisterzo, and W. Aoki. The *s* process: Nuclear physics, stellar models, and observations. *Rev. Mod. Phys.*, 83:157–193, 2011. doi:10.1103/RevModPhys.83.157. → page 10

[21] K. Lodders, H. Palme, and H.-P. Gail. 4.4 abundances of the elements in the solar system. In *Solar System*, pages 712–770. Springer Berlin Heidelberg, 2009. doi:10.1007/978-3-540-88055-4_34. → page 11

[22] J. J. Cowan and W. K. Rose. Production of ^{14}c and neutrons in red giants. *The Astrophysical Journal*, 212:149–158, 1977. doi:10.1086/155030. → page 12

[23] F. Herwig, M. Pignatari, P. R. Woodward, D. H. Porter, G. Rockefeller, C. L. Fryer, M. Bennett, and R. Hirschi. Convective–reactive proton–^{12}c combustion in sakurai's object (v4334 sagittarii) and implications for the evolution and yields from the first generations of stars. *The Astrophysical Journal*, 727(2):89, 2011. doi:10.1088/0004-637X/727/2/89.

[24] L. Dardelet, C. Ritter, P. Prado, E. Heringer, C. Higgs, S. Sandalski, S. Jones, P. Denissenkov, K. Venn, M. Bertolli, M. Pignatari, P. Woodward, and F. Herwig. The i-process and cemp-r/s stars, 2015.

[25] P. A. Denissenkov, F. Herwig, U. Battino, C. Ritter, M. Pignatari, S. Jones, and B. Paxton. i-process nucleosynthesis and mass retention efficiency in he-shell flash evolution of rapidly accreting white dwarfs. *The Astrophysical Journal Letters*, 834(2):L10, 2017. doi:10.3847/2041-8213/834/2/L10. → page 12

[26] S. Goriely. Uncertainties in the solar system r-abundance distribution. *Astronomy and Astrophysics*, 342:881–891, 1999. → pages xii, 12, 13, 103, 104, 111, 127

[27] C. Sneden, J. J. Cowan, and R. Gallino. Neutron-capture elements in the early galaxy. *Annual Review of Astronomy and Astrophysics*, 46(1): 241–288, 2008. doi:10.1146/annurev.astro.46.060407.145207. → pages xii, 12, 13, 103, 104, 111, 127

[28] R. Surman, M. Mumpower, R. Sinclair, K. L. Jones, W. R. Hix, and G. C. McLaughlin. Sensitivity studies for the weak r process: neutron capture

rates. *AIP Advances*, 4(4):041008, 2014. doi:10.1063/1.4867191. → page 12

[29] S. Shibagaki, T. Kajino, G. J. Mathews, S. Chiba, S. Nishimura, and G. Lorusso. Relative contributions of the weak, main, and fission-recycling r-process. *The Astrophysical Journal*, 816(2):79, 2016. doi:10.3847/0004-637X/816/2/79. → page 12

[30] B. P. Abbott et al. GW170817: Observation of gravitational waves from a binary neutron star inspiral. *Phys. Rev. Lett.*, 119:161101, 2017. doi:10.1103/PhysRevLett.119.161101. → pages 15, 17

[31] B. P. Abbott et al. Multi-messenger observations of a binary neutron star merger*. *The Astrophysical Journal Letters*, 848(2):L12, 2017. doi:10.3847/2041-8213/aa91c9. → page 15

[32] V. A. Villar, J. Guillochon, E. Berger, B. D. Metzger, P. S. Cowperthwaite, M. Nicholl, K. D. Alexander, P. K. Blanchard, R. Chornock, T. Eftekhari, W. Fong, R. Margutti, and P. K. G. Williams. The combined ultraviolet, optical, and near-infrared light curves of the kilonova associated with the binary neutron star merger gw170817: Unified data set, analytic models, and physical implications. *The Astrophysical Journal Letters*, 851(1):L21, 2017. doi:10.3847/2041-8213/aa9c84. → page 15

[33] A. Perego, D. Radice, and S. Bernuzzi. At 2017gfo: An anisotropic and three-component kilonova counterpart of gw170817. *The Astrophysical Journal Letters*, 850(2):L37, 2017. doi:10.3847/2041-8213/aa9ab9. → page 15

[34] D. Kasen, B. Metzger, J. Barnes, E. Quataert, and E. Ramirez-Ruiz. Origin of the heavy elements in binary neutron-star mergers from a gravitational-wave event. *Nature*, 551(7678):80–84, 2017. doi:10.1038/nature24453. → page 15

[35] D. M. Siegel. r-process nucleosynthesis in gravitational-wave and other explosive astrophysical events. *Nature Reviews Physics*, 4(5):306–318, 2022. doi:10.1038/s42254-022-00439-1. → pages 15, 18

[36] M. B. Davies, W. Benz, T. Piran, and F. K. Thielemann. Merging Neutron Stars. I. Initial Results for Coalescence of Noncorotating Systems. *The Astrophysical journal*, 431:742, 1994. doi:10.1086/174525. → page 16

[37] M. Ruffert, H. T. Janka, and G. Schaefer. Coalescing neutron stars - a step towards physical models. I. Hydrodynamic evolution and gravitational-wave emission. *Astronomy and Astrophysics*, 311:532–566, 1996.

[38] S. Rosswog, M. Liebendörfer, F. K. Thielemann, M. B. Davies, W. Benz, and T. Piran. Mass ejection in neutron star mergers. *Astronomy and Astrophysics*, 341:499–526, 1999. → page 16

[39] C. Freiburghaus, S. Rosswog, and F.-K. Thielemann. r-process in neutron star mergers. *The Astrophysical Journal*, 525(2):L121, 1999. doi:10.1086/312343. → page 16

[40] M. Ruffert, H.-T. Janka, K. Takahashi, and G. Schaefer. Coalescing neutron stars - a step towards physical models. II. Neutrino emission, neutron tori, and gamma-ray bursts. *Astronomy and Astrophysics*, 319: 122–153, 1997. → page 16

[41] R. Oechslin, H.-T. Janka, and A. Marek. Relativistic neutron star merger simulations with non-zero temperature equations of state* - i. variation of binary parameters and equation of state. *Astronomy and Astrophysics*, 467 (2):395–409, 2007. doi:10.1051/0004-6361:20066682. → page 16

[42] K. Hotokezaka, K. Kiuchi, K. Kyutoku, H. Okawa, Y. Sekiguchi, M. Shibata, and K. Taniguchi. Mass ejection from the merger of binary neutron stars. *Phys. Rev. D*, 87:024001, 2013. doi:10.1103/PhysRevD.87.024001.

[43] K. Hotokezaka, K. Kyutoku, M. Tanaka, K. Kiuchi, Y. Sekiguchi, M. Shibata, and S. Wanajo. Progenitor models of the electromagnetic transient associated with the short gamma ray burst 130603B. *The Astrophysical Journal Letters*, 778(1):L16, 2013. doi:10.1088/2041-8205/778/1/L16. → page 16

[44] S. Goriely and G. Martínez Pinedo. The production of transuranium elements by the r-process nucleosynthesis. *Nuclear Physics A*, 944: 158–176, 2015. doi:https://doi.org/10.1016/j.nuclphysa.2015.07.020. → page 16

[45] J. Mendoza-Temis, M.-R. Wu, K. Langanke, G. Martínez-Pinedo, A. Bauswein, and H.-T. Janka. Nuclear robustness of the *r* process in neutron-star mergers. *Phys. Rev. C*, 92:055805, 2015. doi:10.1103/PhysRevC.92.055805. → pages 16, 31, 37, 76

[46] A. Perego, S. Bernuzzi, and D. Radice. Thermodynamics conditions of matter in neutron star mergers. *The European Physical Journal A*, 55(8): 124, 2019. doi:10.1140/epja/i2019-12810-7. → page 16

[47] S. Wanajo, Y. Sekiguchi, N. Nishimura, K. Kiuchi, K. Kyutoku, and M. Shibata. Production of all the r-process nuclides in the dynamical ejecta of neutron star mergers. *The Astrophysical Journal Letters*, 789(2):L39, 2014. doi:10.1088/2041-8205/789/2/L39. → page 16

[48] V. Kalogera and G. Baym. The maximum mass of a neutron star. *The Astrophysical Journal*, 470(1):L61, 1996. doi:10.1086/310296. → page 16

[49] K. Hotokezaka, K. Kiuchi, K. Kyutoku, T. Muranushi, Y. Sekiguchi, M. Shibata, and K. Taniguchi. Remnant massive neutron stars of binary neutron star mergers: Evolution process and gravitational waveform. *Phys. Rev. D*, 88:044026, 2013. doi:10.1103/PhysRevD.88.044026. → page 17

[50] L. Dessart, C. D. Ott, A. Burrows, S. Rosswog, and E. Livne. Neutrino signatures and the neutrino-driven wind in binary neutron star mergers. *The Astrophysical Journal*, 690(2):1681, 2008. doi:10.1088/0004-637X/690/2/1681. → page 17

[51] S. Rosswog, O. Korobkin, A. Arcones, F.-K. Thielemann, and T. Piran. The long-term evolution of neutron star merger remnants – I. The impact of r-process nucleosynthesis. *Monthly Notices of the Royal Astronomical Society*, 439(1):744–756, 2014. doi:10.1093/mnras/stt2502. → pages 17, 31

[52] A. Bauswein, S. Goriely, and H.-T. Janka. Systematics of dynamical mass ejection, nucleosynthesis, and radioactively powered electromagnetic signals from neutron-star mergers. *The Astrophysical Journal*, 773(1):78, 2013. doi:10.1088/0004-637X/773/1/78. → page 17

[53] B. D. Metzger and R. Fernández. Red or blue? A potential kilonova imprint of the delay until black hole formation following a neutron star merger. *Monthly Notices of the Royal Astronomical Society*, 441(4): 3444–3453, 2014. doi:10.1093/mnras/stu802. → page 17

[54] J. Lippuner, R. Fernández, L. F. Roberts, F. Foucart, D. Kasen, B. D. Metzger, and C. D. Ott. Signatures of hypermassive neutron star lifetimes on r-process nucleosynthesis in the disc ejecta from neutron star mergers. *Monthly Notices of the Royal Astronomical Society*, 472(1):904–918, 2017. doi:10.1093/mnras/stx1987.

[55] S. Fujibayashi, K. Kiuchi, N. Nishimura, Y. Sekiguchi, and M. Shibata. Mass ejection from the remnant of a binary neutron star merger: Viscous-radiation hydrodynamics study. *The Astrophysical Journal*, 860 (1):64, 2018. doi:10.3847/1538-4357/aabafd. → page 17

[56] O. Just, A. Bauswein, R. Ardevol Pulpillo, S. Goriely, and H.-T. Janka. Comprehensive nucleosynthesis analysis for ejecta of compact binary mergers. *Monthly Notices of the Royal Astronomical Society*, 448(1): 541–567, 2015. → page 17

[57] M.-R. Wu, R. Fernández, G. Martínez-Pinedo, and B. D. Metzger. Production of the entire range of r-process nuclides by black hole accretion disc outflows from neutron star mergers. *Monthly Notices of the Royal Astronomical Society*, 463(3):2323–2334, 2016. doi:10.1093/mnras/stw2156. → page 17

[58] F. Foucart. Black-hole–neutron-star mergers: Disk mass predictions. *Phys. Rev. D*, 86:124007, 2012. doi:10.1103/PhysRevD.86.124007. → page 17

[59] K. Kyutoku, K. Ioka, H. Okawa, M. Shibata, and K. Taniguchi. Dynamical mass ejection from black hole-neutron star binaries. *Phys. Rev. D*, 92: 044028, 2015. doi:10.1103/PhysRevD.92.044028. → page 17

[60] L. F. Roberts, G. Shen, V. Cirigliano, J. A. Pons, S. Reddy, and S. E. Woosley. Protoneutron star cooling with convection: The effect of the symmetry energy. *Phys. Rev. Lett.*, 108:061103, 2012. doi:10.1103/PhysRevLett.108.061103. → page 18

[61] T. Fischer, G. Guo, A. A. Dzhioev, G. Martínez-Pinedo, M.-R. Wu, A. Lohs, and Y.-Z. Qian. Neutrino signal from proto-neutron star evolution: Effects of opacities from charged-current–neutrino interactions and inverse neutron decay. *Phys. Rev. C*, 101:025804, 2020. doi:10.1103/PhysRevC.101.025804. → page 18

[62] J. M. LeBlanc and J. R. Wilson. A Numerical Example of the Collapse of a Rotating Magnetized Star. *The Astrophysical Journal*, 161:541, 1970. doi:10.1086/150558. → page 18

[63] C. Winteler, R. Käppeli, A. Perego, A. Arcones, N. Vasset, N. Nishimura, M. Liebendörfer, and F.-K. Thielemann. Magnetorotationally driven supernovae as the origin of early galaxy r-process elements? *The Astrophysical Journal Letters*, 750(1):L22, 2012. doi:10.1088/2041-8205/750/1/L22. → page 18

[64] N. Nishimura, T. Takiwaki, and F.-K. Thielemann. The r-process nucleosynthesis in the various jet-like explosions of magnetorotational core-collapse supernovae. *The Astrophysical Journal*, 810(2):109, 2015. doi:10.1088/0004-637X/810/2/109. → page 18

[65] N. Nishimura, H. Sawai, T. Takiwaki, S. Yamada, and F.-K. Thielemann. The intermediate r-process in core-collapse supernovae driven by the magneto-rotational instability. *The Astrophysical Journal Letters*, 836(2): L21, 2017. doi:10.3847/2041-8213/aa5dee.

[66] M. Reichert, M. Obergaulinger, M. Eichler, M. Á. Aloy, and A Arcones. Nucleosynthesis in magneto-rotational supernovae. *Monthly Notices of the Royal Astronomical Society*, 501(4):5733–5745, 2021. doi:10.1093/mnras/stab029. → page 18

[67] B. Wehmeyer, M. Pignatari, and F.-K. Thielemann. Galactic evolution of rapid neutron capture process abundances: the inhomogeneous approach. *Monthly Notices of the Royal Astronomical Society*, 452(2):1970–1981, 2015. doi:10.1093/mnras/stv1352. → page 18

[68] T. J. Galama, P. M. Vreeswijk, J. van Paradijs, C. Kouveliotou, T. Augusteijn, H. Böhnhardt, J. P. Brewer, V. Doublier, J. F. Gonzalez, B. Leibundgut, C. Lidman, O. R. Hainaut, F. Patat, J. Heise, J. in't Zand, K. Hurley, P. J. Groot, R. G. Strom, P. A. Mazzali, K. Iwamoto, K. Nomoto, H. Umeda, T. Nakamura, T. R. Young, T. Suzuki, T. Shigeyama, T. Koshut, M. Kippen, C. Robinson, P. de Wildt, R. A. M. J. Wijers, N. Tanvir, J. Greiner, E. Pian, E. Palazzi, F. Frontera, N. Masetti, L. Nicastro, M. Feroci, E. Costa, L. Piro, B. A. Peterson, C. Tinney, B. Boyle, R. Cannon, R. Stathakis, E. Sadler, M. C. Begam, and P. Ianna. An unusual supernova in the error box of the γ-ray burst of 25 april 1998. *Nature*, 395 (6703):670–672, 1998. doi:10.1038/27150. → page 18

[69] A. Janiuk, P. Sukova, and I. Palit. Accretion in a dynamical spacetime and the spinning up of the black hole in the gamma-ray burst central engine. *The Astrophysical Journal*, 868(1):68, 2018. doi:10.3847/1538-4357/aae83f. → page 19

[70] A. M. Beloborodov. Nuclear composition of gamma-ray burst fireballs. *The Astrophysical Journal*, 588(2):931, 2003. doi:10.1086/374217. → page 19

[71] D. M. Siegel and B. D. Metzger. Three-dimensional general-relativistic magnetohydrodynamic simulations of remnant accretion disks from

neutron star mergers: Outflows and *r*-process nucleosynthesis. *Phys. Rev. Lett.*, 119:231102, 2017. doi:10.1103/PhysRevLett.119.231102. → page 19

[72] D. M. Siegel, J. Barnes, and B. D. Metzger. Collapsars as a major source of r-process elements. *Nature*, 569(7755):241–244, 2019. doi:10.1038/s41586-019-1136-0. → page 19

[73] J. Lippuner and L. F. Roberts. Skynet: A modular nuclear reaction network library. *The Astrophysical Journal Supplement Series*, 233(2):18, 2017. doi:10.3847/1538-4365/aa94cb. → page 21

[74] W. R. Hix and F.-K. Thielemann. Computational methods for nucleosynthesis and nuclear energy generation. *Journal of Computational and Applied Mathematics*, 109(1):321–351, 1999. doi:https://doi.org/10.1016/S0377-0427(99)00163-6. → page 22

[75] W. R. Hix and B. S. Meyer. Thermonuclear kinetics in astrophysics. *Nuclear Physics A*, 777:188–207, 2006. doi:https://doi.org/10.1016/j.nuclphysa.2004.10.009. Special Isseu on Nuclear Astrophysics.

[76] C. Winteler. *Light element production in the big bang and the synthesis of heavy elements in 3D MHD jets from core-collapse supernovae*. PhD thesis, University of Basel, Faculty of Science, 2013.

[77] P. Virally. A modern nuclear reaction network solver. University of Waterloo Co-op term report, 2021. → pages xii, 22, 24, 25, 26

[78] O. Schenk and K. Gärtner. Solving unsymmetric sparse systems of linear equations with pardiso. *Future Generation Computer Systems*, 20(3): 475–487, 2004. doi:https://doi.org/10.1016/j.future.2003.07.011. → page 22

[79] J. Bezanson, A. Edelman, S. Karpinski, and V. B. Shah. Julia: A fresh approach to numerical computing. *SIAM Review*, 59(1):65–98, 2017. doi:10.1137/141000671. → page 22

[80] Y. Saito and P. Virally. Nuclearreactionnetwork.jl. https://github.com/YukiyaSaito/NuclearReactionNetwork.jl, 2021. → pages xii, 22, 24, 25, 26

[81] M. R. Mumpower, T. Kawano, T. M. Sprouse, N. Vassh, E. M. Holmbeck, R. Surman, and P. Möller. β-delayed fission in r-process nucleosynthesis. *The Astrophysical Journal*, 869(1):14, 2018. doi:10.3847/1538-4357/aaeaca. → pages xv, 22, 24, 25, 34, 102, 126, 127, 133

[82] M. R. Mumpower, R. Surman, G. C. McLaughlin, and A. Aprahamian. The impact of individual nuclear properties on r-process nucleosynthesis. *Progress in Particle and Nuclear Physics*, 86:86–126, 2016. ISSN 0146-6410. doi:https://doi.org/10.1016/j.ppnp.2015.09.001. → pages 25, 67, 76, 99, 102, 104, 107, 119, 122, 133

[83] O. Korobkin, S. Rosswog, A. Arcones, and C. Winteler. On the astrophysical robustness of the neutron star merger r-process. *Monthly Notices of the Royal Astronomical Society*, 426(3):1940–1949, 2012. doi:10.1111/j.1365-2966.2012.21859.x. → page 31

[84] S. Goriely. The fundamental role of fission during r-process nucleosynthesis in neutron star mergers. *The European Physical Journal A*, 51(2):22, 2015. doi:10.1140/epja/i2015-15022-3. → page 31

[85] R. Surman, J. Engel, J. R. Bennett, and B. S. Meyer. Source of the rare-earth element peak in *r*-process nucleosynthesis. *Phys. Rev. Lett.*, 79: 1809–1812, 1997. doi:10.1103/PhysRevLett.79.1809. → page 32

[86] M. R. Mumpower, G. C. McLaughlin, and R. Surman. Formation of the rare-earth peak: Gaining insight into late-time *r*-process dynamics. *Phys. Rev. C*, 85:045801, 2012. doi:10.1103/PhysRevC.85.045801. → page 32

[87] M. R. Mumpower, G. C. McLaughlin, and R. Surman. The rare earth peak: An overlooked r-process diagnostic. *The Astrophysical Journal*, 752(2): 117, 2012. doi:10.1088/0004-637X/752/2/117.

[88] M. R. Mumpower, G. C. McLaughlin, and R. Surman. Influence of neutron capture rates in the rare earth region on the *r*-process abundance pattern. *Phys. Rev. C*, 86:035803, 2012. doi:10.1103/PhysRevC.86.035803. → page 32

[89] I. V. Panov, I. Yu. Korneev, and F. K. Thielemann. The r-process in the region of transuranium elements and the contribution of fission products to the nucleosynthesis of nuclei with a $\leq$130. *Astronomy Letters*, 34(3): 189–197, 2008. doi:10.1134/S1063773708030067. → page 32

[90] S. Goriely, J.-L. Sida, J.-F. Lemaître, S. Panebianco, N. Dubray, S. Hilaire, A. Bauswein, and H.-T. Janka. New fission fragment distributions and *r*-process origin of the rare-earth elements. *Phys. Rev. Lett.*, 111:242502, 2013. doi:10.1103/PhysRevLett.111.242502.

[91] M. Eichler, A. Arcones, A. Kelic, O. Korobkin, K. Langanke, T. Marketin, G. Martinez-Pinedo, I. Panov, T. Rauscher, S. Rosswog, C. Winteler, N. T. Zinner, and F.-K. Thielemann. The role of fission in neutron star mergers and its impact on the r-process peaks. *The Astrophysical Journal*, 808(1): 30, 2015. doi:10.1088/0004-637X/808/1/30. → page 32

[92] A. Arcones and G. Martínez-Pinedo. Dynamical r-process studies within the neutrino-driven wind scenario and its sensitivity to the nuclear physics input. *Physical Review C*, 83:045809, 2011. doi:10.1103/PhysRevC.83.045809. → page 32

[93] G. G. Kiss, A. Vitéz-Sveiczer, Y. Saito, A. Tarifeño-Saldivia, M. Pallas, J. L. Tain, I. Dillmann, J. Agramunt, A. Algora, C. Domingo-Pardo, A. Estrade, C. Appleton, J. M. Allmond, P. Aguilera, H. Baba, N. T. Brewer, C. Bruno, R. Caballero-Folch, F. Calvino, P. J. Coleman-Smith, G. Cortes, T. Davinson, N. Fukuda, Z. Ge, S. Go, C. J. Griffin, R. K. Grzywacz, O. Hall, A. Horváth, J. Ha, L. J. Harkness-Brennan, T. Isobe, D. Kahl, T. T. King, A. Korgul, S. Kovács, R. Krücken, S. Kubono, M. Labiche, J. Liu, J. Liang, M. Madurga, K. Miernik, F. Molina, A. I. Morales, M. R. Mumpower, E. Nacher, A. Navarro, N. Nepal, S. Nishimura, M. Piersa-Siłkowska, V. Phong, B. C. Rasco, B. Rubio, K. P. Rykaczewski, J. Romero-Barrientos, H. Sakurai, L. Sexton, Y. Shimizu, M. Singh, T. Sprouse, T. Sumikama, R. Surman, H. Suzuki, T. N. Szegedi, H. Takeda, A. Tolosa, K. Wang, M. Wolinska-Cichocka, P. Woods, R. Yokoyama, and Z. Xu. Measuring the β-decay Properties of Neutron-rich Exotic Pm, Sm, Eu, and Gd Isotopes to Constrain the Nucleosynthesis Yields in the Rare-earth Region. *The Astrophysical Journal*, 936(2):107, 2022. doi:10.3847/1538-4357/ac80fc. → pages xi, 32, 97, 98, 99, 100, 119, 122

[94] R. Surman and J. Engel. Changes in r-process abundances at late times. *Phys. Rev. C*, 64:035801, 2001. doi:10.1103/PhysRevC.64.035801. → page 32

[95] P. Ring and P. Schuck. *The Nuclear Many-Body Problem*. Springer Berlin, Heidelberg, 1980. → pages 33, 39, 51

[96] P. Möller, J.R. Nix, and K.-L. Kratz. Nuclear properties for astrophysical and radioactive-ion-beam applications. *Atomic Data and Nuclear Data Tables*, 66(2):131–343, 1997. doi:https://doi.org/10.1006/adnd.1997.0746. → page 33

[97] P. Möller, B. Pfeiffer, and K.-L. Kratz. New calculations of gross β-decay properties for astrophysical applications: Speeding-up the classical r process. *Phys. Rev. C*, 67:055802, 2003. doi:10.1103/PhysRevC.67.055802.

[98] P. Möller, M.R. Mumpower, T. Kawano, and W.D. Myers. Nuclear properties for astrophysical and radioactive-ion-beam applications (II). *Atomic Data and Nuclear Data Tables*, 125:1–192, 2019. doi:https://doi.org/10.1016/j.adt.2018.03.003. → pages 33, 98, 99, 101, 103, 105, 122, 124

[99] E. M. Ney, J. Engel, T. Li, and N. Schunck. Global description of β^- decay with the axially deformed skyrme finite-amplitude method: Extension to odd-mass and odd-odd nuclei. *Phys. Rev. C*, 102:034326, 2020. doi:10.1103/PhysRevC.102.034326. → pages 33, 98

[100] T. Marketin, L. Huther, and G. Martínez-Pinedo. Large-scale evaluation of β-decay rates of *r*-process nuclei with the inclusion of first-forbidden transitions. *Phys. Rev. C*, 93:025805, 2016. doi:10.1103/PhysRevC.93.025805. → pages 33, 98, 99

[101] W. Hauser and H. Feshbach. The inelastic scattering of neutrons. *Phys. Rev.*, 87:366–373, 1952. doi:10.1103/PhysRev.87.366. → page 33

[102] A. J. Koning, S. Hilaire, and M. C. Duijvestijn. Talys-1.0. In *International Conference on Nuclear Data for Science and Technology*, pages 211–214. EDP Sciences, 2007. → page 34

[103] T. Rauscher and F.-K. Thielemann. Astrophysical reaction rates from statistical model calculations. *Atomic Data and Nuclear Data Tables*, 75 (1):1–351, 2000. doi:https://doi.org/10.1006/adnd.2000.0834. URL https://nucastro.org/nonsmoker.html. → page 34

[104] T. Kawano. Coh3: The coupled-channels and hauser-feshbach code. In J. Escher, Y. Alhassid, L. A. Bernstein, D. Brown, C. Fröhlich, P. Talou, and W. Younes, editors, *Compound-Nuclear Reactions*, pages 27–34, Cham, 2021. Springer International Publishing. → page 34

[105] S. Goriely, S. Hilaire, A. J. Koning, M. Sin, and R. Capote. Towards a prediction of fission cross sections on the basis of microscopic nuclear inputs. *Phys. Rev. C*, 79:024612, 2009. doi:10.1103/PhysRevC.79.024612. → page 34

[106] J. Erler, K. Langanke, H. P. Loens, G. Martínez-Pinedo, and P.-G. Reinhard. Fission properties for *r*-process nuclei. *Phys. Rev. C*, 85:025802, 2012. doi:10.1103/PhysRevC.85.025802.

[107] P. Möller, A. J. Sierk, T. Ichikawa, A. Iwamoto, and M. R. Mumpower. Fission barriers at the end of the chart of the nuclides. *Phys. Rev. C*, 91: 024310, 2015. doi:10.1103/PhysRevC.91.024310.

[108] S. A. Giuliani, G. Martínez-Pinedo, and L. M. Robledo. Fission properties of superheavy nuclei for *r*-process calculations. *Phys. Rev. C*, 97:034323, 2018. doi:10.1103/PhysRevC.97.034323. → page 34

[109] Panov, I. V., Korneev, I. Yu., Rauscher, T., Martínez-Pinedo, G., Keli´c-Heil, A., Zinner, N. T., and Thielemann, F.-K. Neutron-induced astrophysical reaction rates for translead nuclei*. *Astronomy and Astrophysics*, 513:A61, 2010. doi:10.1051/0004-6361/200911967. → page 34

[110] S. A. Giuliani, G. Martínez-Pinedo, M.-R. Wu, and L. M. Robledo. Fission and the *r*-process nucleosynthesis of translead nuclei in neutron star mergers. *Phys. Rev. C*, 102:045804, 2020. doi:10.1103/PhysRevC.102.045804.

[111] M. R. Mumpower, T. Kawano, and T. M. Sprouse. Beta-delayed fission in the coupled quasi-particle random phase approximation plus hauser-feshbach approach, 2022. URL https://arxiv.org/abs/2201.02889. → page 34

[112] C. L. Zhang, B. Schuetrumpf, and W. Nazarewicz. Nucleon localization and fragment formation in nuclear fission. *Phys. Rev. C*, 94:064323, 2016. doi:10.1103/PhysRevC.94.064323. → page 34

[113] C. Schmitt, K.-H. Schmidt, and B. Jurado. Benchmark of the gef code for fission-fragment yields over an enlarged range in fissioning nucleus mass, excitation energy, and angular momentum. *Phys. Rev. C*, 98:044605, 2018. doi:10.1103/PhysRevC.98.044605.

[114] M. R. Mumpower, P. Jaffke, M. Verriere, and J. Randrup. Primary fission fragment mass yields across the chart of nuclides. *Phys. Rev. C*, 101: 054607, 2020. doi:10.1103/PhysRevC.101.054607.

[115] J. Sadhukhan, S. A. Giuliani, Z. Matheson, and W. Nazarewicz. Efficient method for estimation of fission fragment yields of *r*-process nuclei. *Phys. Rev. C*, 101:065803, 2020. doi:10.1103/PhysRevC.101.065803.

[116] N. Vassh, M. R. Mumpower, G. C. McLaughlin, T. M. Sprouse, and R. Surman. Coproduction of light and heavy r-process elements via fission deposition. *The Astrophysical Journal*, 896(1):28, 2020. doi:10.3847/1538-4357/ab91a9. → page 34

[117] K.-L. Kratz, J.-P. Bitouzet, F.-K. Thielemann, P. Möller, and B. Pfeiffer. Isotopic r-Process Abundances and Nuclear Structure Far from Stability: Implications for the r-Process Mechanism. *The Astrophysical Journal*, 403: 216, January 1993. doi:10.1086/172196. → page 35

[118] C. Freiburghaus, J.-F. Rembges, T. Rauscher, E. Kolbe, F.-K. Thielemann, K.-L. Kratz, B. Pfeiffer, and J. J. Cowan. The astrophysical r-process: A comparison of calculations following adiabatic expansion with classical calculations based on neutron densities and temperatures. *The Astrophysical Journal*, 516(1):381, may 1999. doi:10.1086/307072. → page 35

[119] P. Möller, A. J. Sierk, T. Ichikawa, and H. Sagawa. Nuclear ground-state masses and deformations: Frdm(2012). *Atomic Data and Nuclear Data Tables*, 109-110:1–204, 2016. ISSN 0092-640X. doi:https://doi.org/10.1016/j.adt.2015.10.002. → pages xiii, 38, 43, 45, 56, 76, 83, 102, 107, 122, 124

[120] F. W. Aston. Isotopes and atomic weights. *Nature*, 105(2646):617–619, 1920. doi:10.1038/105617a0. → page 39

[121] D. Lunney, J. M. Pearson, and C. Thibault. Recent trends in the determination of nuclear masses. *Rev. Mod. Phys.*, 75:1021–1082, 2003. doi:10.1103/RevModPhys.75.1021. → pages 39, 42

[122] A. S. Eddington. The internal constitution of the stars. *Nature*, 106(2653): 14–20, 1920. doi:10.1038/106014a0. → page 39

[123] C. F. von Weizsäcker. Zur theorie der kernmassen. *Zeitschrift für Physik*, 96(7):431–458, 1935. → page 39

[124] H. A. Bethe and R. F. Bacher. Nuclear physics a. stationary states of nuclei. *Rev. Mod. Phys.*, 8:82–229, 1936. doi:10.1103/RevModPhys.8.82. → page 39

[125] K. S. Krane. *Introductory nuclear physics*. John Wiley & Sons, 1991. → page 40

[126] J. Mendoza-Temis. *Nuclear masses and their impact in r-process nucleosynthesis*. PhD thesis, Technische Universität, Darmstadt, 2014. URL http://tuprints.ulb.tu-darmstadt.de/4100/. → page 40

[127] G. Audi, M. Wang, A.H. Wapstra, F.G. Kondev, M. MacCormick, X. Xu, and B. Pfeiffer. The ame2012 atomic mass evaluation. *Chinese Physics C*, 36(12):1287, 2012. doi:10.1088/1674-1137/36/12/002. → pages 40, 51

[128] W. D. Myers and W. J. Swiatecki. Nuclear masses and deformations. *Nuclear Physics*, 81(1):1–60, 1966. ISSN 0029-5582. doi:https://doi.org/10.1016/0029-5582(66)90639-0. → page 42

[129] V. M. Strutinsky. Shell effects in nuclear masses and deformation energies. *Nuclear Physics A*, 95(2):420–442, 1967. ISSN 0375-9474. doi:https://doi.org/10.1016/0375-9474(67)90510-6. → pages 42, 43

[130] V. M. Strutinsky. "shells" in deformed nuclei. *Nuclear Physics A*, 122(1): 1–33, 1968. ISSN 0375-9474. doi:https://doi.org/10.1016/0375-9474(68)90699-4. → pages 42, 43

[131] W. D. Myers and W. J. Swiatecki. The macroscopic approach to nuclear masses and deformations. *Annual Review of Nuclear and Particle Science*, 32(1):309–334, 1982. doi:10.1146/annurev.ns.32.120182.001521. → page 42

[132] P. Möller, J. R. Nix, W. D. Myers, and W. J. Swiatecki. Nuclear ground-state masses and deformations. *Atomic Data and Nuclear Data Tables*, 59(2):185–381, 1995. ISSN 0092-640X. doi:https://doi.org/10.1006/adnd.1995.1002. → pages 43, 76

[133] J. Bardeen, L. N. Cooper, and J. R. Schrieffer. Theory of superconductivity. *Phys. Rev.*, 108:1175–1204, 1957. doi:10.1103/PhysRev.108.1175. → page 44

[134] W. D. Myers and W. J. Swiatecki. Average nuclear properties. *Annals of Physics*, 55(3):395–505, 1969. ISSN 0003-4916. doi:https://doi.org/10.1016/0003-4916(69)90202-4. → page 44

[135] W. D. Myers and W. J. Swiatecki. The nuclear droplet model for arbitrary shapes. *Annals of Physics*, 84(1):186–210, 1974. ISSN 0003-4916. doi:https://doi.org/10.1016/0003-4916(74)90299-1. → page 44

[136] I. Tanihata, D. Hirata, T. Kobayashi, S. Shimoura, K. Sugimoto, and H. Toki. Revelation of thick neutron skins in nuclei. *Physics Letters B*, 289 (3):261–266, 1992. ISSN 0370-2693. doi:https://doi.org/10.1016/0370-2693(92)91216-V. → page 44

[137] J. Treiner, W. D. Myers, W. J. Swiatecki, and M. S. Weiss. Bulk compression due to surface tension in hartree-fock, thomas-fermi and droplet-model calculations. *Nuclear Physics A*, 452(1):93–104, 1986. ISSN 0375-9474. doi:https://doi.org/10.1016/0375-9474(86)90510-5. → page 45

[138] H. J. Lipkin. Collective motion in many-particle systems: Part 1. the violation of conservation laws. *Annals of Physics*, 9(2):272–291, 1960. ISSN 0003-4916. doi:https://doi.org/10.1016/0003-4916(60)90032-4. → page 46

[139] Y. Nogami. Improved superconductivity approximation for the pairing interaction in nuclei. *Phys. Rev.*, 134:B313–B321, 1964. doi:10.1103/PhysRev.134.B313.

[140] H. C. Pradhan, Y. Nogami, and J. Law. Study of approximations in the nuclear pairing-force problem. *Nuclear Physics A*, 201(2):357–368, 1973. ISSN 0375-9474. doi:https://doi.org/10.1016/0375-9474(73)90071-7. → page 46

[141] M. Samyn, S. Goriely, P.-H. Heenen, J. M. Pearson, and F. Tondeur. A hartree–fock–bogoliubov mass formula. *Nuclear Physics A*, 700(1): 142–156, 2002. ISSN 0375-9474. doi:https://doi.org/10.1016/S0375-9474(01)01316-1. → pages 47, 49

[142] S. Goriely, M. Samyn, P.-H. Heenen, J. M. Pearson, and F. Tondeur. Hartree-Fock mass formulas and extrapolation to new mass data. *Phys. Rev. C*, 66:024326, 2002. doi:10.1103/PhysRevC.66.024326. → pages 47, 49

[143] S. Goriely, N. Chamel, and J. M. Pearson. Further explorations of Skyrme-Hartree-Fock-Bogoliubov mass formulas. XVI. Inclusion of self-energy effects in pairing. *Phys. Rev. C*, 93:034337, 2016. doi:10.1103/PhysRevC.93.034337. → pages 47, 56, 76, 83

[144] S. Goriely, F. Tondeur, and J. M. Pearson. A Hartree–Fock nuclear mass table. *Atomic Data and Nuclear Data Tables*, 77(2):311–381, 2001. ISSN 0092-640X. doi:https://doi.org/10.1006/adnd.2000.0857. → page 49

[145] N. Wang, M. Liu, and X. Wu. Modification of nuclear mass formula by considering isospin effects. *Phys. Rev. C*, 81:044322, 2010. doi:10.1103/PhysRevC.81.044322. → pages 51, 52, 76

[146] Y. Aboussir, J. M. Pearson, A. K. Dutta, and F. Tondeur. Nuclear mass formula via an approximation to the Hartree—Fock method. *Atomic Data and Nuclear Data Tables*, 61(1):127–176, 1995. ISSN 0092-640X. doi:https://doi.org/10.1016/S0092-640X(95)90014-4. → pages 51, 52, 58, 60

[147] H. J. Krappe and K. Pomorski. *Theory of Nuclear Fission: A Textbook*, volume 838. Springer Science & Business Media, 2012. → page 52

[148] S. Goriely. Nuclear inputs for astrophysics applications. *AIP Conference Proceedings*, 529(1):287–294, 2000. doi:10.1063/1.1361389. → pages 52, 56, 83

[149] N. Wang, Z. Liang, M. Liu, and X. Wu. Mirror nuclei constraint in nuclear mass formula. *Phys. Rev. C*, 82:044304, 2010. doi:10.1103/PhysRevC.82.044304. → pages 52, 76

[150] M. Liu, N. Wang, Y. Deng, and X. Wu. Further improvements on a global nuclear mass model. *Phys. Rev. C*, 84:014333, 2011. doi:10.1103/PhysRevC.84.014333. → page 76

[151] N. Wang and M. Liu. Nuclear mass predictions with a radial basis function approach. *Phys. Rev. C*, 84:051303, 2011. doi:10.1103/PhysRevC.84.051303. → page 54

[152] N. Wang, M. Liu, X. Wu, and J. Meng. Surface diffuseness correction in global mass formula. *Physics Letters B*, 734:215–219, 2014. ISSN 0370-2693. doi:https://doi.org/10.1016/j.physletb.2014.05.049. → pages 52, 56, 76, 83, 85

[153] J. Duflo and A. P. Zuker. Microscopic mass formulas. *Phys. Rev. C*, 52: R23–R27, 1995. doi:10.1103/PhysRevC.52.R23. → pages 54, 56, 76, 83

[154] Duflo-Zuker mass formula software package. https://www-nds.iaea.org/amdc/Duflo-Zuker-program.zip. Accessed: 2022-11-19. → pages 54, 58, 60

[155] H. Koura, M. Uno, T. Tachibana, and M. Yamada. Nuclear mass formula with shell energies calculated by a new method. *Nuclear Physics A*, 674(1): 47–76, 2000. ISSN 0375-9474. doi:https://doi.org/10.1016/S0375-9474(00)00155-X. → page 54

[156] H. Koura, T. Tachibana, M. Uno, and M. Yamada. Nuclidic Mass Formula on a Spherical Basis with an Improved Even-Odd Term. *Progress of Theoretical Physics*, 113(2):305–325, 2005. doi:10.1143/PTP.113.305. → pages 54, 56, 83

[157] A. Boehnlein, M. Diefenthaler, N. Sato, M. Schram, V. Ziegler, C. Fanelli, M. Hjorth-Jensen, T. Horn, M. P. Kuchera, D. Lee, W. Nazarewicz, P. Ostroumov, K. Orginos, A. Poon, X.-N. Wang, A. Scheinker, M. S. Smith, and L.-G. Pang. Colloquium: Machine learning in nuclear physics. *Rev. Mod. Phys.*, 94:031003, 2022. doi:10.1103/RevModPhys.94.031003. → page 61

[158] D. R. Phillips, R. J. Furnstahl, U. Heinz, T. Maiti, W. Nazarewicz, F. M. Nunes, M. Plumlee, M. T. Pratola, S. Pratt, F. G. Viens, and S. M. Wild. Get on the band wagon: a bayesian framework for quantifying model uncertainties in nuclear dynamics. *Journal of Physics G: Nuclear and Particle Physics*, 48(7):072001, 2021. doi:10.1088/1361-6471/abf1df. → page 61

[159] R. T. Cox. Probability, frequency and reasonable expectation. *American journal of physics*, 14(1):1–13, 1946. → page 62

[160] R. T. Cox. The algebra of probable inference. *American Journal of Physics*, 31(1):66–67, 1963.

[161] L. J. Savage. The foundations of statistics; jon wiley and sons. *Inc.: New York, NY, USA*, 1954.

[162] L. J. Savage, G. Barnard, J. Cornfield, I. Bross, I. J. Good, D. V. Lindley, C. W. Clunies-Ross, J. W. Pratt, H. Levene, T. Goldman, et al. On the foundations of statistical inference: Discussion. *Journal of the American Statistical Association*, 57(298):307–326, 1962.

[163] P. D. Hoff. *A first course in Bayesian statistical methods*, volume 580. Springer, 2009. → pages 63, 66

[164] C. M. Bishop and N. M. Nasrabadi. *Pattern recognition and machine learning*. Springer, 2006. → pages 62, 63, 72, 73

[165] K. P. Murphy. *Machine learning: a probabilistic perspective*. MIT press, 2012. → page 63

[166] A. Gelman, J. B. Carlin, H. S. Stern, and D. B. Rubin. *Bayesian data analysis*. Chapman and Hall/CRC, 1995. → pages 63, 64, 65, 66

[167] A. Gelman. Prior choice recommendations. https://github.com/stan-dev/stan/wiki/Prior-Choice-Recommendations, 2020. → page 63

[168] A. Gelman, D. Simpson, and M. Betancourt. The prior can often only be understood in the context of the likelihood. *Entropy*, 19(10):555, 2017. doi:10.3390/e19100555. → page 80

[169] A. Gelman, A. Jakulin, M. G. Pittau, and Y.-S. Su. A weakly informative default prior distribution for logistic and other regression models. *The Annals of Applied Statistics*, 2(4):1360 – 1383, 2008. doi:10.1214/08-AOAS191. → page 63

[170] H. Tak, S. K Ghosh, and J. A. Ellis. How proper are Bayesian models in the astronomical literature? *Monthly Notices of the Royal Astronomical Society*, 481(1):277–285, 2018. doi:10.1093/mnras/sty2326. → page 63

[171] R. M. Neal. *Bayesian learning for neural networks*, volume 118. Springer Science & Business Media, 2012. → pages 67, 74, 82

[172] M. Betancourt. A conceptual introduction to hamiltonian monte carlo, 2017. URL https://arxiv.org/abs/1701.02434.

[173] C. C. Monnahan, J. T. Thorson, and T. A. Branch. Faster estimation of bayesian models in ecology using hamiltonian monte carlo. *Methods in Ecology and Evolution*, 8(3):339–348, 2017. doi:https://doi.org/10.1111/2041-210X.12681. → page 67

[174] M. D. Hoffman and A. Gelman. The no-u-turn sampler: Adaptively setting path lengths in hamiltonian monte carlo, 2011. URL https://arxiv.org/abs/1111.4246. → page 67

[175] J. Salvatier, T. V. Wiecki, and C. Fonnesbeck. Probabilistic programming in python using PyMC3. *PeerJ Computer Science*, 2:e55, 2016. doi:10.7717/peerj-cs.55. → pages 67, 82

[176] A. Saltelli and P. Annoni. How to avoid a perfunctory sensitivity analysis. *Environmental Modelling & Software*, 25(12):1508–1517, 2010. ISSN 1364-8152. doi:https://doi.org/10.1016/j.envsoft.2010.04.012. → page 67

[177] J. Bliss, A. Arcones, F. Montes, and J. Pereira. Nuclear physics uncertainties in neutrino-driven, neutron-rich supernova ejecta. *Phys. Rev. C*, 101:055807, 2020. doi:10.1103/PhysRevC.101.055807. → pages 67, 68, 119, 133

[178] T. Rauscher, N. Nishimura, R. Hirschi, G. Cescutti, A. St. J. Murphy, and A. Heger. Uncertainties in the production of p nuclei in massive stars obtained from Monte Carlo variations. *Monthly Notices of the Royal Astronomical Society*, 463(4):4153–4166, 2016. ISSN 0035-8711. doi:10.1093/mnras/stw2266. → page 68

[179] N. Nishimura, R. Hirschi, T. Rauscher, A. St. J. Murphy, and G. Cescutti. Uncertainties in s-process nucleosynthesis in massive stars determined by Monte Carlo variations. *Monthly Notices of the Royal Astronomical Society*, 469(2):1752–1767, 2017. ISSN 0035-8711. doi:10.1093/mnras/stx696. → pages 68, 119, 133

[180] A. Saltelli, P. Annoni, I. Azzini, F. Campolongo, M. Ratto, and S. Tarantola. Variance based sensitivity analysis of model output. design and estimator for the total sensitivity index. *Computer Physics Communications*, 181(2):259–270, 2010. ISSN 0010-4655. doi:https://doi.org/10.1016/j.cpc.2009.09.018. → pages 68, 69, 71, 98, 123

[181] A. Ekström and G. Hagen. Global sensitivity analysis of bulk properties of an atomic nucleus. *Phys. Rev. Lett.*, 123:252501, 2019. doi:10.1103/PhysRevLett.123.252501. → page 68

[182] T. A. Mara, S. Tarantola, and P. Annoni. Non-parametric methods for global sensitivity analysis of model output with dependent inputs. *Environmental Modelling & Software*, 72:173–183, 2015. ISSN 1364-8152. doi:https://doi.org/10.1016/j.envsoft.2015.07.010. → pages 68, 70, 71

[183] I. M. Sobol'. Sensitivity estimates for nonlinear mathematical models. *Mathematical Modelling and Computational Experiments*, 1(4):407–414, 1993. → pages 68, 69

[184] J. Herman and W. Usher. SALib: An open-source python library for sensitivity analysis. *The Journal of Open Source Software*, 2(9), 2017. doi:10.21105/joss.00097. → page 71

[185] G. E. B. Archer, A. Saltelli, and I. M. Sobol. Sensitivity measures,anova-like techniques and the use of bootstrap. *Journal of*

Statistical Computation and Simulation, 58(2):99–120, 1997. doi:10.1080/00949659708811825. → page 71

[186] I. Goodfellow, Y. Bengio, and A. Courville. *Deep Learning*. MIT Press, 2016. http://www.deeplearningbook.org. → pages 72, 73, 120

[187] F. Chollet et al. Keras. https://keras.io, 2015. → pages 72, 124

[188] M. Abadi, A. Agarwal, P. Barham, E. Brevdo, Z. Chen, C. Citro, G. S. Corrado, A. Davis, J. Dean, M. Devin, S. Ghemawat, I. Goodfellow, A. Harp, G. Irving, M. Isard, Y. Jia, R. Jozefowicz, L. Kaiser, M. Kudlur, J. Levenberg, D. Mané, R. Monga, S. Moore, D. Murray, C. Olah, M. Schuster, J. Shlens, B. Steiner, I. Sutskever, K. Talwar, P. Tucker, V. Vanhoucke, V. Vasudevan, F. Viégas, O. Vinyals, P. Warden, M. Wattenberg, M. Wicke, Y. Yu, and X. Zheng. TensorFlow: Large-scale machine learning on heterogeneous systems, 2015. URL https://www.tensorflow.org/. Software available from tensorflow.org. → pages 72, 124

[189] A. F. Agarap. Deep learning using rectified linear units (relu), 2018. URL https://arxiv.org/abs/1803.08375. → pages 73, 125

[190] C. E. Rasmussen and C. K. I. Williams. *Gaussian Processes for Machine Learning*. The MIT Press, 2005. doi:10.7551/mitpress/3206.001.0001. → pages 74, 82, 120

[191] M. C. Kennedy, C. W. Anderson, S. Conti, and A. O'Hagan. Case studies in gaussian process modelling of computer codes. *Reliability Engineering & System Safety*, 91(10):1301–1309, 2006. doi:https://doi.org/10.1016/j.ress.2005.11.028. The Fourth International Conference on Sensitivity Analysis of Model Output (SAMO 2004). → pages 74, 120

[192] L. S. Bastos and A. O'Hagan. Diagnostics for gaussian process emulators. *Technometrics*, 51(4):425–438, 2009. doi:10.1198/TECH.2009.08019. → pages 74, 120

[193] B. Lakshminarayanan, A. Pritzel, and C. Blundell. Simple and scalable predictive uncertainty estimation using deep ensembles. In I. Guyon, U. Von Luxburg, S. Bengio, H. Wallach, R. Fergus, S. Vishwanathan, and R. Garnett, editors, *Advances in Neural Information Processing Systems*, volume 30. Curran Associates, Inc., 2017. URL

https://proceedings.neurips.cc/paper/2017/file/9ef2ed4b7fd2c810847ffa5fa85bce38-Paper.pdf. → pages 74, 120, 129

[194] J. Erler, N. Birge, M. Kortelainen, W. Nazarewicz, E. Olsen, A. M. Perhac, and M. Stoitsov. The limits of the nuclear landscape. *Nature*, 486(7404): 509–512, 2012. → page 76

[195] S. Goriely, S. Hilaire, M. Girod, and S. Péru. First gogny-hartree-fock-bogoliubov nuclear mass model. *Phys. Rev. Lett.*, 102: 242501, 2009. doi:10.1103/PhysRevLett.102.242501. → page 76

[196] D. Martin, A. Arcones, W. Nazarewicz, and E. Olsen. Impact of nuclear mass uncertainties on the *r* process. *Phys. Rev. Lett.*, 116:121101, 2016. doi:10.1103/PhysRevLett.116.121101. → pages 76, 99, 119

[197] Y. L. Zhu, K. A. Lund, J. Barnes, T. M. Sprouse, N. Vassh, G. C. McLaughlin, M. R. Mumpower, and R. Surman. Modeling kilonova light curves: Dependence on nuclear inputs. *The Astrophysical Journal*, 906(2): 94, 2021. doi:10.3847/1538-4357/abc69e. → page 76

[198] B. W. Sargent. The maximum energy of the β-rays from uranium x and other bodies. *Proceedings of the Royal Society of London. Series A, Containing Papers of a Mathematical and Physical Character*, 139(839): 659–673, 1933. → page 76

[199] Y. Zhou, Z.-H. Li, Y.-B. Wang, Y.-S. Chen, B. Guo, J. Su, Y.-J. Li, S.-Q. Yan, X.-Y. Li, Z.-Y. Han, Y.-P. Shen, L. Gan, S. Zeng, G. Lian, and W.-P. Liu. Empirical formula for β^--decay half-lives of r-process nuclei. *Science China Physics, Mechanics & Astronomy*, 60(8):082012, 2017. doi:10.1007/s11433-017-9045-0. → page 76

[200] J. Dobaczewski, W. Nazarewicz, and P.-G. Reinhard. Error estimates of theoretical models: a guide. *Journal of Physics G: Nuclear and Particle Physics*, 41(7):074001, 2014. doi:10.1088/0954-3899/41/7/074001. → page 77

[201] J. D. McDonnell, N. Schunck, D. Higdon, J. Sarich, S. M. Wild, and W. Nazarewicz. Uncertainty quantification for nuclear density functional theory and information content of new measurements. *Phys. Rev. Lett.*, 114:122501, 2015. doi:10.1103/PhysRevLett.114.122501. → page 77

[202] J. Van Schelt, D. Lascar, G. Savard, J. A. Clark, S. Caldwell, A. Chaudhuri, J. Fallis, J. P. Greene, A. F. Levand, G. Li, K. S. Sharma, M. G. Sternberg,

T. Sun, and B. J. Zabransky. Mass measurements near the *r*-process path using the canadian penning trap mass spectrometer. *Phys. Rev. C*, 85: 045805, 2012. doi:10.1103/PhysRevC.85.045805. → page 77

[203] M. Vilen, J. M. Kelly, A. Kankainen, M. Brodeur, A. Aprahamian, L. Canete, R. P. de Groote, A. de Roubin, T. Eronen, A. Jokinen, I. D. Moore, M. R. Mumpower, D. A. Nesterenko, J. O'Brien, A. Pardo Perdomo, H. Penttilä, M. Reponen, S. Rinta-Antila, and R. Surman. Exploring the mass surface near the rare-earth abundance peak via precision mass measurements at jyfltrap. *Phys. Rev. C*, 101:034312, 2020. doi:10.1103/PhysRevC.101.034312.

[204] C. Izzo, J. Bergmann, K. A. Dietrich, E. Dunling, D. Fusco, A. Jacobs, B. Kootte, G. Kripkó-Koncz, Y. Lan, E. Leistenschneider, E. M. Lykiardopoulou, I. Mukul, S. F. Paul, M. P. Reiter, J. L. Tracy, C. Andreoiu, T. Brunner, T. Dickel, J. Dilling, I. Dillmann, G. Gwinner, D. Lascar, K. G. Leach, W. R. Plaß, C. Scheidenberger, M. E. Wieser, and A. A. Kwiatkowski. Mass measurements of neutron-rich indium isotopes for *r*-process studies. *Phys. Rev. C*, 103:025811, 2021. doi:10.1103/PhysRevC.103.025811.

[205] H. F. Li, S. Naimi, T. M. Sprouse, M. R. Mumpower, Y. Abe, Y. Yamaguchi, D. Nagae, F. Suzaki, M. Wakasugi, H. Arakawa, W. B. Dou, D. Hamakawa, S. Hosoi, Y. Inada, D. Kajiki, T. Kobayashi, M. Sakaue, Y. Yokoda, T. Yamaguchi, R. Kagesawa, D. Kamioka, T. Moriguchi, M. Mukai, A. Ozawa, S. Ota, N. Kitamura, S. Masuoka, S. Michimasa, H. Baba, N. Fukuda, Y. Shimizu, H. Suzuki, H. Takeda, D. S. Ahn, M. Wang, C. Y. Fu, Q. Wang, S. Suzuki, Z. Ge, Yu. A. Litvinov, G. Lorusso, P. M. Walker, Zs. Podolyak, and T. Uesaka. First application of mass measurements with the rare-ri ring reveals the solar *r*-process abundance trend at $a = 122$ and $a = 123$. *Phys. Rev. Lett.*, 128:152701, 2022. doi:10.1103/PhysRevLett.128.152701. → page 77

[206] A. E. Raftery, T. Gneiting, F. Balabdaoui, and M. Polakowski. Using bayesian model averaging to calibrate forecast ensembles. *Monthly Weather Review*, 133(5):1155 – 1174, 2005. doi:10.1175/MWR2906.1. → pages 77, 78, 79, 80, 81, 91

[207] Z. M. Niu and H. Z. Liang. Nuclear mass predictions with machine learning reaching the accuracy required by *r*-process studies. *Phys. Rev. C*, 106:L021303, 2022. doi:10.1103/PhysRevC.106.L021303. → page 78

[208] Z.M. Niu and H.Z. Liang. Nuclear mass predictions based on bayesian neural network approach with pairing and shell effects. *Physics Letters B*, 778:48–53, 2018. ISSN 0370-2693. doi:https://doi.org/10.1016/j.physletb.2018.01.002.

[209] L. Neufcourt, Y. Cao, W. Nazarewicz, and F. Viens. Bayesian approach to model-based extrapolation of nuclear observables. *Phys. Rev. C*, 98: 034318, 2018. doi:10.1103/PhysRevC.98.034318. → pages 82, 96

[210] L. Neufcourt, Y. Cao, W. Nazarewicz, E. Olsen, and F. Viens. Neutron drip line in the ca region from bayesian model averaging. *Phys. Rev. Lett.*, 122: 062502, 2019. doi:10.1103/PhysRevLett.122.062502. → pages 82, 94, 96, 133

[211] R.-D. Lasseri, D. Regnier, J.-P. Ebran, and A. Penon. Taming nuclear complexity with a committee of multilayer neural networks. *Phys. Rev. Lett.*, 124:162502, 2020. doi:10.1103/PhysRevLett.124.162502.

[212] R. Utama, J. Piekarewicz, and H. B. Prosper. Nuclear mass predictions for the crustal composition of neutron stars: A bayesian neural network approach. *Phys. Rev. C*, 93:014311, 2016. doi:10.1103/PhysRevC.93.014311.

[213] A. E. Lovell, A. T. Mohan, T. M. Sprouse, and M. R. Mumpower. Nuclear masses learned from a probabilistic neural network. *Phys. Rev. C*, 106: 014305, 2022. doi:10.1103/PhysRevC.106.014305.

[214] M. R. Mumpower, T. M. Sprouse, A. E. Lovell, and A. T. Mohan. Physically interpretable machine learning for nuclear masses. *Phys. Rev. C*, 106:L021301, 2022. doi:10.1103/PhysRevC.106.L021301. → page 78

[215] J. A. Hoeting, D. Madigan, A. E. Raftery, and C. T. Volinsky. Bayesian model averaging: a tutorial (with comments by M. Clyde, David Draper and E. I. George, and a rejoinder by the authors. *Statistical Science*, 14(4): 382 – 417, 1999. doi:10.1214/ss/1009212519. → page 78

[216] A. Hamaker, E. Leistenschneider, R. Jain, G. Bollen, S. A. Giuliani, K. Lund, W. Nazarewicz, L. Neufcourt, C. R. Nicoloff, D. Puentes, R. Ringle, C. S. Sumithrarachchi, and I. T. Yandow. Precision mass measurement of lightweight self-conjugate nucleus 80zr. *Nature Physics*, 17(12):1408–1412, 2021. doi:10.1038/s41567-021-01395-w. → pages 82, 96

[217] L. Neufcourt, Y. Cao, S. A. Giuliani, W. Nazarewicz, E. Olsen, and O. B. Tarasov. Quantified limits of the nuclear landscape. *Phys. Rev. C*, 101: 044307, 2020. doi:10.1103/PhysRevC.101.044307. → pages 94, 133

[218] L. Neufcourt, Y. Cao, S. Giuliani, W. Nazarewicz, E. Olsen, and O. B. Tarasov. Beyond the proton drip line: Bayesian analysis of proton-emitting nuclei. *Phys. Rev. C*, 101:014319, 2020. doi:10.1103/PhysRevC.101.014319. → pages 82, 96

[219] S. Yoshida. Nonparametric bayesian approach to extrapolation problems in configuration interaction methods. *Phys. Rev. C*, 102:024305, 2020. doi:10.1103/PhysRevC.102.024305. → page 82

[220] R. M. Neal et al. Mcmc using hamiltonian dynamics. *Handbook of markov chain monte carlo*, 2(11):2, 2011. → page 82

[221] M. Stephens. Dealing with label switching in mixture models. *Journal of the Royal Statistical Society: Series B (Statistical Methodology)*, 62(4): 795–809, 2000. doi:https://doi.org/10.1111/1467-9868.00265. → page 82

[222] A. Jasra, C. C. Holmes, and D. A. Stephens. Markov Chain Monte Carlo Methods and the Label Switching Problem in Bayesian Mixture Modeling. *Statistical Science*, 20(1):50 – 67, 2005. doi:10.1214/088342305000000016. → page 82

[223] G. Audi, A.H. Wapstra, and C. Thibault. The ame2003 atomic mass evaluation: (ii). tables, graphs and references. *Nuclear Physics A*, 729(1): 337–676, 2003. ISSN 0375-9474. doi:https://doi.org/10.1016/j.nuclphysa.2003.11.003. The 2003 NUBASE and Atomic Mass Evaluations. → pages 83, 93

[224] S. R. Stroberg, J. D. Holt, A. Schwenk, and J. Simonis. Ab initio limits of atomic nuclei. *Phys. Rev. Lett.*, 126:022501, 2021. doi:10.1103/PhysRevLett.126.022501. → pages 94, 133

[225] A. Tolosa-Delgado, J. Agramunt, J. Tain, A. Algora, C. Domingo-Pardo, and A. Morales. Commissioning of the BRIKEN detector for the measurement of very exotic β-delayed neutron emitters. *Nucl. Instrum. Methods Phys. Res., Sect. A, Accel. Spectrom. Detect. Assoc. Equip.*, 925: 133–147, 2019. → page 97

[226] N. Fukuda, T. Kubo, T. Ohnishi, N. Inabe, H. Takeda, D. Kameda, and H. Suzuki. Identification and separation of radioactive isotope beams by

the bigrips separator at the riken ri beam factory. *Nucl. Instr. Meth.*, 317: 323, 2013. doi:10.1016/j.nimb.2013.08.048. → page 97

[227] J. Wu, S. Nishimura, G. Lorusso, P. Möller, E. Ideguchi, and P. H. Regan. 94 β-Decay Half-Lives of Neutron-Rich $_{55}$Cs to $_{67}$Ho: Experimental Feedback and Evaluation of the r-Process Rare-Earth Peak Formation . *Physical Review Letters*, 118:072701, 2017. → pages xiv, 98, 101, 103, 105

[228] R. Minato, T. Marketin, and N. Paar. β-delayed neutron-emission and fission calculations within relativistic quasiparticle random-phase approximation and a statistical model. *Phys. Rev. C*, 104:044321, 2021. doi:10.1103/PhysRevC.104.044321. → page 99

[229] T. M. Sprouse, R. Navarro Perez, R. Surman, M. R. Mumpower, G. C. McLaughlin, and N. Schunck. Propagation of statistical uncertainties of skyrme mass models to simulations of *r*-process nucleosynthesis. *Phys. Rev. C*, 101:055803, 2020. doi:10.1103/PhysRevC.101.055803. → pages 99, 119, 122

[230] N. Vassh, R. Vogt, R. Surman, J. Randrup, T. M. Sprouse, M. R. Mumpower, P. Jaffke, D. Shaw, E. M. Holmbeck, Y. Zhu, and G. C. McLaughlin. Using excitation-energy dependent fission yields to identify key fissioning nuclei in r-process nucleosynthesis. *Journal of Physics G: Nuclear and Particle Physics*, 46(6):065202, 2019. doi:10.1088/1361-6471/ab0bea. → page 102

[231] S. Rosswog, T. Piran, and E. Nakar. The multimessenger picture of compact object encounters: binary mergers versus dynamical collisions. *Monthly Notices of the Royal Astronomical Society*, 430(4):2585–2604, 2013. doi:10.1093/mnras/sts708. → page 102

[232] T. Piran, E. Nakar, and S. Rosswog. The electromagnetic signals of compact binary mergers. *Monthly Notices of the Royal Astronomical Society*, 430(3):2121–2136, 2013. ISSN 0035-8711. doi:10.1093/mnras/stt037. → page 102

[233] B. S. Meyer. *r*-process nucleosynthesis without excess neutrons. *Phys. Rev. Lett.*, 89:231101, 2002. doi:10.1103/PhysRevLett.89.231101. → page 102

[234] T. M. Sprouse, M. R. Mumpower, and R. Surman. Following nuclei through nucleosynthesis: A novel tracing technique. *Phys. Rev. C*, 104: 015803, 2021. doi:10.1103/PhysRevC.104.015803. → page 103

[235] M. Wang, G. Audi, F. G. Kondev, W. J. Huang, S. Naimi, and X. Xu. The AME2016 atomic mass evaluation (II). tables, graphs and references. *Chinese Physics C*, 41(3):030003, 2017. doi:10.1088/1674-1137/41/3/030003. → page 103

[236] G. Audi, F. G. Kondev, M. Wang, W. J. Huang, and S. Naimi. The NUBASE2016 evaluation of nuclear properties. *Chinese Physics C*, 41(3): 030001, 2017. doi:10.1088/1674-1137/41/3/030001. → page 103

[237] P. Dimitriou, I. Dillmann, B. Singh, V. Piksaikin, K.P. Rykaczewski, J.L. Tain, A. Algora, K. Banerjee, I.N. Borzov, D. Cano-Ott, S. Chiba, M. Fallot, D. Foligno, R. Grzywacz, X. Huang, T. Marketin, F. Minato, G. Mukherjee, B.C. Rasco, A. Sonzogni, M. Verpelli, A. Egorov, M. Estienne, L. Giot, D. Gremyachkin, M. Madurga, E.A. McCutchan, E. Mendoza, K.V. Mitrofanov, M. Narbonne, P. Romojaro, A. Sanchez-Caballero, and N.D. Scielzo. Development of a reference database for beta-delayed neutron emission. *Nuclear Data Sheets*, 173: 144–238, 2021. doi:https://doi.org/10.1016/j.nds.2021.04.006. Special Issue on Nuclear Reaction Data. → pages 108, 109, 112

[238] M. R. Mumpower, G. C. McLaughlin, R. Surman, and A. W. Steiner. Reverse engineering nuclear properties from rare earth abundances in the r process. *Journal of Physics G: Nuclear and Particle Physics*, 44(3): 034003, 2017. doi:10.1088/1361-6471/44/3/034003. → pages 120, 134

[239] N. Vassh, G. C. McLaughlin, M. R. Mumpower, and R. Surman. Markov chain monte carlo predictions of neutron-rich lanthanide properties as a probe of r-process dynamics. *The Astrophysical Journal*, 907(2):98, 2021. doi:10.3847/1538-4357/abd035. → pages 120, 134

[240] F. G. Kondev, M. Wang, W. J. Huang, S. Naimi, and G. Audi. The NUBASE2020 evaluation of nuclear physics properties. *Chinese Physics C*, 45(3):030001, 2021. doi:10.1088/1674-1137/abddae. → page 122

[241] J. Sola and J. Sevilla. Importance of input data normalization for the application of neural networks to complex industrial problems. *IEEE Transactions on Nuclear Science*, 44(3):1464–1468, 1997. doi:10.1109/23.589532. → page 123

[242] S. J. Reddi, S. Kale, and S. Kumar. On the convergence of adam and beyond, 2019. URL https://arxiv.org/abs/1904.09237. → page 124

[243] D. P. Kingma and J. Ba. Adam: A method for stochastic optimization, 2014. URL https://arxiv.org/abs/1412.6980. → page 124

[244] H. Jin, Q. Song, and X. Hu. Auto-keras: An efficient neural architecture search system. In *Proceedings of the 25th ACM SIGKDD International Conference on Knowledge Discovery & Data Mining*, pages 1946–1956. ACM, 2019. → page 125